

**Swirl and Blade Wakes in the Interaction between Gas  
Turbines and Exhaust Diffusers investigated by  
Endoscopic Particle Image Velocimetry**

Von der Fakultät für Maschinenbau  
der Gottfried Wilhelm Leibniz Universität Hannover  
zur Erlangung des akademischen Grades  
Doktor-Ingenieur  
genehmigte Dissertation  
von

Victor Opilat  
geboren am 07. August 1985 in St. Petersburg (Leningrad)

2011

Keywords:

Turbine Exhaust Diffuser, Blade Wake, Endoscopic Particle Image Velocimetry

Schlagworte für die Dokumentation:

Austrittsdiffusor Turbine, Nachlaufdüsen, Endoskopische Particle Image Velocimetry

Referent:	Prof. Dr.-Ing. Jörg Seume
Korreferent:	Prof. Dr.-Ing. Stephan Kabelac
Leiter der Prüfungskommission:	Prof. Dr.-Ing. Lothar Schulze
Zusätzlicher Mitglied	Prof. Dr. Viktor Chernikov
Tag der Promotion:	21. Oktober 2011

Gedruckt mit Unterstützung des Deutschen Akademischen Austauschdienstes

## **Acknowledgments**

This thesis was prepared as a result of my work as a research assistant at the Institute of Turbomachinery and Fluid Dynamics – TFD. Many thanks to my mentor Prof. Dr.-Ing. J. Seume. Many thanks to Dr.-Ing. J. Runkel, Dr.-Ing. O. Sieker, Dipl.-Ing. M. Kuschel, Dr. V. Sadovnichiy. This work was performed under supervision of Siemens AG corporate technology, Dr. T. Hammer, whose help is gratefully acknowledged. I gratefully acknowledge the financial support of the Siemens/DAAD stipend program and the help of the staff of DAAD.

Special thanks to Prof. V. Chernikov (Technical University of St. Petersburg). Special thanks to my girlfriend E. Shvets for helping to get power for work. Great thanks to my parents L. Opilat and W. Opilat for their help.

Hannover, 29<sup>th</sup> August 2011

Victor Opilat

## Abstract

Exhaust diffusers studied in this thesis are installed behind the last turbine stage of gas turbines, including those used in combined cycle power plants. Extensive research made in recent years proved that effects caused by an upstream turbine need to be taken into account when designing efficient diffusers. Under certain conditions these effects can stabilize the boundary layer in diffusers and prevent separation.

In this research the impact of multiple parameters, such as tip leakage flow, swirl, and rotating blade wakes, on the performance of a diffuser is studied. Experiments were conducted using a diffuser test rig with a rotating bladed wheel as a turbine effect generator and with an additional tip leakage flow insert. The major advantages of this test rig are modularity and easy variation of the main parameters. To capture the complexity and understand the physics of diffuser flow, and to clarify the phenomenon of the flow stabilisation, the 2D endoscopic laser optical measurement technique Particle Image Velocimetry (PIV) was adopted to the closed “rotating” diffuser test rig.

Intensity and distribution of vortices in the blade tip area are decisive for diffuser performance. Large vortices in the annular diffuser inlet behind the blade tips interact with the boundary layer in diffusers. At design point these vortices are very early suppressed by the main flow. For the operating point with a low value of the flow coefficient (negative swirl), vortices are about two times stronger than for design point and the boundary layer is destabilized. Vortices develop in the direction contrary to swirl in the main flow and just cause flow destabilization. Coherent back flow zones are induced and reduction of diffuser performance occurs. For the operating point with positive swirl (for a high flow coefficient value), these vortices are also strong but do not counteract the main flow because they develop in the same direction with the swirl in the main flow. Pressure recovery in the annular diffuser is even higher than for design point because vortices energize the boundary layer and the turbulence level in the core flow is very high. Turbulent energy is better transported to the peripheral zones of the channel by the swirled flow.

A small positive swirl angle in the inlet flow (behind the rotating bladed wheel in experiments) has a stabilizing effect on the diffuser, while negative swirl decreases its performance. This occurs due to change in the development of vertical structures downstream of the rotor blade tip area. The tip leakage flow from the last turbine stage positively affects pressure recovery in the diffuser energizing the boundary layer. Comparison of results for different diffuser test rig configurations with results from a more gas turbine-like test rig with a similar diffuser and a scaled turbine stage model and for higher Mach numbers showed similar pressure recovery trends, verifying the results.

## Zusammenfassung (German)

Die in dieser Dissertation behandelten Austrittsdiffusoren werden in der stationären Gasturbinen, auch in den kombinierten Gas- und Dampfkraftwerken, hinter der letzten Turbinenstufe eingesetzt. Die Forschung aus den letzten Jahren bestätigte es, dass der Interaktion zwischen der Gasturbine und dem Diffusor bei der Auslegung eines Diffusors Rechnung getragen werden sollte. Die durch die Turbine eingeführten Effekte können die Grenzschicht im Diffusor stabilisieren und Ablösung unterdrücken.

In dieser Arbeit wurde der Einfluss von der Spaltströmung, Drall und Nachlaufdübeln auf die Performance vom Diffusor untersucht. Ein Diffusorprüfstand wurde verwendet, der mit einem profilierten Speichenrad und einem zusätzlichen Spaltströmungszufuhr ausgerüstet ist. Die großen Vorteile dieses Prüfstandes sind der modulare Aufbau und die einfache Einstellung der Parameter. Um die Komplexität der Diffusorströmung zu verstehen, 2D endoskopische laser-optische Messtechnik Particle Image Velocimetry (PIV) wurde am rotierenden Diffusorprüfstand eingesetzt.

Die Intensität und Position der Wirbel in dem Bereich hinter der Schaufelspitze ist für die Diffusorperformance entscheidend. Große Wirbel in dem Diffusoreintritt interagieren mit der Grenzschicht an der Wand. Beim Auslegungspunkt sind diese Wirbel sehr schnell durch die Kernströmung unterdrückt. Für den Betriebspunkt mit niedrigerer Durchflusszahl sind die Wirbeln zweifach größer als bei dem Auslegungspunkt. Sie dehnen sich gegen der Richtung des Dralles in der Hauptströmung aus und destabilisieren die Grenzschicht. Kohärente Ablösegebiete entstehen, wodurch die Performance sinkt. Für den Betriebspunkt mit größerer Durchflusszahl sind die Wirbeln zwar auch groß, stören aber die Hauptströmung nicht, da sie sich in die Richtung des Dralles bewegen. Sogar größerer Druckaufbau im Diffusor wird erzielt, weil die Wirbel die Grenzschicht mit turbulenter Energie der versorgen.

Moderate positive Drallwinkel in der Eintrittsströmung haben eine stabilisierende Wirkung auf die Strömung, wobei negativer Drall die Performance verschlechtert. Das hat auf die unterschiedliche Wirbelverteilung im Bereich hinter den Schaufelspitzen zurückzuführen. Die Spaltströmung wirkt sich positiv auf die Performance aus, weil es Energie der Grenzschicht zuführt. Die Ergebnisse für verschiedene Prüfstandskonfigurationen sind mit den Ergebnissen der Forschung an einem realitätsnäheren Prüfstand mit einem ähnlichen Diffusor aber mit einem skalierten Turbinenmodell und für höhere Mach-Zahlen verglichen. Gleiche Abhängigkeit Druckaufbau-Drallwinkel konnten festgestellt werden.

# Contents

Acknowledgments .....	III
Abstract.....	IV
Zusammenfassung (German).....	V
Contents .....	VI
Abbreviations .....	VII
List of Figures.....	VII
List of Tables .....	IX
List of Symbols.....	X
Subscripts .....	X
1. Introduction .....	1
2. Interaction between Turbine and Exhaust Diffuser .....	4
2.1. Purpose of a diffuser behind a turbine.....	4
2.2. Geometric parameters of diffusers .....	5
2.3. Performance evaluation of diffusers .....	8
2.4. Design of exhaust diffusers considering the upstream turbine.....	9
3. Experimental facilities .....	14
3.1. Diffuser test rig at the Leibniz Universität Hannover .....	14
3.2. The test rig at St. Petersburg State Technical University .....	17
3.3. Geometric parameters of the diffuser test rigs.....	19
4. PIV Instrumentation .....	21
4.1. Endoscopic Particle Image Velocimetry (PIV); working principle.....	21
4.2. PIV in Turbomachinery .....	21
4.3. PIV measuring system and requirements .....	23
4.4. Endoscopic PIV .....	25
5. Measuring programme.....	27
5.1. Measuring programme.....	27
5.2. PIV Technique Validation .....	30
6. Diffuser Flow Features (acquired by PIV) and their impact on diffuser performance.....	31
6.1. Diffuser Boundary Layer Investigation.....	32
6.2. Diffuser Boundary Layer Investigation (2 <sup>nd</sup> Configuration) .....	41
6.3. Blade wake investigation.....	44
7. Parameters dominating the pressure recovery in the diffuser.....	48
7.1. Results with the bladed wheel and with the tip leakage flow.....	49
7.1.1. Flow parameter distributions .....	49
7.1.2. Coefficients.....	55
7.2. Results without a bladed wheel and with tip leakage flow.....	56
7.2.1. Flow parameter distributions .....	56
7.2.2. Coefficients.....	57
7.3. Results with turbine stage model (Chernikov) .....	58
7.4. Comparison of results .....	59
8. Conclusions .....	61
9. Literature .....	63
Appendix .....	67

## Abbreviations

2D	two-dimensional
3D	three-dimensional
CFD	computational fluid dynamics
GE	General Electrics
HRSG	heat recovery steam generator
ILA	Intelligent Laser Systems
LDA	Laser Doppler Anemometer
Nd:YAG	neodymium-doped yttrium aluminium garnet
PIV	Particle Image Velocimetry
RMS	root mean square
SPSTU	St. Petersburg State Technical University
TFD	Institut of Turbomachinery and Fluid-Dynamics

## List of Figures

Figure 1.1: Secondary flows; a: blade passage, b: tip leakage (Selesnev et al., 1986).....	2
Figure 2.1: Typical combined power plant layout (Siemens, www.siemens.com).....	4
Figure 2.3: F-Class axial diffuser (GE) .....	5
Figure 2.4: E-Class radial diffuser (GE).....	5
Figure 2.5: Basic diffuser geometries (Fleige, 2002) .....	6
Figure 2.6: Combined cycle power plant with SGT5-8000H gas turbine (Siemens©).....	6
Figure 2.7: Toshiba MS7001FA gas turbine with axial annular diffuser (Toshiba©) .....	6
Figure 2.8: Geometry of a conical diffuser (Fleige, 2002).....	7
Figure 2.10: Ideal pressure recovery coefficient (Fleige, 2002).....	8
Figure 3.1: Test facility layout .....	14
Figure 3.2: Test facility .....	15
Figure 3.3: Inlet part of the test facility .....	16
Figure 3.4: Fan for the leakage flow.....	16
Figure 3.5: Spoke wheels and a bladed wheel.....	17
Figure 3.6: Test facility at St. Petersburg State Technical University .....	18
Figure 3.7: Comparison of ideal pressure recovery for two diffusers .....	20
Figure 4.1: PIV working principle (Raffel et al., 2007) .....	21
Figure 4.2: PIV measuring system .....	23
Figure 4.3: Laser endoscope in diffuser test rig .....	25
Figure 4.4: Camera endoscope .....	25
Figure 5.1: Measurement setup, view 1.....	27
Figure 5.2: Measurement setup, view 2.....	28
Figure 5.3: Velocity definition behind NACA-bladed wheel.....	28
Figure 5.4: Comparison of PIV and pneumatic probes at the annular diffuser inlet.....	30
Figure 6.1: PIV configuration 1.....	33
Figure 6.2: PIV configuration 1, fragment .....	33
Figure 6.3: Velocity at diffuser inlet, Sieker .....	33
Figure 6.4: Velocity at diffuser inlet, Sieker .....	33
Figure 6.5: Velocity at 50% diffuser length.....	34
Figure 6.6: Comparison of measurements.....	34
Figure 6.7: Averaged velocity field, design point .....	35
Figure 6.8: Averaged velocity field, partial load.....	35

Figure 6.9: Averaged velocity field, overload .....	35
Figure 6.10: Axial RMS velocity, Sieker .....	36
Figure 6.11: Tangential RMS velocity, Sieker .....	36
Figure 6.12: RMS velocity field, design point .....	36
Figure 6.13: RMS velocity field, partial load.....	36
Figure 6.14: RMS velocity field, overload.....	37
Figure 6.15: Averaged vorticity field, design point .....	37
Figure 6.16: Averaged vorticity field, partial load .....	37
Figure 6.17: Averaged vorticity field, overload .....	38
Figure 6.18: Vorticity extracted from PIV data.....	38
Figure 6.19: RMS velocity extracted from PIV data.....	38
Figure 6.20: Single vorticity field 1, design point.....	39
Figure 6.21: Single vorticity field 2, design point.....	39
Figure 6.22: Single vorticity field 1, partial load .....	39
Figure 6.23: Single vorticity field 2, partial load .....	39
Figure 6.24: Single vorticity field 1, overload.....	40
Figure 6.25: Single vorticity field 2, overload.....	40
Figure 6.26: PIV configuration 2.....	41
Figure 6.27: PIV configuration 2, fragment .....	41
Figure 6.28: Velocity field behind the wheel, design point, 2500 rpm .....	42
Figure 6.29: Velocity field behind the wheel, partial load, 2500 rpm.....	43
Figure 6.30: Velocity field behind the wheel, overload, 1500 rpm.....	43
Figure 6.31: PIV configuration 3.....	44
Figure 6.32: PIV configuration 3, fragment .....	44
Figure 6.33: Averaged and single vorticity fields behind the rotating bladed wheel.....	45
Figure 6.34: Blade wake in the core flow in terms of velocity magnitude.....	46
Figure 6.35: Blade wake in the core flow in terms of vorticity.....	46
Figure 6.36: Vortex diameter vs. swirl angle .....	47
Figure 6.37: Vorticity in the wake vs. swirl angle .....	47
Figure 7.1: Measurement setup .....	50
Figure 7.2: Axial velocity at the inlet of annular diffuser vs. swirl angle, $Ma=0.1$ .....	50
Figure 7.3: Tangential velocity at the inlet of annular diffuser vs. swirl angle, $Ma=0.1$ .....	50
Figure 7.4: Axial velocity at the inlet of annular diffuser vs. swirl angle, $Ma=0.12$ .....	51
Figure 7.5: Tangential velocity at the inlet of annular diffuser vs. swirl angle, $Ma=0.12$ .....	51
Figure 7.6: Axial velocity at the outlet of annular diffuser vs. swirl angle, $Ma=0.1$ .....	51
Figure 7.7: Tangential velocity at the outlet of annular diffuser vs. swirl angle, $Ma=0.1$ .....	51
Figure 7.8: Axial velocity at the outlet of annular diffuser vs. swirl angle, $Ma=0.12$ .....	52
Figure 7.9: Tangential velocity at the outlet of annular diffuser vs. swirl angle, $Ma=0.12$ .....	52
Figure 7.10: Axial velocity, outlet of conical diffuser vs. swirl angle, $Ma=0.1$ .....	53
Figure 7.11: Tangential velocity, outlet of conical diffuser vs. swirl angle, $Ma=0.1$ .....	53
Figure 7.12: Turbulent kinetic energy, outlet of conical diffuser vs. swirl angle, $Ma=0.1$ .....	53
Figure 7.13: Measurement setup .....	53
Figure 7.14: Axial velocity, outlet of conical diffuser vs. swirl angle, $Ma=0.12$ .....	54
Figure 7.15: Tangential velocity, outlet of conical diffuser vs. swirl angle, $Ma=0.12$ .....	54
Figure 7.16: Turbulent kinetic energy, outlet of conical diffuser vs. swirl angle, $Ma=0.12$ ....	54
Figure 7.17: Measurement setup .....	54
Figure 7.18: Pressure recovery for the whole diffuser vs. swirl angle and mass flow .....	55
Figure 7.19: Kinetic energy for the whole diffuser vs. swirl angle and mass flow .....	55
Figure 7.20: Total pressure loss for the whole diffuser vs. swirl angle and mass flow.....	55
Figure 7.21: Axial velocity at the annular diffuser inlet vs. swirl angle .....	56
Figure 7.22: Tangential velocity at the annular diffuser inlet vs. swirl angle .....	56



Figure 7.23: Axial velocity at the ring diffuser outlet vs. swirl angle .....	57
Figure 7.24: Tangential velocity at the ring diffuser outlet vs. swirl angle.....	57
Figure 7.25: Pressure recovery for the whole diffuser vs. swirl angle .....	57
Figure 7.26: Velocity at the ring diffuser inlet vs. swirl angle (Chernikov, 2008) .....	58
Figure 7.27: Velocity at the ring diffuser inlet vs. swirl angle (Chernikov, 2008) .....	58
Figure 7.28: Pressure recovery, whole diffuser, vs. swirl angle and mass flow, comparison ..	59
Figure 9.1: Time-resolved blade wake .....	67

## List of Tables

Table 2. Geometric parameters of the diffuser test rig at SPSTU .....	19
Table 3. Geometric parameters of the diffuser test rig, SPSTU considering modular design..	20
Table 4. Operating points for configurations 1 and 2.....	32
Table 5. Operating points for configuration 3 .....	45
Table 6. Operating points NACA rotor + tip leakage flow .....	49
Table 7. Operating points tip leakage flow.....	56

## List of Symbols

A	[m <sup>2</sup> ]	cross section
AR	[-]	area ratio
c	[m/s]	velocity
c <sub>p</sub>	[-]	pressure recovery coefficient
D	[mm]	diameter
d <sub>hydr</sub>	[mm]	hydraulic diameter
h	[mm]	channel height (for the annular diffuser)
J	[-]	kinetic energy coefficient
k	[m <sup>2</sup> /s <sup>2</sup> ]	turbulent kinetic energy
L	[mm]	length of diffuser
L*	[-]	dimensionless length of diffuser
Ma	[-]	Mach number at the diffuser inlet
$\dot{m}$	[kg/s]	mass flow
n	[rpm]	rotational speed of the bladed wheel
p	[Pa]	pressure
q	[Pa]	dynamic pressure
Re, = (c·d <sub>hydr.</sub> )/ν	[-]	Reynolds number
R	[mm]	outer radius of the channel (for the conical diffuser)
St	[-]	Strouhal number
U	[m/s]	circumferential velocity of bladed wheel
Y	[-]	total pressure loss coefficient
φ	[-]	flow coefficient
α	[°]	swirl angle
ω <sub>z</sub>	[1/s]	the out-of-XY-plane vorticity
ρ	[kg/m <sup>3</sup> ]	density
θ	[°]	diffuser half cone angle
ν	[-]	hub ratio, R <sub>i</sub> is the inner radius, R <sub>out</sub> is the outer radius
σ	[-]	variance
Ω	[-]	vortex street vector
ν	[m <sup>2</sup> /s]	kinematic viscosity

## Subscripts

'	fluctuation
1	inlet
2	outlet
ax	axial
ann	annular
con	conical
Euler	Eulerian radius
i	ideal
l	leakage
r	radial
tg	tangential
tot	total
δ	swirl angle in the leakage flow

# 1. Introduction

Exhaust diffusers are installed behind the last turbine stage of stationary gas turbines, including gas turbines used in combined power plants upstream of the heat recovery steam generator (see Fig. 2.1). The purpose of an exhaust diffuser is to guide the turbine exhaust flow to the heat exchanger in order to recover thermal energy from it. Due to the flow passing through the diffuser, the pressure in the flow increases and the velocity decreases. The diffuser thus increases the enthalpy change in the turbine and makes the combined cycle plant work more efficient.

Geometrically, diffusers are axi-symmetric channels, in which the cross-sectional area increases with its length. Diffusers consist of an annular and a conical part. The hub in the annular part is needed to accommodate the rear bearing of the turbine rotor and is supported with struts connecting it to the casing. The conical part connects the annular part with the downstream units. The geometry of diffusers is discussed in section 2.2. The performance of diffusers is traditionally measured with the pressure recovery coefficient,  $c_p$ , showing which portion of the dynamic pressure in the diffuser inlet flow was transformed into static pressure in the diffuser.

Improving diffuser performance by optimizing its design has been the main goal of this research. Design optimisation of a diffuser requires consideration of the turbine working conditions as shown by Kruse and Quest (1982) and Sieker and Seume (2008). When the load at the gas turbine is changed, the mass flow changes and the turbine exhaust flow pattern is changed. The incoming flow swirls. The flow in the diffuser is always unsteady due to the operation of the upstream turbine and also can have fluctuations because of the downstream units (e.g. heat exchanger) and the unwanted boundary layer separation from the diffuser walls.

A well-known tool for diffuser design is the work of Sovran and Clomp (1967) which provides performance charts for a range of diffuser geometries but with no consideration of the turbine. The goal of diffuser research since then has been the search for an alternative to the performance charts of Sovran and Clomp for enabling better design of diffusers, which should consider unsteady effects and secondary flows in diffusers.

Although CFD calculations have progressed significantly in recent years, the calculation time for the unsteady approach is still significant. Furthermore, the CFD calculation results require validation with cutting-edge experimental data.

Sieker and Seume (2008) investigated pressure recovery in diffusers using a rotating spoke wheel and a NACA-bladed wheel in order to simulate turbine rotor wakes. It was shown that the flow field as well as the pressure recovery in the annular diffuser strongly depend on the spoke wheel operating conditions. Clarification of these results needed experimental data of unsteady or planar measurement techniques, which can be found in this thesis.

One source of challenges in this the field is highly complicated unsteady processes in the working medium. The flow leaving turbine is highly turbulent, complicated by swirl (mostly at the partial load of turbine), tip leakage flow, and unsteady turbulent structures.

Unsteady structures produced in turbines are three-dimensional and need to be considered using a three-dimensional approach. Selesnev et al. (1986) explains features of the three-dimensional flow in the blade passage which are shown in Fig. 1.1: "Pressure gradient is provided in the blade passage due to the pressure difference on the suction and the pressure side of the blades. At the midspan this gradient does not result in the secondary flows because it is compensated by dynamic forces. At the endwalls, on the surface of stator or rotor, the flow is slower in the boundary layer for the same pressures. Therefore flow is moving from the pressure side to the suction side, forming a horseshoe vortex in the root and in the tip regions of the blade. The leakage over the blade tip is counteracting this vortex while transferring the boundary layer, however. Finally, the flow direction is changed in the root and in the tip regions and pressure losses take place due to vortex formation."

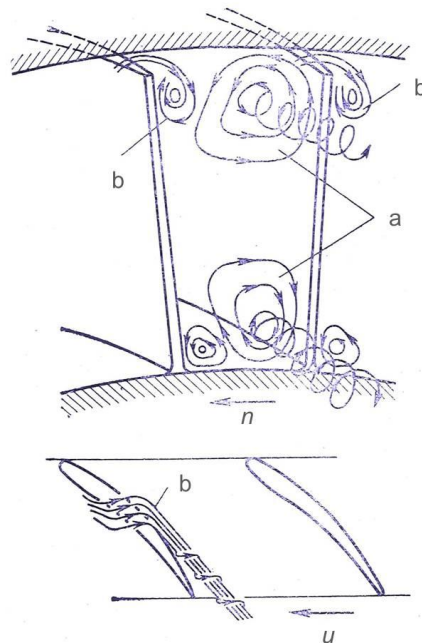


**Figure 1.1: Secondary flows; a: blade passage, b: tip leakage (Selesnev et al., 1986)**

Intensive research has been carried out on the secondary flow and interaction of vortices in turbine flows in order to understand the loss sources and to optimize the turbine. The work of Schlienger et al. (2005) provides analysis of the flow structure at the exit plane behind the first turbine stage. The hub passage vortex and secondary flows from the stator were found to be dominating. Schlienger et al. state that effects like clocking of the first stator blade row have the potential to influence secondary flows and thus the flow structure downstream of the rotor, causing incidence and fluctuations.

The three-dimensional flow structure behind a turbine rotor was studied experimentally by Ristic et al., (1999) using three-dimensional laser Doppler velocimetry on an axial flow turbine test rig. Ristic et al. found the casing-half secondary flow to be strongly influenced by

the tip leakage flow. Major difference between the leakage vortex studied in cascades and in the rotor was found, highlighting the importance of tests on rotating test rigs. However, Ristic et al. found the influence of secondary flow to overshadow those of the leakage and of the other effects from the midspan to 95% of the channel height. They stated that the secondary flow reduced the spreading of the tip vortex and stated that the vorticity field was dominated mainly by it. Radial flows in the wake are found growing due to the secondary flow and the rotation effect. Basically, much higher distortion of the flow pattern by secondary flows and tip leakage flow was found in the rotor wake pattern than in the nozzle wake.

Application of the newest measurement techniques is a common approach in the experimental research on diffusers as well as on the other turbomachinery units. The endoscopic Particle Image Velocimetry (PIV) method is applied in the present work in combination with pneumatic measurement techniques for the investigation of diffuser flow conditions. While being in development for 25 years, PIV has been used in turbomachinery tests for just several years. The current PIV approach stands out due to the implementation of a “rotating” test rig and use of endoscopes for both laser and camera such that there is no need for windows matched to the test rig’s surfaces.

Chernikov (2008) studied diffuser performance under changes in load on an air supplied turbine stage. A precise scale model of the last turbine stage was used to generate the inflow into the diffuser. Chernikov found a significant influence of the turbine operating mode on the diffuser characteristics and considered the interaction of the tip leakage flow with the secondary flows to be important for the flow phenomena.

The similarity of geometric parameters of the test rig used in the current research and those of Chernikov allows comparison though it is limited by the technical boundary conditions (geometry of the test rigs, limits of modeling at the test rig). The diffuser test rig in the current research is a geometrically scaled model of a real turbine exhaust diffuser for which nearly all flow parameters can be easily modified. By contrast, the diffuser test rig of Chernikov is closer to real turbine exhaust diffuser conditions and possesses a scaled model of a turbine stage with two rows of guide vanes, in which flow parameters cannot be easily modified. A dimensionless comparison of results confirms the relevance of the dimensionless parameters and validates the results.

## 2. Interaction between Turbine and Exhaust Diffuser

### 2.1. Purpose of a diffuser behind a turbine

Gas turbine exhaust diffusers are installed behind the last turbine stage of stationary gas turbines, including gas turbines used in combined power plants, and upstream of the HRSG (heat recovery steam generator). A layout of a typical combined power plant system is shown in Fig. 2.1.

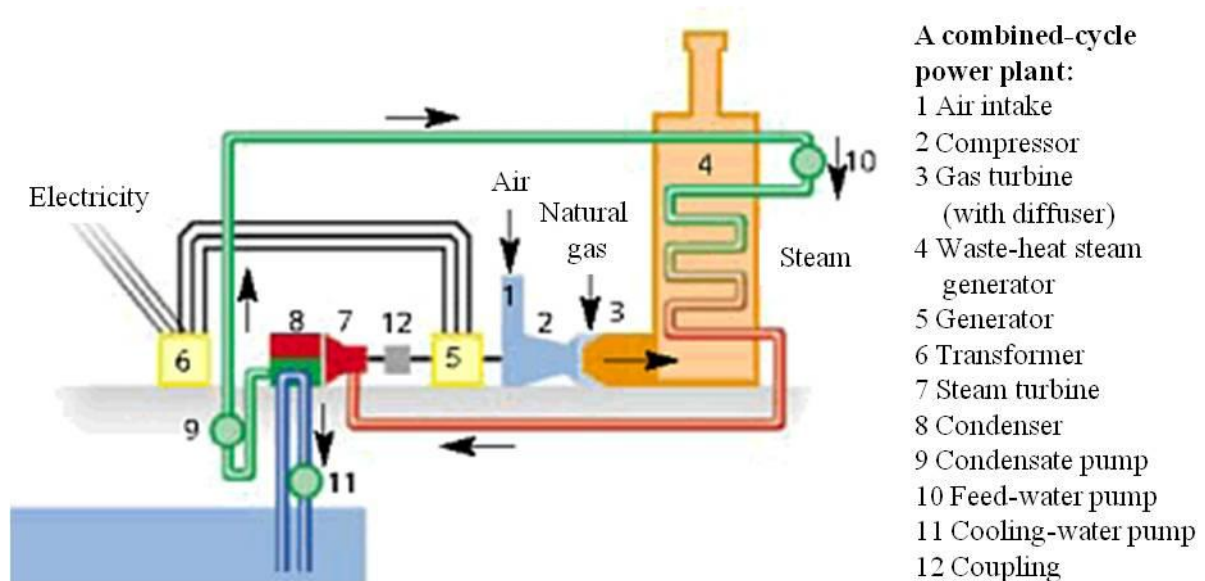


Figure 2.1: Typical combined power plant layout (Siemens, [www.siemens.com](http://www.siemens.com))

The purpose of an exhaust diffuser is to guide the turbine exhaust flow to the heat exchanger that is the HRSG while recovering energy from it. A part of the kinetic energy of the exhaust is transformed into static pressure.

The h-s diagram in Fig. 2.2 shows the expansion process in a turbine with and without a diffuser. The gas enters the turbine in point 1 with parameters static pressure  $p_1$  and velocity  $c_1$ . Without a diffuser, gas can only expand to the pressure  $p_2$  equal to  $p_u$ , while the energy of the flow leaving the turbine is not utilized. If a diffuser is applied, gas can expand to point 3 with pressure  $p_3$  and velocity  $c_2$ . Kinetic energy of the flow leaving the diffuser is then lower than in the first case. The enthalpy difference between points 1 and 3 is greater and thus a bigger part of the available energy can be utilized in the turbine.

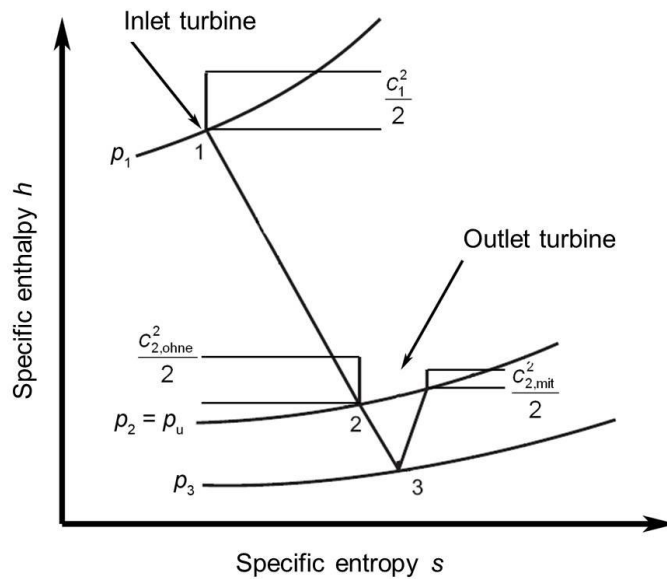


Figure 2.2: Turbine process in h-s diagram

Axial exhaust diffusers can be found in the newest Siemens H class turbine SGT5-8000H as described by Fischer (2010). GE employs axial diffusers in their F-class heavy duty gas turbines. In the GE B- and E-class turbines radial diffusers are used, Balevic, (2009).

## 2.2. Geometric parameters of diffusers

Geometrically, diffusers are channels for which the cross-sectional area increases with the channel's length. Axial, radial, and axial-radial diffusers are applied behind industrial turbines, as shown in Fig. 2.3 and Fig 2.4.

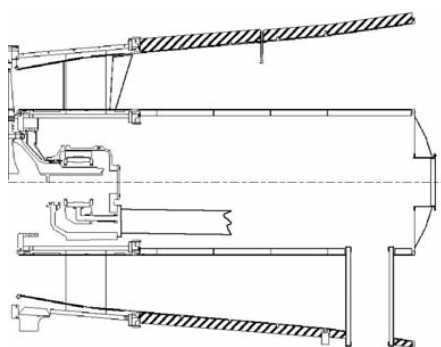


Figure 2.3: F-Class axial diffuser (GE)

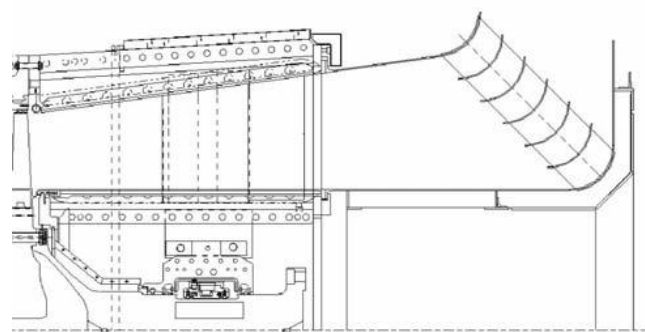
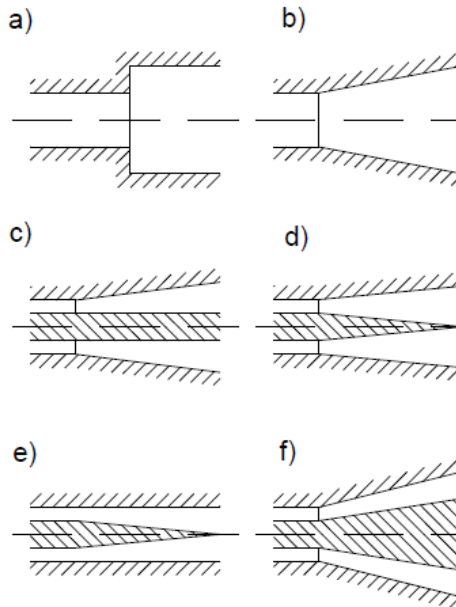


Figure 2.4: E-Class radial diffuser (GE)

Axial diffusers can be divided into annular diffusers which have a form of an annulus due to the hub inside and conical diffusers which have a simple form of a cone. The hub in the annular part is needed to accommodate the rear bearing of the turbine rotor and it is supported with struts connecting it to the casing. Diffusers with a rectangular cross-section and diffusers with a curved axis also exist. In Fig. 2.5 different geometries are shown for axial diffusers.



**Figure 2.5: Basic diffuser geometries (Fleige, 2002)**

An abrupt enlargement of the cross section of a channel is known as a Carnot diffuser (a). (b) shows a conical diffuser, (c-f) show annular diffusers with different geometries of the casing and the inner body (hub). In many industrial turbines (Fig. 2.6, 2.7) axial diffusers are applied which consist of an annular and a conical part. The conical part connects the annular part with the downstream units.

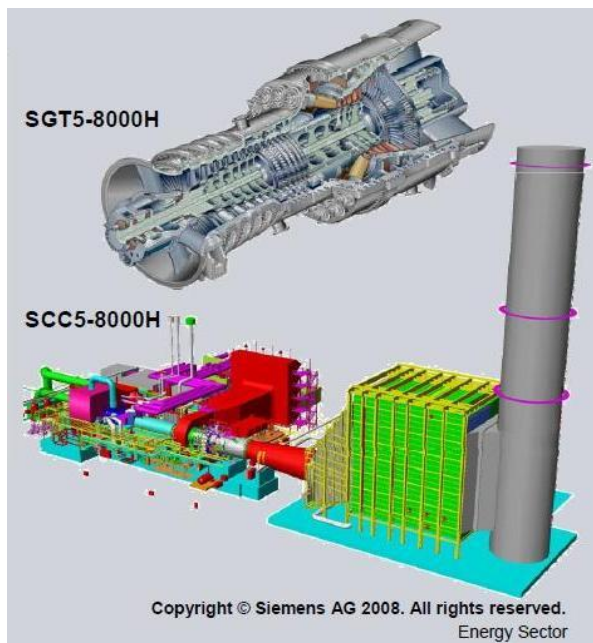


**Figure 2.6: Combined cycle power plant with SGT5-8000H gas turbine (Siemens©)**

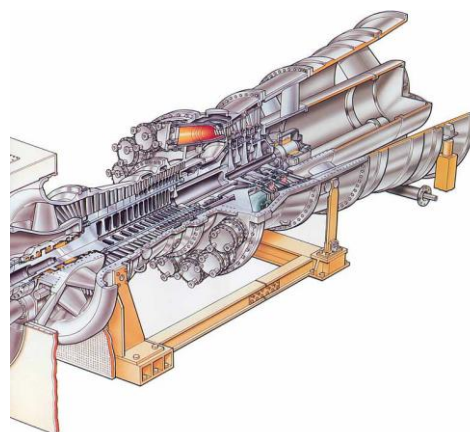


**Figure 2.7: Toshiba MS7001FA gas turbine with axial annular diffuser (Toshiba©)**



A range of dimensionless parameters is used to define the geometry of diffusers. Here, parameters for axial annular and conical diffusers are given. For conical diffusers (Fig. 2.8), one length (L or R) and two geometric similarity parameters are enough to define the geometry. These are, as given by Fleige (2002):

The area ratio between inlet and outlet area:

$$AR = \frac{A_2}{A_1} \quad (1)$$

The dimensionless length which is the channel's length divided by the channel radius in the inlet:

$$L^* = \frac{L}{R} \quad (2)$$

A third parameter can be introduced which is a function of the first two and describes the opening angle of the channel:

$$\tan(\theta) = \frac{\sqrt{AR} - 1}{L^*} \quad (3)$$

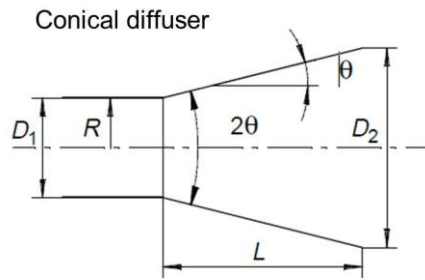


**Figure 2.8: Geometry of a conical diffuser (Fleige, 2002)**

For annular diffusers (Fig. 2.9), four independent similarity parameters define the geometry. These are the area ratio, the dimensionless length, which is defined using the channel height at the inlet of the annular diffuser, the hub ratio and the opening angle. The hub ratio is

$$\nu = \frac{R_i}{R_a} \quad (4)$$

Where  $R_i$  is the inner and  $R_a$  the outer radius of the channel at the inlet. In the case of  $\theta_i = 0$  the opening angle  $\theta_a$  is defined as

$$\tan(\theta_a) = \frac{\sqrt{AR + (1 - AR)\nu^2} - 1}{(1 - \nu)L^*} \quad (5)$$

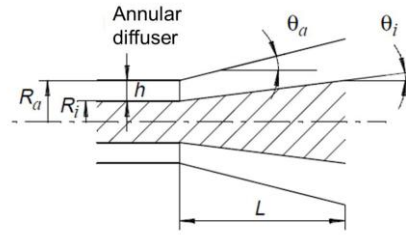


Figure 2.9: Geometry of an annular diffuser (Fleige, 2002)

### 2.3. Performance evaluation of diffusers

Performance of diffusers is defined with the pressure recovery coefficient  $c_p$  showing which part of dynamic pressure in the diffuser inlet flow was transformed in diffuser into static pressure.

The pressure recovery coefficient is defined as

$$c_p = \frac{\overline{p_2 - p_1}}{\overline{p_{tot,1} - p_1}} \quad (6)$$

where  $(p_2 - p_1)$  is the rise of static pressure between the outlet and the inlet of the diffuser and  $(p_{tot,1} - p_1)$  is the dynamic pressure at the inlet.

For estimating the efficiency of diffusers, an ideal pressure recovery coefficient  $c_{pi}$  can be used which depends only on the geometrical parameters. Figure 2.10 shows dependence of the  $c_{pi}$  on the area ratio of the diffuser.

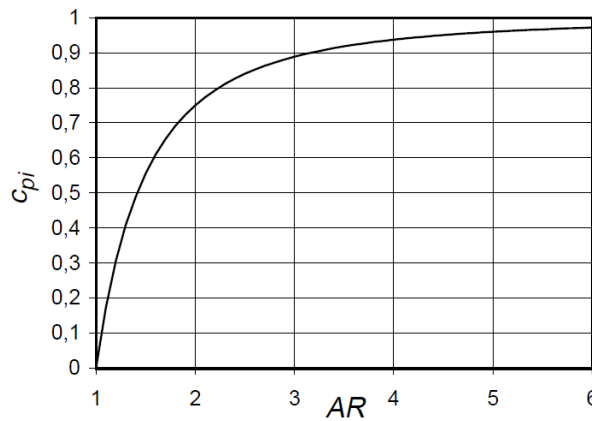


Figure 2.10: Ideal pressure recovery coefficient (Fleige, 2002)

Diffuser performance can be further described using the kinetic energy and total pressure loss coefficients. This approach can be found in Deytch and Zarjankin (1970). The total pressure loss coefficient, which provides information about viscous losses, is defined for incompressible flow as

$$Y = (p_{1tot} - p_{2tot}) / (p_{1tot} - p_1) \quad (7)$$

The kinetic energy coefficient describes the unrecovered part of the kinetic energy and is defined as:

$$J = (p_{2tot} - p_2)/(p_{1tot} - p_1) = q_2 / q_1 \quad (8)$$

The sum of these coefficients shows full losses of exhaust kinetic energy in a diffuser.

The process in diffusers, considering incompressible adiabatic flow along a streamline, can be described by the Bernoulli-equation. Following the dimensionless form of the Bernoulli-equation, the energy balance can be divided into three components which describe the pressure rise ( $C_p$ ), the total pressure loss ( $Y$ ), and the remaining kinetic energy in the outflow ( $J$ ); we introduce  $q$  as dynamic pressure.

$$\frac{(p_2 - p_1)}{q_1} + \frac{(p_{1tot} - p_{2tot})}{q_1} + \frac{(p_{2tot} - p_2)}{q_1} = C_p + Y + J = 1 \quad (9)$$

According to Denton (1993), control volume analysis can be used to evaluate the loss generation budget in the tested diffuser. An important feature of the energy is that its total flux along the stream-tube must be constant and the viscous loss can be obtained from the energy balance without the measurement of the total pressure. Accordingly, we can evaluate the total pressure coefficient from the energy balance correlation for the control volume consisting of the stream-tube between the inlet and the outlet sections of the diffuser where the flow parameters are known. For the current diffuser test rig, the corresponding measurement positions are at the inlet of the annular diffuser and the outlet of the conical diffuser.

Hence we get:

$$Y = 1 - C_p - J \quad (10)$$

where  $C_p$  and  $J$  are calculated using averaged measured parameters of the stream-tubes.

Analysis of CFD-computational results by Fleige (2002) shows that the influence of the radial velocity component on the overall diffuser performance is negligible. Hence, we can assume that the radial velocity is equal to zero. Resultantly, from the correlation

$$c^2 = c_{ax}^2 + c_{tg}^2 \quad (11)$$

we get

$$q_1 = q_{1ax} + q_{1tg} = q_{1ax} / \cos^2 \alpha \quad (12)$$

Therefore, the kinetic energy coefficient can be divided into two parts which describe the unrecovered part of the kinetic energy in the swirl and the meridional motion.

$$J = (q_{2ax} + q_{2tg}) / q_1 = J_{ax} + J_{tg} \quad (13)$$

## 2.4. Design of exhaust diffusers considering the upstream turbine

A well-known tool for diffuser design is the work of Sovran and Clomp (1967) which provides performance charts for a range of diffuser geometries but with no consideration of the turbine. The flow was considered to be non-swirled and the boundary layer to be very thin (Sieker). The goal of diffuser research since then has been searching for alternatives to the

performance charts of Sovran and Clomp for better designing of diffusers, which should consider unsteady effects and non-uniform flow going into the diffuser.

Walsh (2004) gives guidelines for the design point of industrial gas turbine engine exhaust flow. According to Walsh, as the power turbine must operate synchronously, changes up to 30° between base load and synchronous idle are typical in power generation and exit swirl angle changes may be large at the off-design conditions. According to Walsh, the optimum inlet swirl angle for duct types which commonly occur downstream of turbines is on the order of 15°.

According to Walsh, the final stage turbine exit swirl angle (at the design point) should be less than 20° and ideally 5° on the pitch line. The final stage exit Mach number should be around 0.3 and not higher than 0.55 above which dramatic breakdown in flow may occur in exhaust diffusers. Conical diffuser exhaust systems should have a cone included angle as close to 6° as possible within the installation space constraints. For diffusers there is a little additional static pressure recovery in going beyond an area ratio of 2:1, and none in going beyond 3:1.

Logan and Roy (2003) state that even with the recent advantages in general-use CFD tools, analytical prediction of diffuser recovery is not normally performed as part of preliminary turbine design, and diffuser performance is normally obtained from empirically derived plots such as of Sovran and Klomp (1967).

Logan and Roy (2003) found an almost 6% increase in overall turbine efficiency due to the inclusion of a diffuser, comparing the overall efficiency including inlet and exit losses of a turbine without a diffuser to a turbine with a diffuser. They state that a large amount of energy is contained in turbine exhaust and the efficiency gain associated with a diffuser is dependent on pressure recovery, rotor exit Mach number (as it increases the advantages gained by including a diffuser) and overall pressure ratio.

Improving diffuser performance by optimizing its design is the main goal. The theory that the design optimisation of a diffuser requires the consideration of the turbine working conditions can be found in Kruse and Quest (1982). When the load at the gas turbine is changed, the mass flow changes and the turbine exhaust flow pattern changes. The incoming flow swirls. The flow in a diffuser is always unsteady due to the operation of the upstream turbine and also can have fluctuations because of the downstream units (e.g. heat exchanger) and because of the unwanted boundary layer separation from the diffuser walls.

Due to the turbine operation, diffuser flow is provided with flow structures which enter the diffuser from the turbine. As observed by others and in the present work, these structures, which result in large-, middle- and small-scaled turbulence, change the diffuser's performance, influencing the boundary layer of the diffuser. Blade wakes are large-scaled structures, which originate on trailing edges of turbine blades.

Vassiliev et al. (2008) studied the dependence of swirl on the pressure recovery in diffusers gained with refitting the exhaust diffuser of an existing industrial gas turbine by adapting it to the increased mass flow through changing the residual swirl at the turbine outlet through matching of diffuser struts. Experiments showed that pressure recovery in the refitted diffuser

depended on the inlet of swirl angle, and maximum recovery has been achieved at design conditions with swirl angle about  $0 - 10^\circ$ .

In order to determine the performance of various strut configurations over a wide range of inlet swirl conditions, Feldcamp and Birk (2006) experimentally investigated the overall influence of struts spanning an annular diffuser followed by a straight cored annular diffuser. The results of Feldcamp and Birk show that the presence of struts for the non-swirled flow has a relatively small effect on the overall total pressure loss, while with the inlet swirl angle of  $20^\circ$  the struts are able to assist in recovery of the swirling flow.

Numerical investigation of the diffusers has progressed in the last years. An extensive numerical investigation of the impact of blade wakes was provided by Kluß et al. (2009). This research with the commercial solver ANSYS CFX-10.0 has shown that only an unsteady approach with the shear stress transport turbulence model is capable of predicting the stabilizing effect of the rotating wheel on the diffuser flow. It was suggested that the mixing effect of wakes and secondary flow patterns is responsible for flow reattachment. However, the calculation time for the unsteady approach is significant (up to a few weeks computer time). The CFD calculation results require validation with cutting-edge experimental data.

A numerical study of gas turbine exhaust diffusers made by Pradeep et al. (2010) for two inlet swirl conditions and several annular diffuser's geometries showed that the performance worsened with higher inlet swirl and that the divergence angle in the annular part of the diffuser plays an important role in the initiation of flow separation. According to Pradeep, the best performance in terms of static pressure recovery and total pressure losses can be achieved for a design with a mild initial diffusion, followed by aggressive diffusion up to the maximum thickness location of the struts.

Extensive research of Vasiliev et. al (2010) on the impact of the inlet flow conditions on the pressure recovery in diffusers showed that non-uniform pressure distribution as compared to a uniform one can lead to better diffuser performance and that moderate residual swirl can also improve the performance. Furthermore, Vasiliev et al. analysed two approaches for minimising exhaust losses in heavy-duty gas turbines: through adjustment of the diffuser geometry to cope with the given inflow conditions and through fitting the inflow conditions to a given diffuser geometry.

Extensive research on exhaust diffusers was conducted at the TFD, Leibniz Universität Hannover. The diffuser test rig built by Fleige (2002) was used as a test facility. Fleige, Riess, and Seume (2002) investigated diffusers by experimentally and numerically varying the swirl angle produced by a static swirl generator in the form of vanes and using three strut configurations and a simulated tip leakage flow. Pressure recovery was found to decrease due to the presence of struts, either cylindrical or profiled, although struts reduced the circumferential velocity component and thus prevented a swirl-induced central recirculation zone in the conical diffuser at high ( $>18^\circ$ ) inlet swirl angles. Generally, introduction of tip leakage flow near the casing was found to energize the boundary layer and increase  $c_p$ . The tangential component in the tip leakage flow was found to reduce  $c_p$ . Fleige states that if the swirl in the tip leakage flow and in the main flow superimpose, this reduces  $c_p$ .

Sieker and Seume (2008) investigated the performance of diffusers with a short annular part with aggressive opening angles of  $15^\circ$  and  $20^\circ$  and a rotating turbine stage simulator. They observed high sensitivity of diffusers to changes in the inlet conditions and to the operating point as described below. Sieker and Seume (2008) have shown that a diffuser which would have separated flow according to conventional performance charts (Sovran and Klomp, (1967)) can be stabilized with the unsteady effects produced by turbines; however this effect is not strong enough to prevent separation in diffusers with an opening angle of  $20^\circ$ . Sieker and Seume (2008) showed then that conventional design methods are insufficient for diffuser design.

Sieker and Seume (2008) investigated correlations of pressure recovery in annular and conical diffusers with the swirl number, a dimensionless parameter reflecting the impact of swirl induced by the turbine. The rise of swirl number was found to increase pressure recovery but only for a small dimensionless length of diffuser, while for the rear part of diffuser with further length decrease of pressure recovery was stated. Only the frontal part of conical diffusers could be correlated using swirl angle as a parameter. Stabilizing as well as destabilizing influences of the turbine stage model on the diffuser boundary layer were found. Sieker and Seume's (2008) results show that turbulent energy produced by the operation of the turbine stage simulator with profiled blades can stabilize the boundary layer in diffuser, but they do not clarify the dependence. The flow coefficient applied as a parameter for pressure recovery correlations in the annular diffuser showed a clearer dependence. According to Sieker and Seume (2008), a higher flow coefficient results in higher pressure recovery while its low values result in lower pressure recovery. At the same time, the increase of turbulent kinetic energy at the shroud for tests with negative swirl causes an increase of energy dissipation.

Kuschel and Seume (2011) applied a 3D hot wire probe measurements and unsteady pressure transducers to the exhaust diffuser test rig in order to resolve the unsteady flows and understand their influence on the pressure recovery. Measuring frequency of 50 kHz and a dense measurement grid in the annular diffuser allowed identifying vortices at the tips of the blade wakes for operating conditions with a high flow-coefficient. The number of vortices was found to be lower than the number of blades. It was shown, that the flow field was not isotropic and therefore, an unsteady approach is needed to correctly resolve the diffuser flow numerically.

In this thesis, the research of Sieker and Seume (2008) is continued and expanded by validating their results through comparison with results obtained from experiments on a more gas turbine-like diffuser test rig as well as through extensive application of the high-end measurement technique Endoscopic Particle Image Velocimetry for tests on diffusers.

Chernikov (2008), (2009), studied diffuser performance under changes of the load on an air supplied turbine stage test rig equipped with an exhaust diffuser. A precise scale model of the last turbine stage was used to generate the inflow to the diffuser. Pneumatic 5-hole probes and thermoelectric elements were used for measuring. Chernikov found a significant influence of the turbine operating mode on the diffuser characteristics and considered the interaction of the

tip leakage flow with the secondary flows to explain the phenomena. The highest pressure recovery was found for tests with moderate positive swirl and high kinetic energy in the main flow, while the flow at the hub was almost non-swirled. Chernikov suggested that the main flow vector, the leakage flow vector, and the secondary flow interaction in the close-to-shroud channel part are responsible for flow stabilisation, Fig. 2.11. The vortex street is energized and stabilizes the flow downstream of the diffuser. In Fig. 2.11  $\alpha$  is the swirl angle in the main flow,  $c_{2\delta}$  is the vector of the leakage flow leaving the gap, and  $\Omega$  is the vector of the vortex street.

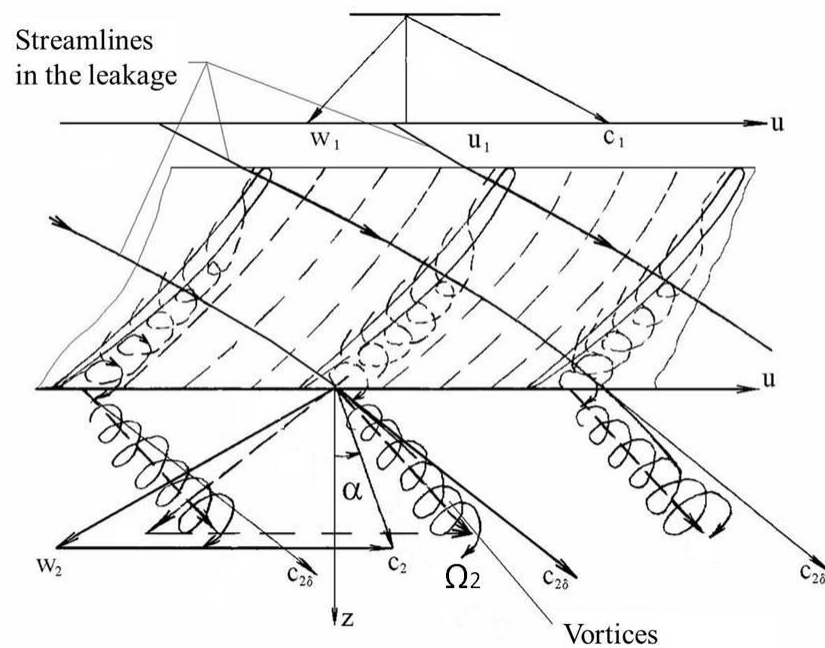


Figure 2.11: Flow in the last rotor stage in a gas turbine at 70% load (Chernikov, 2008)

### 3. Experimental facilities

#### 3.1. Diffuser test rig at the Leibniz Universität Hannover

The diffuser test rig at the Institute of Turbomachinery and Fluid-Dynamics is used for the experimental research. The test rig represents a typical gas turbine exhaust diffuser consisting of two channels: an annular diffuser which is the front part of the whole diffuser, and a conical diffuser, which is the rear part connected to the front part. The whole diffuser is a 1:10 scaled model of an industrial gas turbine exhaust diffuser.

Ambient air is used as the working medium. This air is sucked from the laboratory into the diffusers and is blown out into the laboratory.

In 2002 the test rig was designed and built up by Fleige (2002) “in order to conduct cold air flow measurements to investigate the effects of flow phenomena on diffuser performance”. Between 2005 and 2009 the test rig was operated and developed further by Sieker and Seume (2008) while the range of its modelling capacities grew.

The main advantage of the test rig is its modular design and availability of adjustments explained below which allow varying of diffuser flow parameters. Moreover, the influence of different flow phenomena (swirl angle of the inlet flow, tip leakage flow, turbulence, high-scaled unsteady effects – blade wakes and vortices, Mach number and Reynolds number in a limited range) can be “separated” for studying, which can be harder to achieve on more gas turbine-like test rigs. The test rig is shown in Fig. 3.1 and 3.2. Fig. 3.1 shows a general sketch of the test rig. Fig. 3.2 represents the test rig.

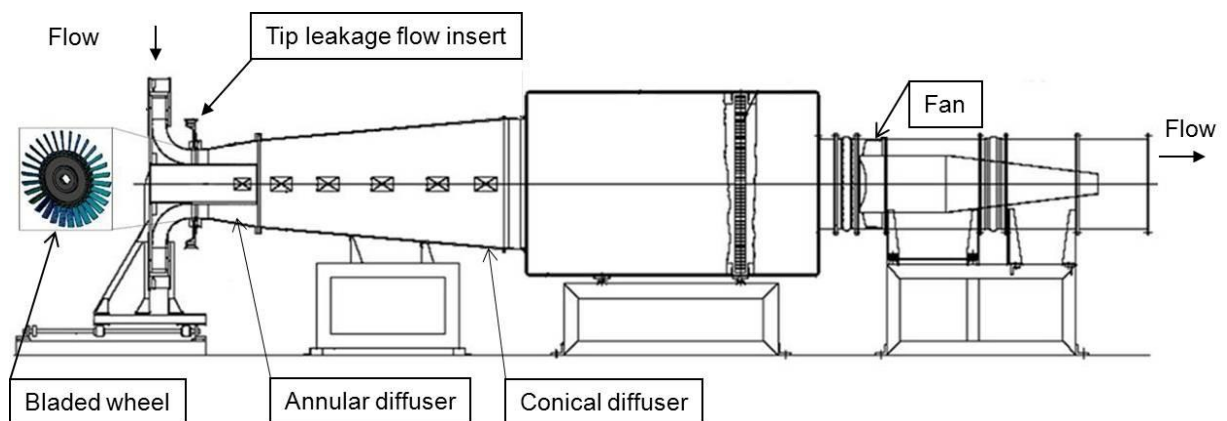


Figure 3.1: Test facility layout





**Figure 3.2: Test facility**

There are three different replaceable annular diffusers with opening half-cone angles of  $10^\circ$ ,  $15^\circ$ , or  $20^\circ$ . The first one was built by Fleige as a typical fitting in the performance charts of Sovran and Clomp (1967) while others were built by Sieker (Sieker and Seume 2008) in order to investigate the potential of shorter diffusers. Shorter diffusers were introduced to clarify if it is possible to save place in the power plant by reducing the diffuser length with non-reduced or improved performance. Annular diffusers consist of a transparent casing and an aluminium hub. The casing possesses flanges connecting it to the inlet duct and the conical diffuser. The conical diffuser is welded from steel sheets and has an opening angle of  $5^\circ$ . Depending on the annular part, the length of the whole diffuser is up to 2.07 m. The diameter of the annular diffuser inlet is 480 mm, the diameter of its outlet is 600 mm and the diameter of the conical diffuser outlet is 900 mm. Dimensionless geometric parameters of the diffusers can be found in section 3.3 “Geometric parameters of the diffuser test rigs” where they are used for comparison with the geometric parameters of the diffuser test rig of the TU St. Petersburg which was used for validation.

Struts in the annular diffuser which support the rear bearing of the turbine shaft are not essential for the test rig design. Nevertheless struts can be installed in the diffuser and there have been tests with different strut geometries like symmetrically profiled and circular cross-section struts, Fleige et al. (2002).

The conical diffuser is connected to a settling chamber which has a door on its right side allowing entrance for maintenance. Inside the chamber there is a metal honeycomb grid to straighten the flow and destroy large scaled flow structures from the diffuser before they come into the axial fan located downstream.

The 37 kW axial fan provides mass flow through the test rig. The mass flow and therefore the Mach number in the test rig inlet can be adjusted using a frequency converter. The maximum mass flow is 8 kg/s. The maximum mass flow achieved in the current experiments is 6.5 kg/s with a Mach number 0.16 in the diffuser’s entrance.

The inlet duct possesses a swirl generator to bring swirl into the flow. The setup was built by Fleige and is shown in Fig. 3.3. To adjust the swirl in the range of  $-5^\circ$  to  $+25^\circ$ , 30 sheet-metal swirl vanes are installed and are bent by turning the inlet ring. The flow sucked from the

ambient is then turned in the desired direction when passing the setup. So the swirl which occurs in the last turbine stage outflow in the real industrial turbines, with the turbine operating not at the design point, can be modelled. However this system without bladed wheel (explained below) cannot be seen as sufficient for modelling, as the flow is provided with swirl but not with blade wakes, unlike that in the real engine.

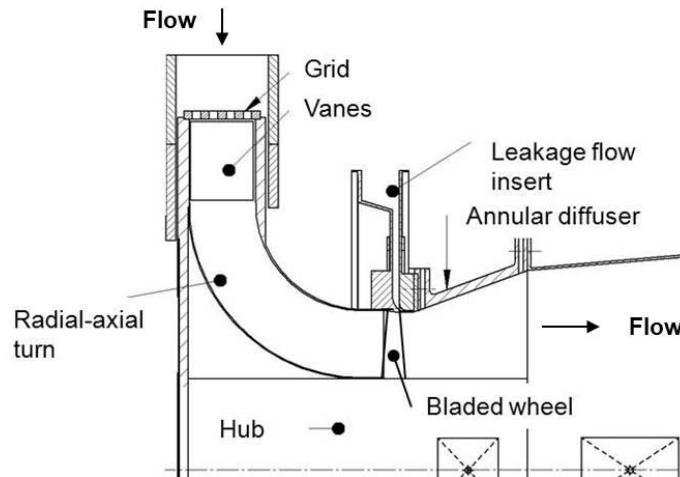


**Figure 3.3: Inlet part of the test facility**

Figure 3.4 shows the tip leakage flow setup. Tip leakage flow can be brought into the flow in the annular diffuser inlet by a ca. 1.5 mm annular gap. In real turbines this flow is a result of the pressure difference before and after the turbine stage which pushes the gas through the axial gap between the tip of the blade and the stator.

The uniform flow is provided through four circumferential, uniformly-distributed, corrugated tubes from an additional 5 kW centrifugal fan with adjustable frequency. In order to vary swirl in the leakage flow in a range of  $\pm 25^\circ$ , a similar set-up as for the swirl generator in the main flow is used. The further information to the construction of this setup can be found in Fleige (2002).



**Figure 3.4: Fan for the leakage flow**

The flow provided with unsteady effects typical for turbo machines can be provided in diffuser test rig with a feature introduced by Sieker. Sieker and Seume (2008) implemented a rotating spoke/bladed wheel in the inlet of the annular diffuser (Fig. 3.3) which simulates the flow conditions coming from the last turbine stage. At least three different types of spokes

and one type of blade which can be installed in the disk are shown in Fig. 3.5. The rotational speed of the wheel is variable up to 3000 rpm and is provided by a separate 4 kW electric motor with a frequency converter. The rotational speed can be set up between 100 and 3000 rpm. The bladed wheel can be used independently to the “mechanical” swirl generator. Sieker and Seume (2008) explain the choice of blade profile by the impracticality of scaled turbine blades firstly due to the limited swirl angle achievable with the swirl generator upstream of the wheel and secondly due to the fact that the motor is not capable of dissipating the resulting amount of power. For the current research a symmetrical NACA-0020 bladed spoke wheel was used.

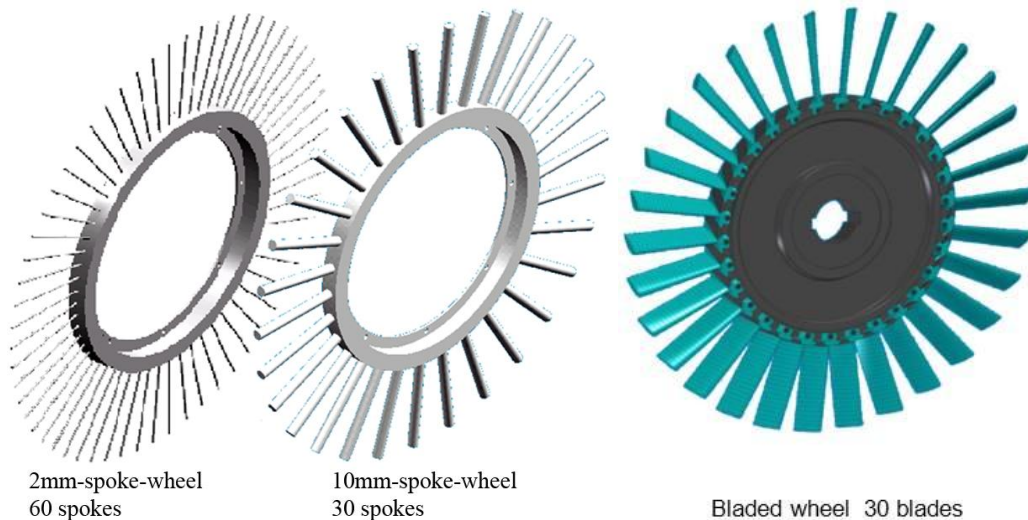


**Figure 3.5: Spoke wheels and a bladed wheel**

### **3.2. The test rig at St. Petersburg State Technical University**

The research of Chernikov is done with a test rig which on the one hand possesses a geometry similar to that of the diffuser test rig at the TFD and on the other hand possesses a scaled turbine stage. According to the methodology of Chernikov (2008), the geometrical similarity of the turbine stage model is so complete that the most important dimensions of the original stage are provided in the model stage, including various radial and axial clearances and the relative roughness of the surface. According to Chernikov, “a precisely scaled last stage generates inlet boundary conditions corresponding to those of the turbine”, meeting the kinematic and dynamic dimensionless parameters. According to Chernikov, if the similarity criteria are met for the turbine stage, similarity of the diffuser inlet flow is achieved.

Data used for comparison in the present research are coming from tests on a model of the exhaust diffuser without struts for mass flow of 5, 7.5, and 10 kg/s, varying the swirl angle in the turbine outlet flow from 60° to 100°. Pressure recovery values for the control sections are calculated using results of averaging and the conservation equations.

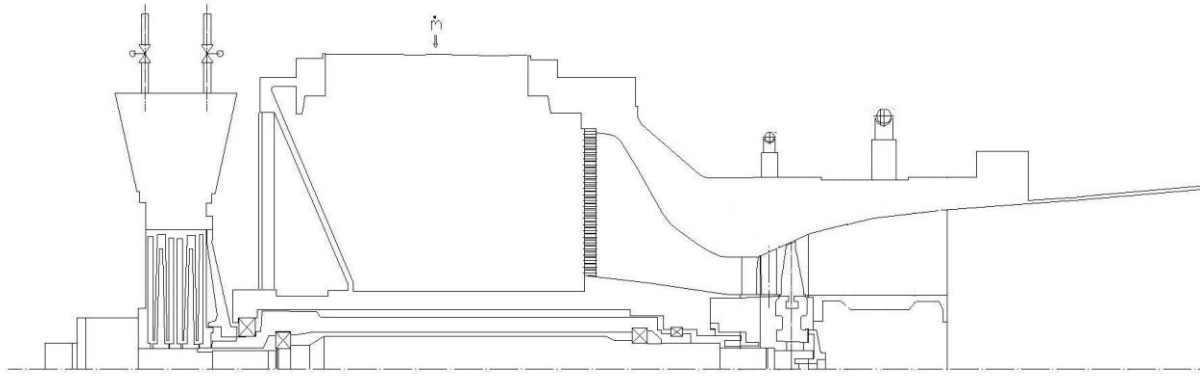


**Figure 3.6: Test facility at St. Petersburg State Technical University**

Figure 3.6 shows a longitudinal cross section of the test rig. According to Chernikov, the main components of the test rig are the air turbine and the model of an exhaust diffuser. The model is constructed with at the scaling factor of 8.0. The diffuser has an annular section restricted at the shroud by a contour with opening angles of  $24^\circ$ ,  $15^\circ$  and  $7^\circ$ . Parameters at the inlet of the annular diffuser and the outlet of the conical diffuser are used. The conical diffuser has an opening angle of  $5^\circ$ .

According to Chernikov, the annular exhaust diffuser can be adjusted with five supporting pillars of a constant cross section, followed by the conical section. Traversing of the control cross sections by measuring the pressure field, velocities, and temperatures of the flow is performed by means of five-hole conical pneumatic probes with 2.4 mm diameter heads designed in St. Petersburg State Polytechnical University, and five-hole cylindrical pneumatic probes with a 4.6 mm head diameter and a built-in thermoelectric element designed by United Sensor (United States).

Evaluation of the gas-dynamic properties of diffusers is based on the pressure recovery coefficient, where averaged values of the pressure, density, and flow velocity at the diffuser inlet and the averaged pressure at the diffuser outlet are applied.

### 3.3. Geometric parameters of the diffuser test rigs

To be able to compare different diffuser geometries, geometric parameters are needed. These are given in Tables 1 and 2 for diffuser test rigs of the present research and at SPbSTU, respectively. When the modular design of the latter test rig is taken into account, parameters are as shown in Table 3. “With hub” in Table 2 means that the annular diffuser’s outlet area is used for calculation of the parameter; “no hub” means that the conical diffuser’s inlet area is used.

**Table 1. Geometric parameters of the diffuser test rig, Leibniz Universität Hannover**

Diffuser	Area ratio AR [-]	Dimensionless length $L_{ann}^*$ ; $L_{con}^*$ [-]	$\nu$ [-]	Opening angle $\Theta_a$ [°]
15° annular diffuser	1.93	2.42	0.59	15
Conical diffuser	2.25/2.88	10.8/5.8	-	<u>5</u>
Diffuser	5.54	-	-	-

**Table 2. Geometric parameters of the diffuser test rig at SPSTU**

Diffuser	Area ratio AR [-] (“no hub”)	Area ratio AR [-] (“with hub”)	Dimensionless length $L_{ann}^*$ ; $L_{con}^*$ [-] (“no hub”)	Dimensionless length $L_{ann}^*$ ; $L_{con}^*$ [-] (“with hub”)	$\nu$ [-]	Opening angle $\Theta_a$ [°]
15° annular diffuser	1.43	1.61	2.38	-	0.55	10.26
Conical diffuser	2.4	3.05	12.03	6.51	-	4.8
Diffuser	4.9	-	-	-	-	-

**Table 3. Geometric parameters of the diffuser test rig, SPSTU considering modular design**

Diffuser	Area ratio AR [-]	Dimensionless length $L_{ann}^*$ ; $L_{con}^*$ [-]	$\nu$ [-]	Half cone angle $\Theta_a$ [°]
15° annular diffuser (front part)	1.41	1.25	0.55	13.4
15° annular diffuser (rear part)	1.14	0.87	0.48	6.62

Fig. 3.7 gives comparison of ideal pressure recovery for both diffusers. Similarity in diffuser geometries can be noticed.

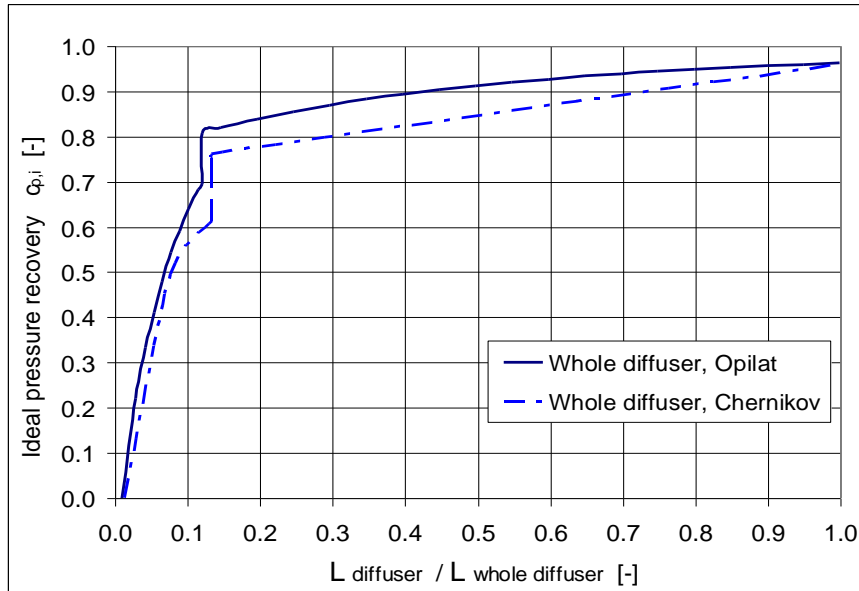


**Figure 3.7: Comparison of ideal pressure recovery for two diffusers**

## 4. PIV Instrumentation

### 4.1. Endoscopic Particle Image Velocimetry (PIV); working principle

The endoscopic PIV measurement technique is a measuring tool which provides velocity data of the flow under investigation. The principle of PIV is to visualise the flow using two pulsed lasers and shown in Fig. 4.1. The laser beams are guided from the laser head through optics which transform them into thin laser sheets which illuminate a measuring plane. The flow is seeded with light-weight light-reflecting particles. The distribution of the illuminated particles in two laser pulses is recorded by a digital camera. As the time between two laser pulses is known, images can be correlated with a software generating velocity fields from the displacement of particles between the two images. Variables such as vorticity, shear, and normal stresses, and effects like vortex shedding can be studied using these fields.

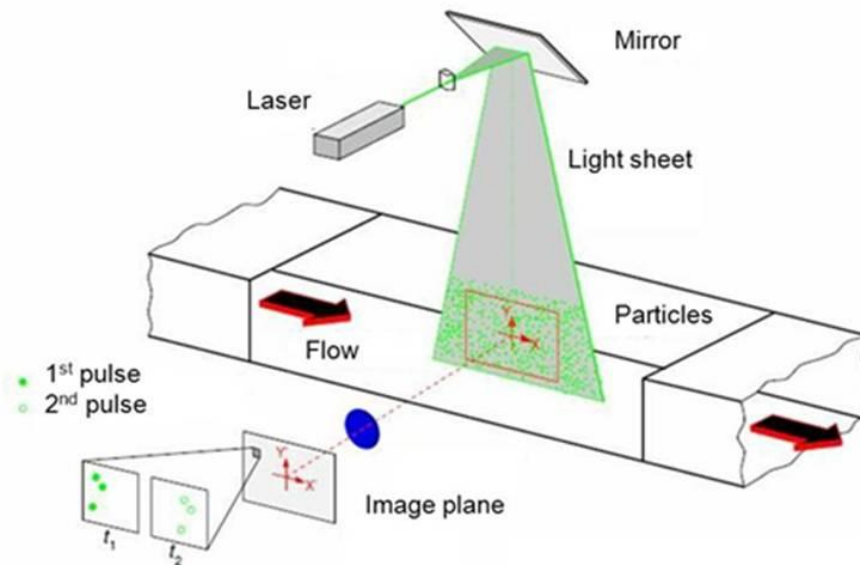


Figure 4.1: PIV working principle (Raffel et al., 2007)

### 4.2. PIV in Turbomachinery

In this research endoscopic PIV is applied in combination with a pneumatic measurement technique for investigation of diffuser flow conditions. The PIV technique has been developed for about 25 years. PIV has been used in turbomachinery tests: the work of Alhaj and Seume (2010), for example, showed a successful implementation of the PIV to a linear turbine blade cascade.

An extensive overview on the recent PIV applications in turbomachines was provided by Woisetschlager and Gottlich (2008), with a focus on rotating turbine and compressor test rigs and the developments within the PivNet network: “In recent research PIV was applied from high-speed flows in a blade cascade like by Stieger et al. (2004) up to rotating flows in transonic turbine and axial and centrifugal compressor test rigs, Gottlich et al. (2008), Bryanston-Cross et al. (2000), Estevadeordal et al. (2002), Ibaraki et al. (2007), Voges et al.



(2007), Hayami et al. (2004). Wernet et al. (2005) applied stereoscopic PIV to record the tip clearance flow in a low-speed four-stage axial compressor.” Woisetschläger and Göttlich refer to investigations on high-speed rotating turbomachinery flows proving that PIV has become a powerful measuring tool in the past decade. The resolution of measurement (size of interrogation area) for high-speed measurements and difficult optical access are mentioned as the major challenges for PIV sets in experiments of turbomachines. The highly curved windows which are used in almost every experiment introduce perspective viewing, distorting the images and then the measured velocity field. An important point is also that the high-speed PIV is mainly seen to be necessary in order to speed up the measurements while recordings sorted by the phase of the rotor are sufficient for investigation of rotor-stator interactions.

Göttlich et al. (2006) present results of PIV measurements on a transonic turbine operating at 10600 rpm at Graz University of Technology, Austria which enabled the investigation of the interaction between shocks, shock reflections, vortex shedding, and wake-wake interaction in those turbulent and transonic flows.

Voges et al. (2007) applied phase-resolved PIV in a centrifugal compressor with a vaned diffuser and impeller rotating at speeds up to 50,000 rpm. In the measurements, 180 PIV recordings were averaged for each of 16 phase angles. Structures in the velocity could be identified in the transient diffuser passage flow while the impeller passed by.

Voges et al. (2007) implemented PIV for investigation of the blade tip interaction with casing treatment on a single-stage transonic axial compressor, using a quartz glass window with curvatures matching the casing for the camera view and the periscope light sheet probes which allowed measuring at three different radial positions in the rotor passage and giving a general characterization of the investigated flow field based on the phase-averaged velocity vector maps. The results of Voges show the influence of the casing treatment design on the rotor passage flow, interacting phenomena as well as shock configurations of the flow field, for both peak efficiency and near stall operating conditions.

Presenting the history of the PIV, Kompenhans (2009) gives the year 1995 as a major breakthrough in the development of PIV, when it came out of the laboratory and came into use at research organizations in industry, followed by use of digital video cameras allowing capturing the two frames of a PIV recording within a short time interval and with full spatial resolution, and the necessary cross-correlation evaluation algorithms.

Roosenboom (2009) used PIV to study the propeller flow, combining CFD and PIV to investigate structures which dominate propeller flow, outlining velocity-derived quantities (vorticity, instantaneous fluctuations, velocity fluctuations, turbulence kinetic energy, Reynolds stresses) to be suitable for comparison and with characterisation of the capabilities of computational methods with respect to turbulence properties. Roosenboom found that the difference between PIV and CFD in the vortex structure organization of the blade wakes and in the wing boundary layer with slipstream interaction was due to strong dissipative terms in the uRANS models.



An alternative way to time-resolved PIV, based on a sufficient number of images taken, is applied by Badreddine (2009) who used the PIV technique together with hot-wire anemometry to study the flow with parameters  $Re=120$  and  $St=0.18$ , sorting out the PIV images related to the vortex shedding in this flow, determining the time period, and providing phase-resolved PIV data.

Reynolds, Gorrel and Estevadeordal (2010) used PIV to investigate wake-shock interactions for two stator loadings and three stator-rotor axial gaps of gas turbine engine fans and compressors. The study focuses on identifying and describing flow downstream of the deswirlers as a function of vortex strength, size, and location. This research shows that stator loading as well as axial gap have a significant effect on the strength and size of vortices shed due to transonic blade-row interactions. Different spacings generate interactions at different rotor bow-shock strengths.

The present PIV approach stands out due to the implementation in a “rotating” test rig (though there have been tests on rotating machines described by Woisetschlaeger (2008) in combination with the use of endoscopes for both laser and camera and thus no need of windows matched to the test rig’s surfaces.

### 4.3. PIV measuring system and requirements

The measuring system shown in Fig. 4.2 consists of two Nd:YAG lasers, optics which transform the laser beams into thin laser sheets, two cooling boxes, a synchronizer which controls signals of cameras, q-switches and laser sources when measuring, and a personal computer with software for evaluation of the acquired images. In laboratories, PIV systems are usually either adapted to a particular task like a test rig or an experimental setup for aerodynamic research, or used in rotation between different tasks. The second practice requires a flexible system design with a mobile foundation and high qualification of operating personal due to adjustments needed before every use on a new application.

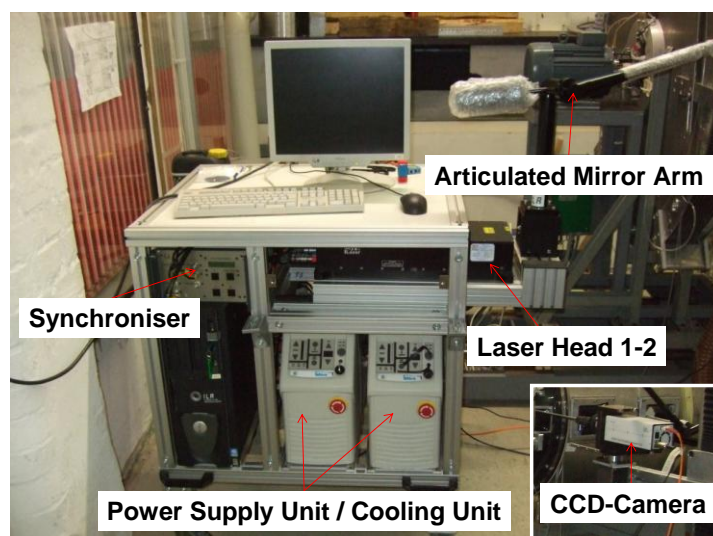


Figure 4.2: PIV measuring system

Vegetable oil particles which are brought into the flow upstream of the swirl generator by a perforated tube to ensure a homogeneous distribution are used for the seeding. The average size of the particles is 7  $\mu\text{m}$ .

Two Nd:YAG-lasers which operate in a pulsed mode generate light at the wavelength of 532 nm and a pulse energy of 200 mJ per laser head. A synchronizer coordinates the lasers and camera, with respect to a trigger signal.

The pulse distance in the tests is between 7 and 20  $\mu\text{s}$ , which corresponds to a particle displacement of about 0.3 mm for a 50 m/s flow velocity.

Working with the PIV measurement system synchronizer, adjustments must be made to define the sequence of measurements. Laser devices like laser lamps, q-switches as well as a camera and an external trigger are connected to the synchronizer which controls their operation. The timing for the PIV measurement is adjusted using this synchronizer.

The repetition rate of the measurement equipment is not higher than 10 Hz, i.e. 10 pairs of images per second. Depending on the application, a choice must be made between an internal or external trigger. An internal trigger coordinates image sequence with adjustable frequency up to 10 Hz. Due to this relatively low frequency, information produced using this mode can be used either for visualising high-scaled unsteady structures in the flow, like big vortices in the Karman vortex street behind blades, or for averaging of velocity field and measuring of velocity deviations. To investigate the unsteady wakes behind particular blades, an external trigger can be used, providing measurements in delay mode with respect to the rotor position.

According to the ILA PIV Hardware manual (2006) when the optional external trigger is switched on, the synchronizer will not send any output sequence and no camera output until a trigger input is there. While measuring in rotating machines, the trigger input can be referred to the rotor position. A piece of reflecting paper is put on the rotor between the test rig and the electric motor. The laser beam producing the external trigger is directed to the reference point. With a rotating shaft, every time the point reflects the laser light back to the trigger, a signal is sent to the synchronizer.

Moreover, according to ILA, there is an option to toggle the trigger modus between angle and delay modus. In the angle modus, a phase angle can be added to every trigger input signal which is suitable when measuring on rotating machines. In the delay modus, the delay time will be added to every trigger input to delay the measuring. The trigger phase is a special delay time which can be added to every starting time of measuring. Using the phase triggering mode in the present research, wakes produced by the blades can be captured with respect to a particular angular rotor position.

The laser light reflection from NACA-blades and the internal diffuser and hub surfaces was reduced by painting them black. However, in some tests reflections affected the image quality and the correlations particularly in the boundary layer and between the blades.

#### 4.4. Endoscopic PIV

To study the velocity distributions in the turbomachine's geometries, a configuration of the laser light-section and the camera view must be chosen to be either an application of an endoscope or non-endoscope setup (using transparent windows instead of endoscopes). In the latter case the laser beam, after being generated by the laser heads, is guided through a system of lenses instead of going through the window to illuminate the measurement plane. In Endoscopic PIV, the laser light beam is guided through an endoscope (Fig. 4.3) into the test rig. There are three types of endoscopes, which guide the thin light sheet either straight ahead, or turn it 90° in two possible directions.

The endoscopes for cameras have a similar design and are shown in Fig. 4.4. Therefore a wide range of geometric configurations can be employed for PIV measurements. In the camera endoscope, the image is guided from the optical entry through a lens system to the ocular lens. The laser endoscope consists of an adapter, which is used to connect it to the light sheet arm, and a metal sleeve, which has a prism on its end. The conversion of the laser beam to a light sheet and, if necessary, its redirection occurs in the prism. The light sheet is about 0.5 mm thick and has a length of more than 2000 mm.

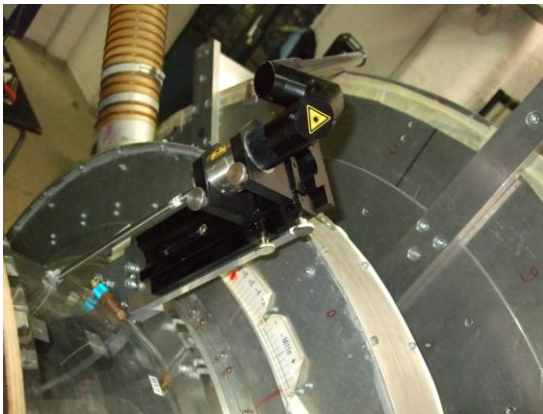


Figure 4.3: Laser endoscope in diffuser test rig



Figure 4.4: Camera endoscope

According to Mohseni and Seume (2011), image distortion is a common issue in many PIV measurements. Geometric image distortion is due to the lenses used in the optical components of the PIV system. Mohseni and Seume state that with a non-endoscopic setup and when the camera view axis is normal to the object plane, which is so for the two-dimensional PIV, the image distortion may be neglected. The use of endoscopes, which introduce additional lenses to the optical path causes additional distortion in the image which cannot be neglected in the corners of the image. The other case where image distortion cannot be neglected is stereoscopic PIV, where the cameras' optical axes are not perpendicular to the object plane. In the present 2D PIV setup the camera view is set perpendicular to the measurement area.

Work of Mohseni (2010) and the present PIV investigation both showed that the position of the laser arm significantly influences the quality of the light-sheet due to laser reflections in the arm. Improvement of this factor is not provided in this research but left for future investigations. In the present research, all mentioned sources of errors result in accuracy of

PIV measurement not lower than what is given in Fig. 5.4. The task of providing homogeneous and sufficient seeding is challenging in all PIV measurements, and especially in the present research, where the medium comes into the test rig directly from the working hall. Particles were added to the inlet flow using a perforated tube located in front of the test rig inlet (upstream of the swirl generator). Improvements of the measurement accuracy through future seeding solutions and the perfection of laser arm positioning or the elimination of the laser arm must be done in future investigations.

## 5. Measuring programme

### 5.1. Measuring programme

Experimental investigations are conducted using the diffuser test rig at TFD and the measuring techniques 2D PIV, LDA, tabs and probes. Fig. 5.1 shows the measurement setup in one of the main views on the diffuser test rig. At the inlet of the annular diffuser, the radial distribution of the total and static pressure as well as the swirl angle is measured using three-hole pneumatic probes. For measuring of static pressure, 128 taps are installed in the annular and the conical diffuser and connected with an automated Pressure Systems Net Scanner. The annular diffuser taps are located on the shroud and on the hub. The conical diffuser has taps on the shroud and on a narrow tube located along the diffuser centre line for housing the pressure channels.

PIV measuring planes are shown in Fig. 5.2 on the measuring setup in the second main view on the test rig. The three planes correspond to three configurations of the laser sheet and camera positions to acquire planar velocity fields in the inlet part of the diffuser, close to the bladed wheel. Details to the measurement planes are given in paragraphs 7.1 – 7.3.

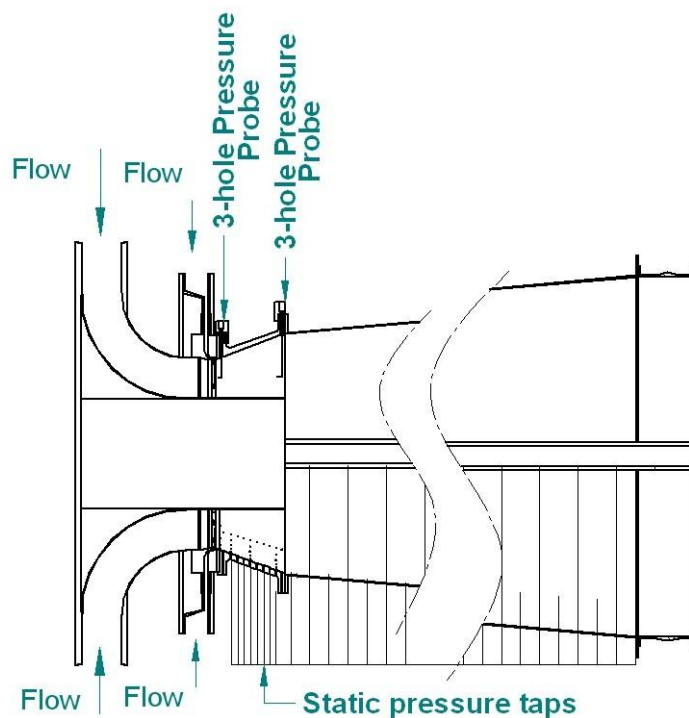


Figure 5.1: Measurement setup, view 1

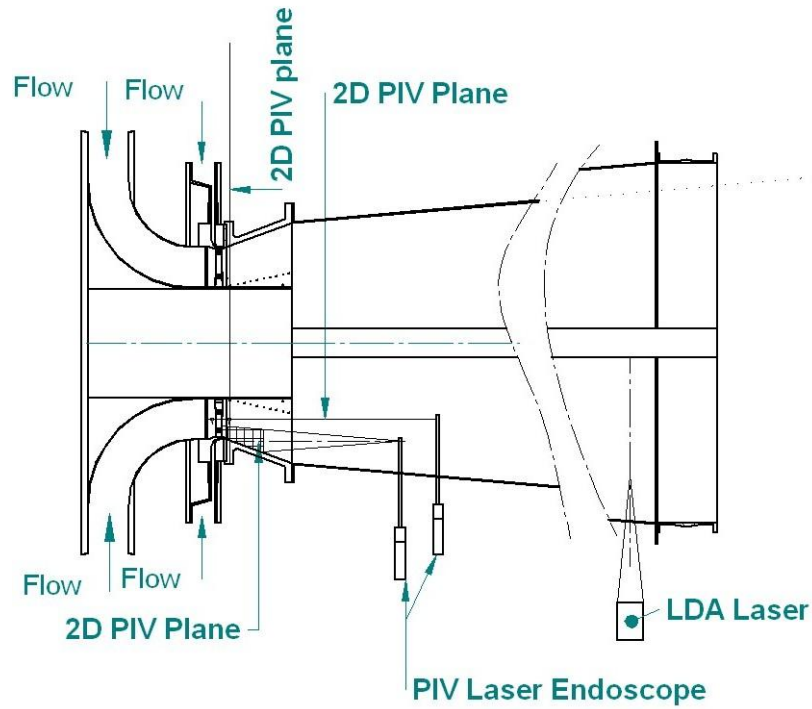


Figure 5.2: Measurement setup, view 2

The inlet swirl is oriented in the negative and positive direction for turbine operating conditions of partial load and overload, respectively. The  $0^\circ$  swirl refers to the diffuser design point. The direction of swirl angle used is shown in Fig. 5.3. During the tests, the swirl angle was adjusted at the turbine base load according to the flow angle measured behind the midspan of the bladed wheel.

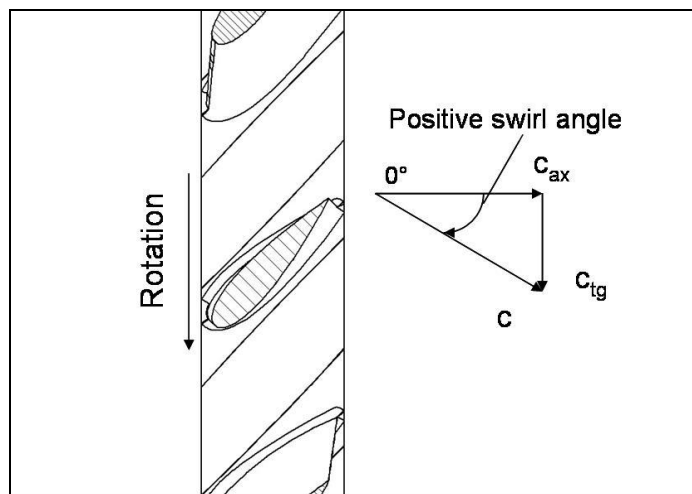


Figure 5.3: Velocity definition behind NACA-bladed wheel

An important parameter describing the flow structure is the flow coefficient which depends on the axial velocity and the rotational speed of the rotor, and refers to the turbine stage. This parameter is used as well in the research of Sieker and Seume (2008) and Chernikov (2009) and is defined for every operating point as the ratio between the mean axial velocity at the inlet with respect to the circumferential velocity at the Eulerian radius:

$$\Phi = \frac{\bar{c}_{ax}}{u_{Euler}} = \frac{\frac{\dot{m}}{\rho \cdot A_1}}{2 \cdot \pi \cdot n \cdot r_{Euler}} \quad (14)$$

The Mach number, which shows compressibility effects in the flow, was varied in a small range of 0.1 to 0.16. Therefore the flow is assumed to be incompressible. Reynolds number, based on the channel height in the annular diffuser inlet, is about  $4 \cdot 10^5$ , and, based on the hydraulic diameter, is about  $5 \cdot 10^5$ . Mass flow is calculated by averaging the radial distribution of the axial velocity over the channel height.

In the analysis of PIV data vorticity is used. According to the Springer Handbook of Experimental Fluid Dynamics, (2003), “vorticity characterizes the rotation rate of a fluid particle. In the case of constant-density incompressible flows, vorticity is acquired by a pressure gradient introduced at a physical surface. In turbulent flows vorticity is a key to improving understanding of the mechanisms that control the motion of the large-scale structures.” The vorticity is defined in the Cartesian coordinate system as

$$\omega_z = \left( \frac{\partial c_{tg}}{\partial x} - \frac{\partial c_{ax}}{\partial y} \right) \quad (15)$$

For calculation of the turbulence intensity, the following correlations are applied as by PivTEC (2006):

$$\bar{x} = \frac{1}{N} \sum_{i=1}^N x_i \quad (16)$$

Mean value

$$\sigma_x^2 = \frac{N \sum_{i=1}^N x_i^2 - \left( \sum_{i=1}^N x_i \right)^2}{N(N-1)} \quad (17)$$

Variance

Standard velocity deviation,  $c'$ , is defined as the square root of the variance. To study turbulent characteristics, the mean velocity components,  $(\bar{c}_{ax}, \bar{c}_{tg})$  and the rms velocities  $(c'_{ax}, c'_{tg})$ , are used. The turbulent kinetic energy is defined as

$$k_{kin,turb,3D} = \frac{1}{2} (\overline{c'_{ax}{}^2} + \overline{c'_{tg}{}^2} + \overline{c'_r{}^2}) \quad (18)$$

As the two-dimensional PIV is applied, the radial component cannot be measured simultaneously with the axial and tangential component. Therefore the radial component is not considered and the following formula is used:

$$k_{kin,turb,2D} = \frac{3}{4} (\overline{c'_{ax}{}^2} + \overline{c'_{tg}{}^2}) \quad (19)$$

In order to set realistic conditions, the mass flow rate and swirl in the leakage flow were set using the approach given by Fleige (2002). In the tests with swirled tip leakage flow, the velocity ratio between the leakage flow and the main flow was the highest at approximately

1.2. The direction of swirl in the leakage flow is adjusted using the relation from Fleige (2002) for turbine outlet flows:

$$\alpha_{\text{leakage}} \approx 0.25 \cdot \alpha_{\text{main\_flow}} - 19^\circ \quad (20)$$

## 5.2. PIV Technique Validation

Validation of the PIV technique is provided through direct comparison of PIV measured velocities to velocities measured with pneumatic probes. At the inlet of the annular diffuser, the radial distribution of total and static pressure as well as the swirl angle was measured by Sieker and Seume (2008) using 3-hole pneumatic probes. The velocity is calculated from the pneumatic probes measured data. The PIV measurement positions used in the present research intersect the pneumatic probes' measurement positions used by Sieker and Seume (2008) in one line in the annular diffuser inlet.

Figure 5.4 shows velocity distributions measured at the inlet of the annular diffuser. The uncertainties of probe measurements are too small to be shown in Fig. 5.4. The PIV results do not cover the whole channel due to the limited opening angle of the light section. Axial velocities are compared for the annular diffuser channel radius. In the middle of the measured region, the pressure probe measurement is covered by the 95% confidence interval of the PIV measurement thus showing that the agreement is within the accuracy of the PIV measurement. This uncertainty increases towards the edges of the illuminated region because the contrast of the particles is lower, and the background noise level consequently is higher at the edges of the PIV image than in the middle.

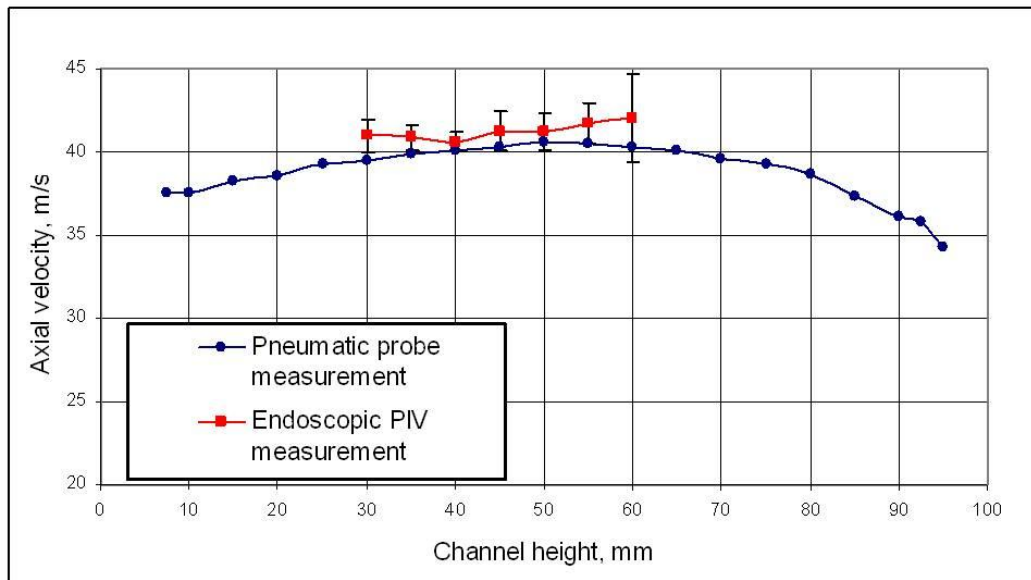


Figure 5.4: Comparison of PIV and pneumatic probes at the annular diffuser inlet



## 6. Diffuser Flow Features (acquired by PIV) and their impact on diffuser performance

The interaction between the diffuser's boundary layer and the effects introduced by the bladed wheel is studied applying PIV. The flow structure and unsteady effects appearing due to a change in the bladed wheel operating conditions are found to be responsible for change of the diffuser's performance. The PIV method was used which allows planar velocity measurements of two- or three-component velocity fields. In the present research, a two-component PIV using a fully endoscopic approach is applied to the diffuser test rig.

In order to describe the flow phenomena in the diffuser which could not be explained with conventional measurement techniques, the present PIV investigation is performed for the operating points which simulate real turbine operating conditions. A part of these operating points were first studied by Sieker and Seume (2008). Other operating points were applied for the first time. Firstly, investigations in two configurations are discussed, which are focused on visualisation of the boundary layer on the diffuser's shroud. Further, PIV was applied in a 3<sup>rd</sup> configuration to study additional operating points in order to better investigate the blade wake in the core flow. Data of all three configurations provide information on the three-component velocity field in the front part of the annular diffuser and are used to explain the diffuser performance change depending on the rotor load.

In the three-dimensional diffuser flow, three velocity components need to be measured. These are the axial velocity  $c_{ax}$ , the tangential velocity  $c_{tg}$ , and the radial velocity  $c_r$ .

PIV provides information on:

- 1) time-resolved velocity fields (with measuring frequency limited to 10 Hz),
- 2) time-averaged velocity fields,
- 3) RMS-velocities in the flow,
- 4) Turbulent structures in the flow.

In the diffuser test rig, the following structures are studied:

- Blade wakes separated from the blades of the 1-stage rotor
- Vortices which originate due to the interaction between the bladed wheel and the endwall
- Vortices which originate due to flow separation from the blade surface in the endwall region due to angles of attack at the leading edge of the blades in the off-design points

## 6.1. Diffuser Boundary Layer Investigation

For a better understanding of the flow field behind the bladed rotor, PIV measurements are performed for diffuser tests of Sieker and Seume (2008), focusing on the inlet part of the annular diffuser. The operating points are given in Table 4. These testing conditions had been chosen by Sieker and Seume (2008) to represent different turbine operating conditions: design point, partial load, and overload. At the partial load point, the bladed wheel is working as a compressor sucking air into the test rig, additionally to the fan, representing turbine rotor partial load working conditions. At the overload point, the bladed wheel is working as a turbine receiving power from the flow, representing the turbine rotor working at overload. The rotational speed of the bladed wheel is varied from 1500 to 2500 rpm. The variation of rotational speed and mass flow allows adjusting the flow coefficient:

**Table 4. Operating points for configurations 1 and 2**

	rotational speed	mass flow	Flow coefficient
Name	n, rpm	kg/s	$\phi$
Design point	2500	5.6	0.78
Partial load	2500	4.91	0.68
Overload	1500	5.56	1.29

PIV is employed in configuration 1 which is shown in Fig. 6.1. This configuration allows studying the flow field in the axial and radial directions. A fragment of the configuration showing the measurement plane is shown in Fig. 6.2. A section of the diffuser channel which is 101 mm high and located immediately behind the spoke wheel is illuminated by the laser. Due to the opening angle of the light sheet, and for maximizing the measurement region, the distance between the laser source (endoscope outlet) and the camera endoscope position was set to 100 mm. Endoscopes can be moved radially to come closer to the case or to the hub, respectively. The camera endoscope uses the same insert in the diffuser as the pneumatic probe in a comparison measurement. The distance between the measurement plane and the camera endoscope is 50 mm (half of the channel height at the inlet of annular diffuser). This distance results in high-quality correlations of the PIV at a measuring section of 70 mm x 100 mm which is considerably large.

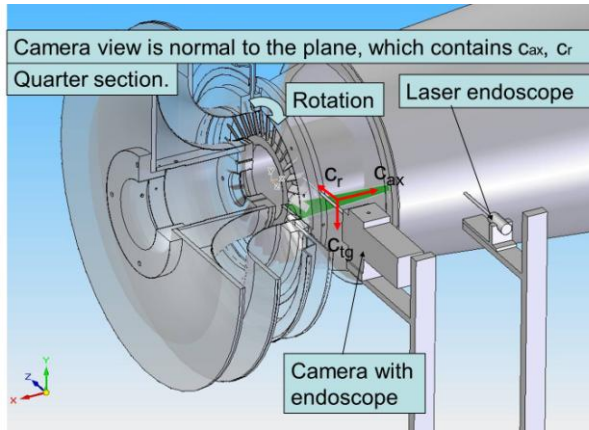


Figure 6.1: PIV configuration 1

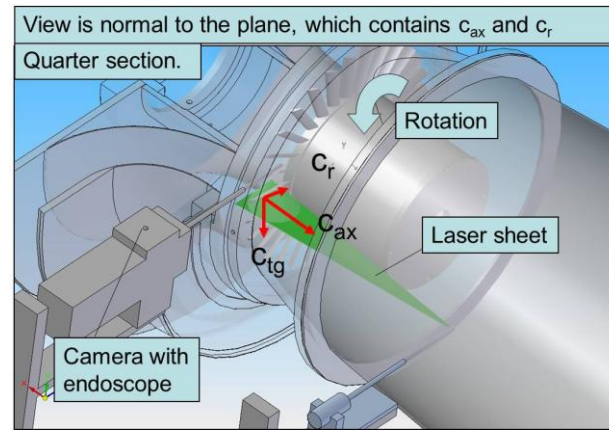


Figure 6.2: PIV configuration 1, fragment

The data of pneumatic measurements of Sieker and Seume (2008) is analysed together with new data acquired with PIV. Important factors are the steady flow structure, distribution of turbulence in the flow and, particularly, unsteady structures. Sieker and Seume (2008) measured velocity distributions using 3-hole pneumatic probes in the inlet of the annular diffuser and velocity distributions and turbulence intensity using LDA in the position at 50% of the annular diffuser length. Figure 6.6 shows that their measurements with probes in the inlet are covered by the PIV measurements. However, the PIV measurement region covers only 36% of the annular diffuser length. Therefore only tendency can be considered to compare the PIV and LDA results downstream of the inlet.

Velocity distributions for all three operating points of Table 5 taken with a pneumatic probe and with PIV in the inlet of annular diffuser are shown in Fig. 6.3. Inlet velocity profiles are very uniform but the boundary layer is strongly developed especially for the partial load operating point. Tangential velocity distributions in Fig. 6.4 show a small, but radially uniform swirl at this point, while swirl at the design point is changing direction along the channel height. Velocity distributions taken with LDA at 50% of annular diffuser's length are shown in Fig. 6.5. The boundary layer has separated for the partial load point, but not for the design points. A uniform velocity profile is measured for the overload point.

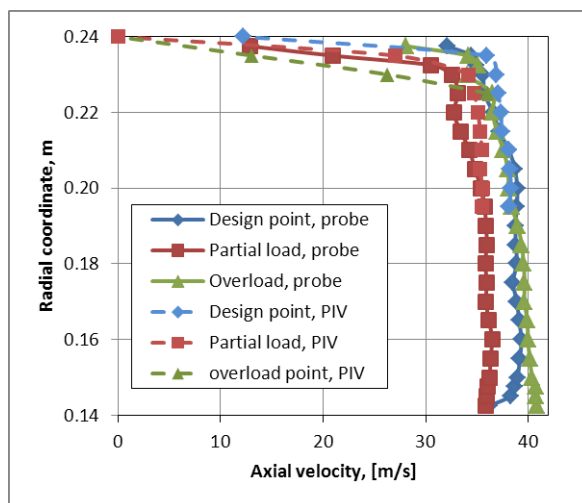


Figure 6.3: Velocity at diffuser inlet, Sieker and Seume (2008) and PIV

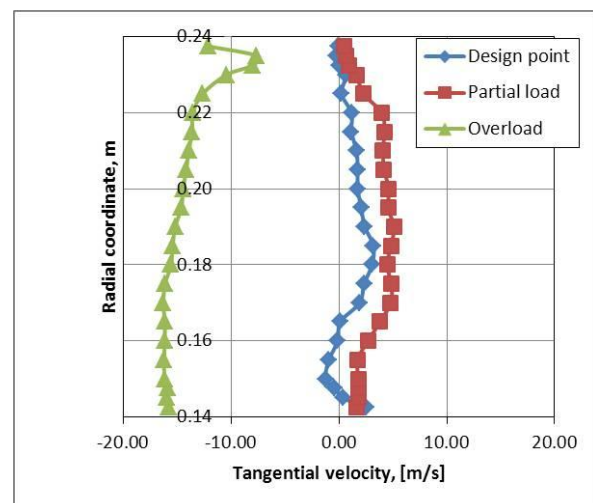


Figure 6.4: Velocity at diffuser inlet, Sieker and Seume (2008)

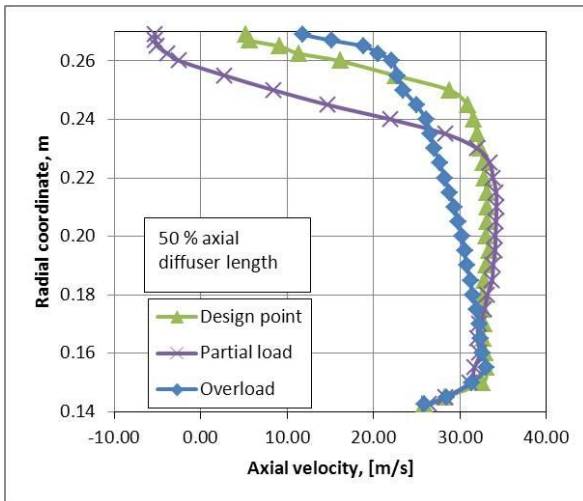


Figure 6.5: Velocity at 50% diffuser length, Sieker and Seume (2008)

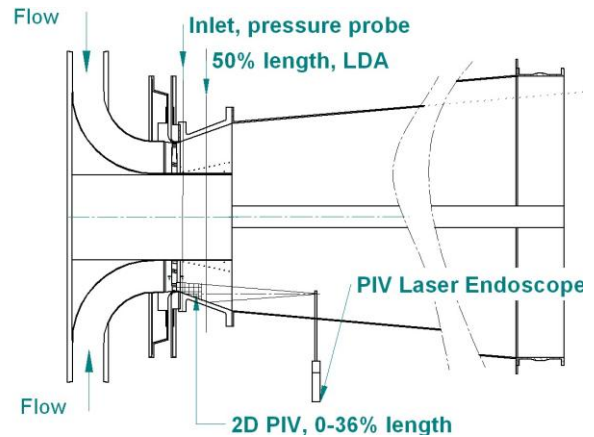


Figure 6.6: Comparison of measurements

Further, averaged velocity fields measured with PIV for three operating points of Table 5 provide information on a planar structure of the flow. A velocity field for the design point is shown in Fig. 6.7. Two of 30 profiled blades are shown in the left part of the figure. The boundary layer on the diffuser shroud is thin. For the partial load point shown in Fig. 6.8, it is thicker and is growing downstream. Matching the probe measurements of Sieker and Seume (2008), PIV data show that the velocity reduction in the wall region is stronger for the partial load point. The flow reattachment is found at about 30% of the diffuser length. Velocity field shows that effective diffuser cross-sectional flow area is bigger for the design point. Streamlines show that for the design point, the flow is following the diffuser shroud while for the partial load point a back flow zone is provided from a dimensionless diffuser length of 0.3. Flow structure for the overload point, which is shown in Fig. 6.9, is characterized by a highly turbulent boundary layer. The streamlines, however, follow the diffuser geometry. No coherent separation zone is observed.

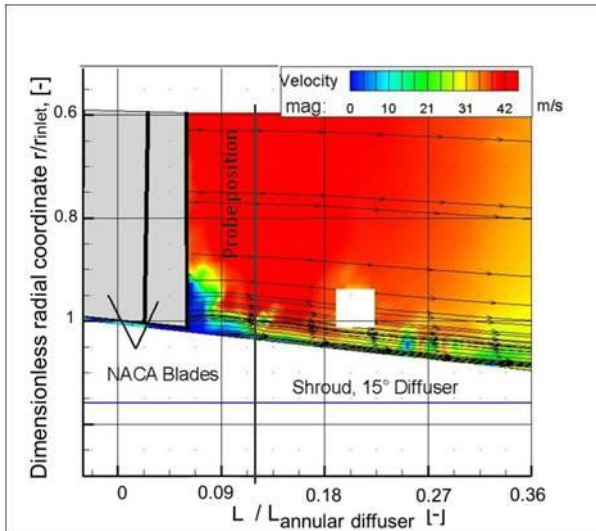


Figure 6.7: Averaged velocity field, design point

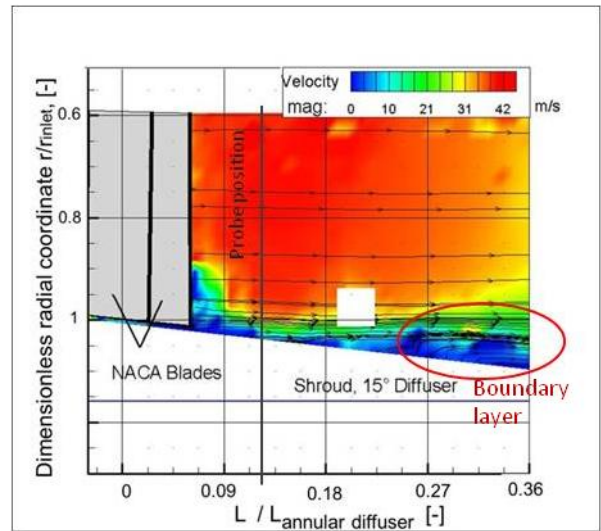


Figure 6.8: Averaged velocity field, partial load

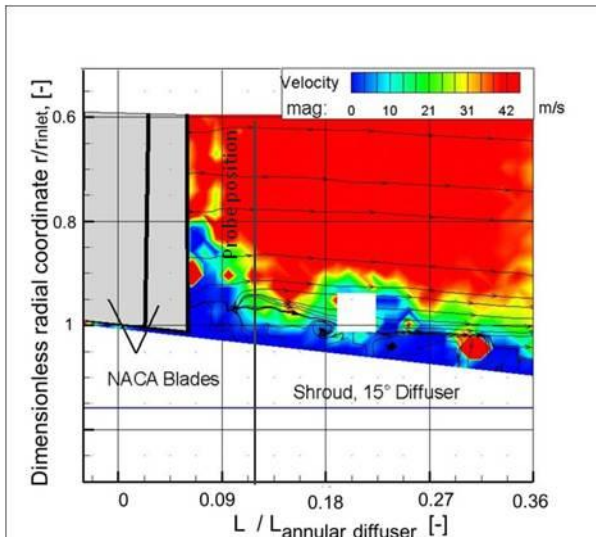


Figure 6.9: Averaged velocity field, overload

The measurements of rms-velocities are needed to understand distributions of the turbulence level in the flow. The measurements of Sieker and Seume (2008) shown in Fig. 6.10 give axial rms-velocity distributions taken with LDA at a position 50% of the annular diffuser's length. Figure 6.11 gives distribution of tangential velocity. Figures 6.12 and 6.13 give the RMS-velocity flow field for the design point and partial load point measured with PIV. From the rms velocity field it can be seen, that the PIV measurement hint at the increase of turbulent kinetic energy at the position at 50% of the annular diffuser length, comparing to the operating points found by Sieker and Seume (2008). A zone with increased turbulence is developing at the outer part of the blade passage. For the design point, the zone of high turbulence is thicker in the diffuser inlet but its thickness is decreasing rapidly and the velocity fluctuation drops to 0-5 m/s in the axial middle of the diffuser. For the partial load point, it is less developed in the diffuser inlet but then is growing downstream, occupying

about 20% of the channel height. The rms-velocities for the overload point (Fig. 6.14) are measured by PIV approximately two times higher than at the design point. The profile is uniform. The core flow is found to be highly turbulent.

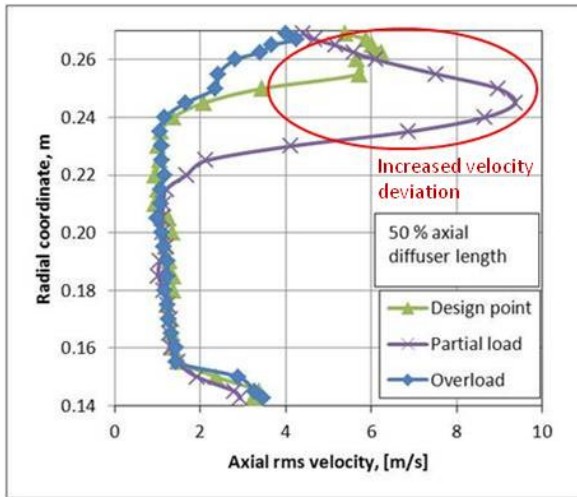


Figure 6.10: Axial RMS velocity, Sieker and Seume (2008)

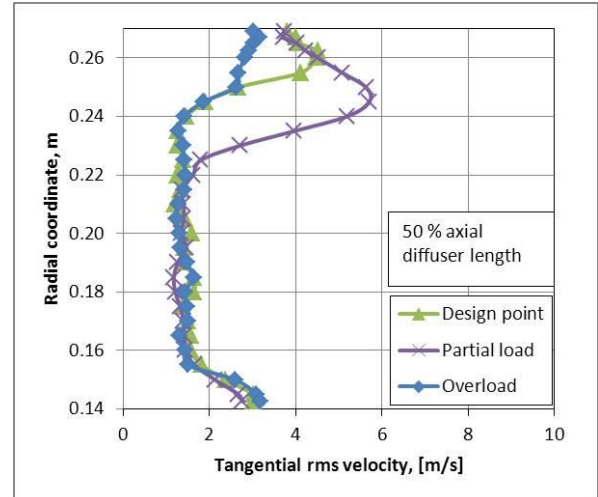


Figure 6.11: Tangential RMS velocity, Sieker and Seume (2008)

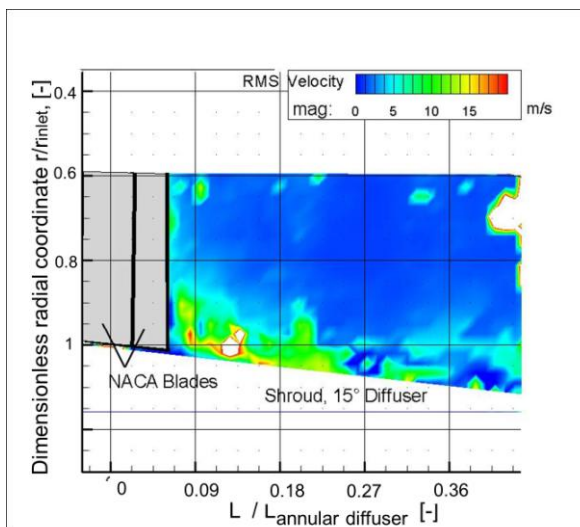


Figure 6.12: RMS velocity field, design point

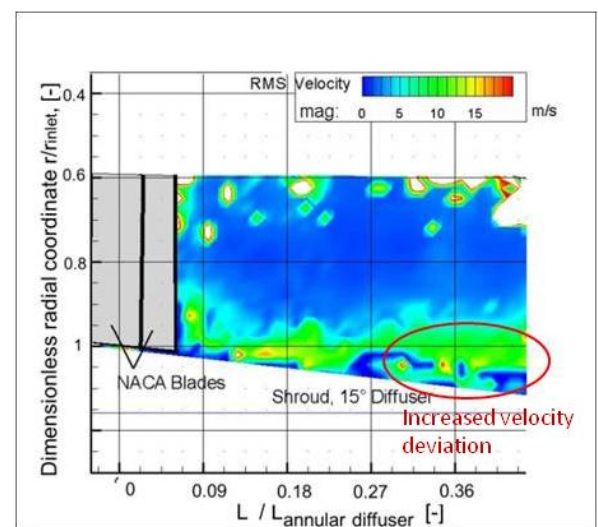
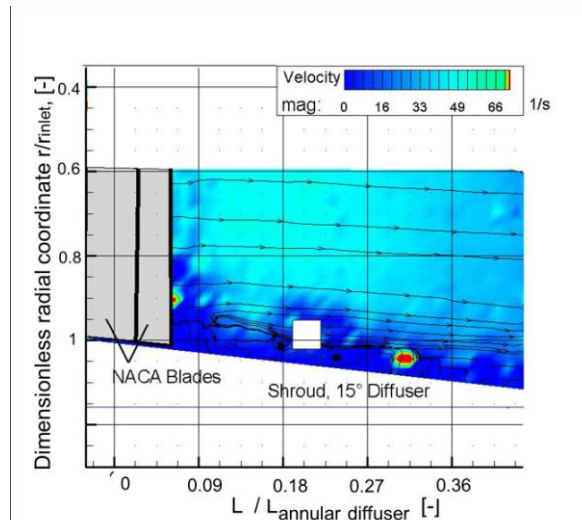


Figure 6.13: RMS velocity field, partial load





**Figure 6.14: RMS velocity field, overload**

The turbulence level can provide an explanation for changes in pressure recovery, but the following investigation is needed to understand the basics of the flow phenomena. PIV allows consideration of the averaged flow in terms of vorticity. Fig. 6.15 shows that for the design point, averaged vorticity is higher in the boundary layer. Comparing the vorticity fields for design and the partial load points (Fig. 6.15, 6.16), we notice that the vortex is three times longer at the partial load point than at the design point and the flow separates at 30% annular diffuser length. For the design point, the vortex ends approximately at 20% and only small vortices can be seen downstream of this point. PIV data for averaging are provided for a constant blade position; therefore, single vortices can be measured.

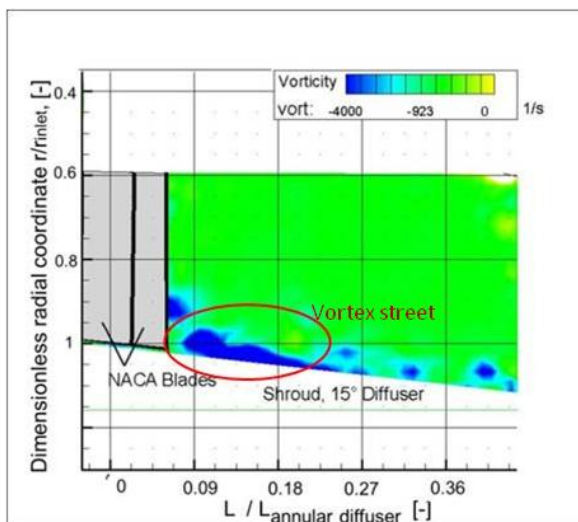


**Figure 6.15: Averaged vorticity field, design point**

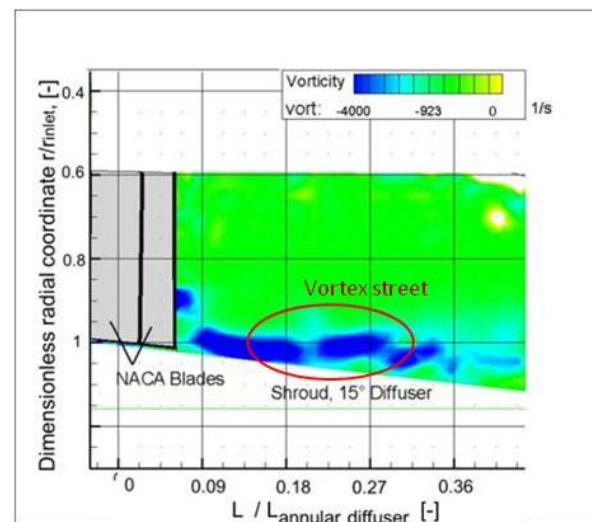


**Figure 6.16: Averaged vorticity field, partial load**

For the design point, the vortex street is very close to the casing. For the partial load point with negative swirl, the vortex street is close to the casing and is following the diffuser's casing until separation happens, where it follows a recirculation zone. Before a dimensionless length of 0.25, separation takes place occasionally downstream of that length, a back flow zone is established. For the overload point, Fig. 6.17, vortices are occupying almost 20% of the diffuser channel height.

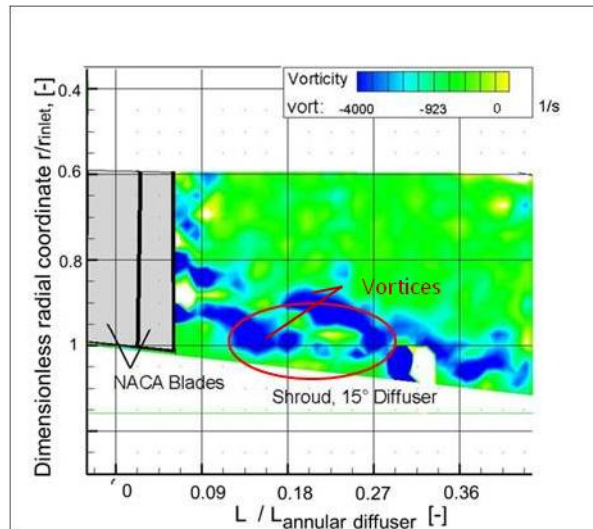


**Figure 6.17: Averaged vorticity field, overload**

For a better understanding of the flow parameters, parameters like vorticity (Fig. 6.18) and rms-velocity (Fig. 6.19) are extracted, at a radial position 100% of the diffuser inlet height. Vorticity in the negative vortex is almost two times stronger at the partial load and at the overload operating points than at the design point. This is causing higher values of the pulsation component in the boundary layer which are seen in the rms-velocity distributions in Fig. 6.13. For the design point, vorticity is around 0 behind the vortex in the inlet.

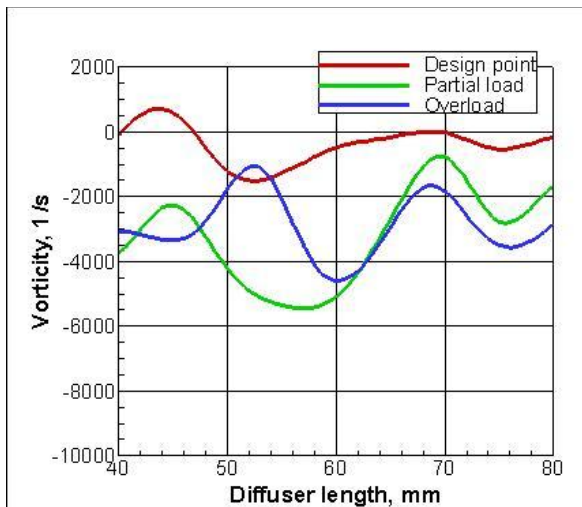


**Figure 6.18: Vorticity extracted from PIV data**

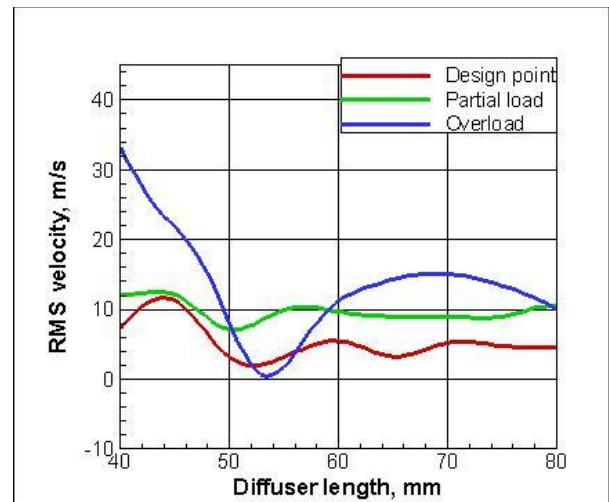


**Figure 6.19: RMS velocity extracted from PIV data**

To study the vortex distribution in the diffuser flow and to further understand the origin of this phenomenon, single (not averaged) PIV images are considered below. Fig. 6.20 shows a typical velocity field in terms of vorticity for the design point. Fig. 6.21 shows a moment where the blade wakes could be visualized in the flow in the form of couples of small counter-rotating vortices. Vortices are appearing at the trailing edge due to a difference in parameters on the pressure and on the suction side of the blade.



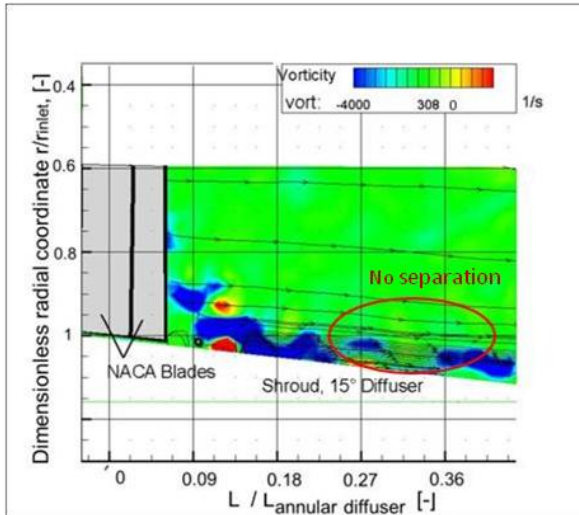


Figure 6.20: Single vorticity field 1, design point

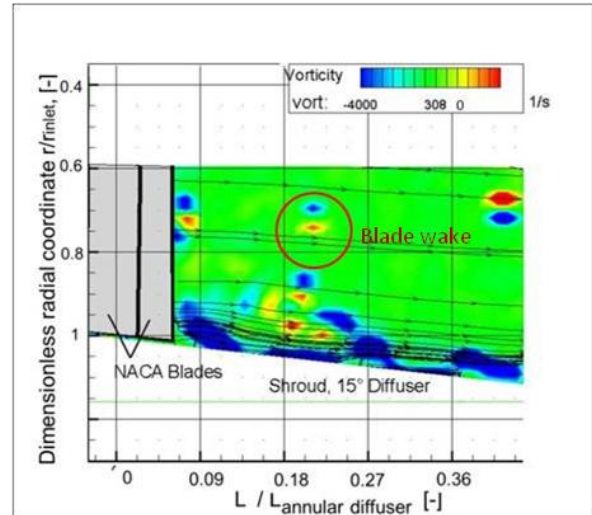


Figure 6.21: Single vorticity field 2, design point

For the partial load point (Fig. 6.22), blade wakes are more developed because it is an off-design operating point, where the angle of attack on the blades and the swirl angle have changed. Vortices originating due to flow separation from blade surfaces in the endwall region are coming further downstream, causing distortions of the velocity profile. The big vortex behind the blade's tip is much bigger and stronger than vortices in the blade wake in the core flow. For the partial load point, the vortex street, though having intensive vortices, is not sufficient to prevent separation. Figure 6.23 shows how the flow is deflected by a separation zone with a strong vortex in the middle of the separation zone.

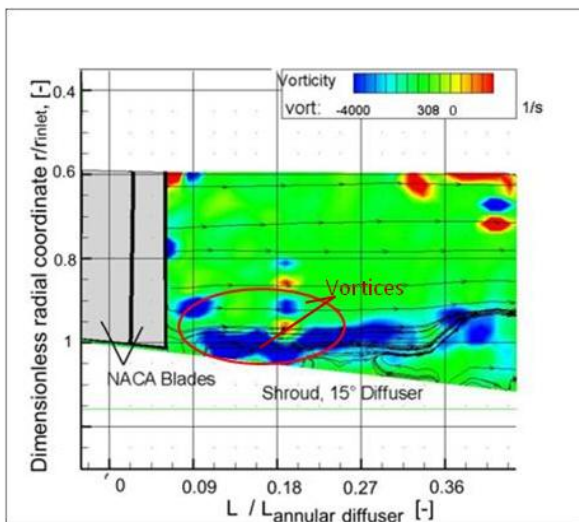


Figure 6.22: Single vorticity field 1, partial load

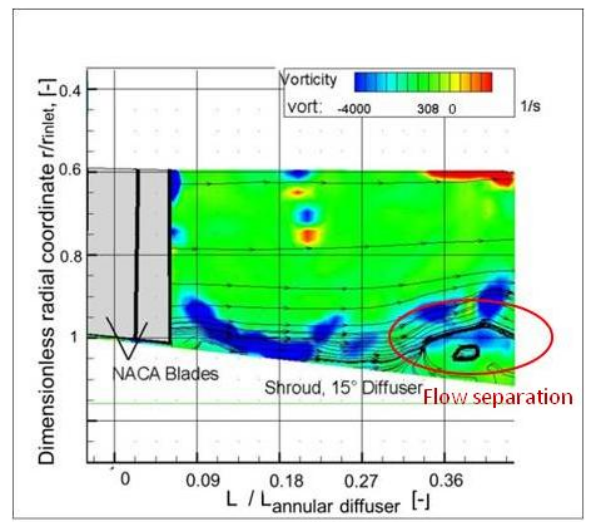
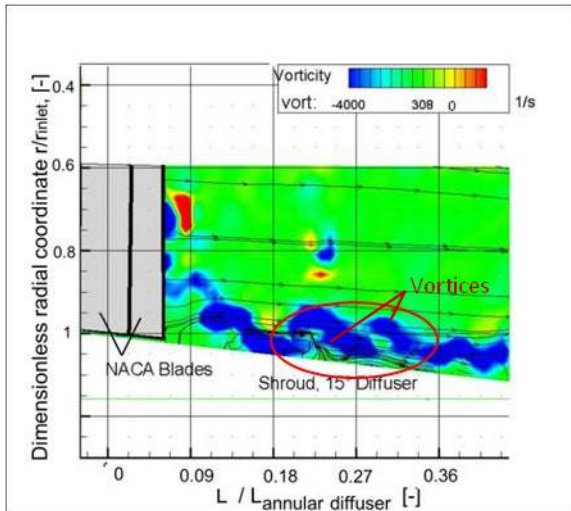
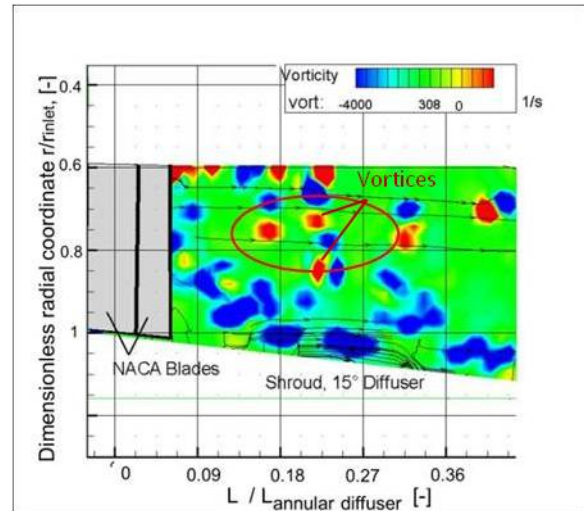


Figure 6.23: Single vorticity field 2, partial load

Figure 6.24 shows a non-averaged vorticity field for the overload point. No separation is detected. Vortices behind the blade's tip are strong and long-living. Stochastic structures occupy the boundary layer. In Fig. 6.25 unsteady structures can be found in the core flow, explaining the high turbulence level found in Fig. 6.14.



**Figure 6.24: Single vorticity field 1, overload**



**Figure 6.25: Single vorticity field 2, overload**

Using the 1<sup>st</sup> PIV configuration, the presence of a vortex at the shroud behind the blade tip has been detected. For the design point, the vortex is weak due to favourable flow conditions at the blades. For the off-design operating points, the vortex is bigger and is developed along the diffuser shroud. A full understanding of the influence of vortices which were discussed in this paragraph on the diffuser function requires the consideration of the vortex features in the circumferential direction provided in the subsequent section 6.2.

## 6.2. Diffuser Boundary Layer Investigation (2<sup>nd</sup> Configuration)

In order to investigate the development of the vortex responsible for the diffuser performance in the radial-circumferential direction, the same operating points as in paragraph 6.1 are studied applying a second PIV configuration. The second measurement configuration is shown in Fig. 6.26. A fragment of the configuration showing the measurement plane, which is a sector perpendicular to the diffuser longitudinal axis directly behind the rotating wheel, is shown in Fig. 6.27. This configuration allowed capturing the velocity distribution 15 mm downstream of the rotor. Tangential and radial velocity components are captured. The measuring area contains one third of the radial channel height at the casing.

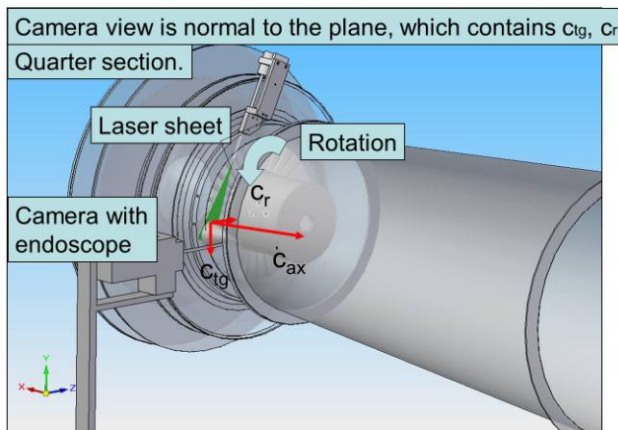


Figure 6.26: PIV configuration 2

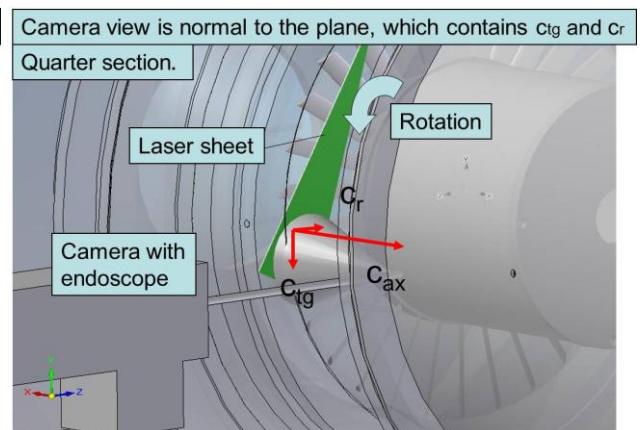
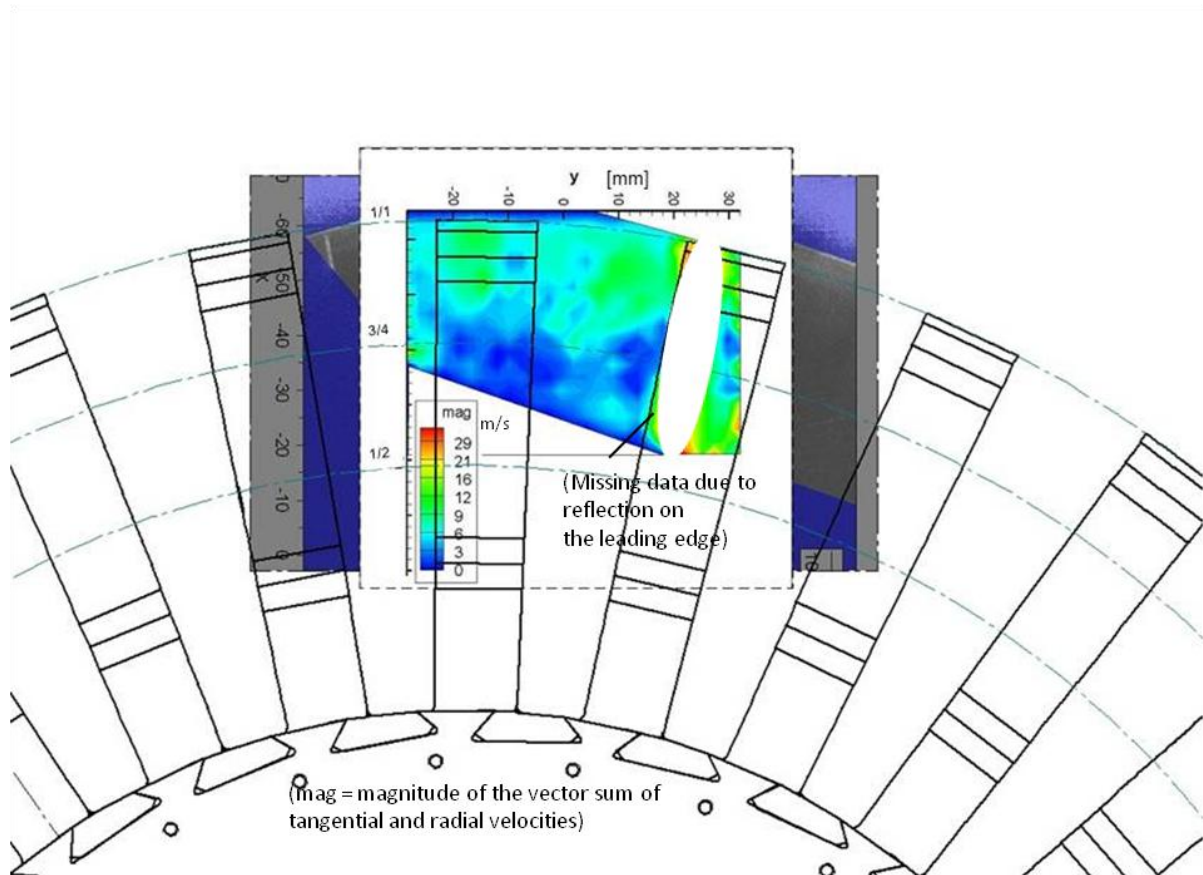


Figure 6.27: PIV configuration 2, fragment

At this point, the advantage of PIV as a planar measurement technique is used. The measuring time was shorter than it would have been if the same amount of data would have to be measured using point-based methods. It must be mentioned that errors caused by optical effects are higher in this configuration than in the others because the main velocity component is perpendicular to the measuring plane. This undesirable effect is reduced when swirling flows are studied.

The 2D velocity distribution behind the bladed wheel (in the inlet of the annular diffuser) is studied to visualize and investigate the inviscid core flow, secondary flows in the blade passage, blade wakes, and the vortex in the peripheral region behind the blade tips. In the analysis of the flow structure between the blades of the NACA wheel, tangential ( $c_{tg}$ ) and radial ( $c_r$ ) velocity components are considered.

For the design point shown in Fig. 6.28, the flow is supposed to leave the wheel without any additional swirl. The velocity magnitude is low in the measured section because the flow leaves the wheel almost without swirl, and the main component is perpendicular to the measuring plane. In the area behind the blade, tangential velocities are highly negative. An increase of the radial velocity in the direction of the casing hints at the expanding flow (good diffuser function). The symmetrical shape of the blades results at the design point results in the absence of separation from the blade (no vortices behind the blade tip are found).



**Figure 6.28: Distribution of the combined tangential / radial velocity field behind the wheel, design point**

The operating point shown in Fig. 6.29 represents conditions where the turbine rotor is working on the partial load. The tangential velocity is also highly negative behind the blade. The negative swirl is found to be moderate. A noticeable gradient of the radial velocity in the direction of the shroud is due to the downstream channel expansion. An increase of absolute velocity is also noticeable behind the blade.

As it will be shown below, an important phenomenon is the vortex found in the shroud region. While measurements with the first PIV configuration showed that it is long in the axial direction, this PIV configuration shows that it is also long in the circumferential direction. In the radial direction it takes only about 5% of the channel height. A secondary flow is observed with velocity growing towards the casing.

The operating point shown in Fig. 6.30 represents overload, in which case, in the present rig, the bladed wheel is working as a turbine receiving energy from the flow. As expected, a high tangential velocity opposite to the wheel's rotation direction is measured. The area behind the blade with negative swirl is reduced compared to the partial load point; the core flow region is definitely bigger than for other tests. A strong vortex is observed behind the blade tip. The velocity direction in the vortex is similar to that in the core flow.



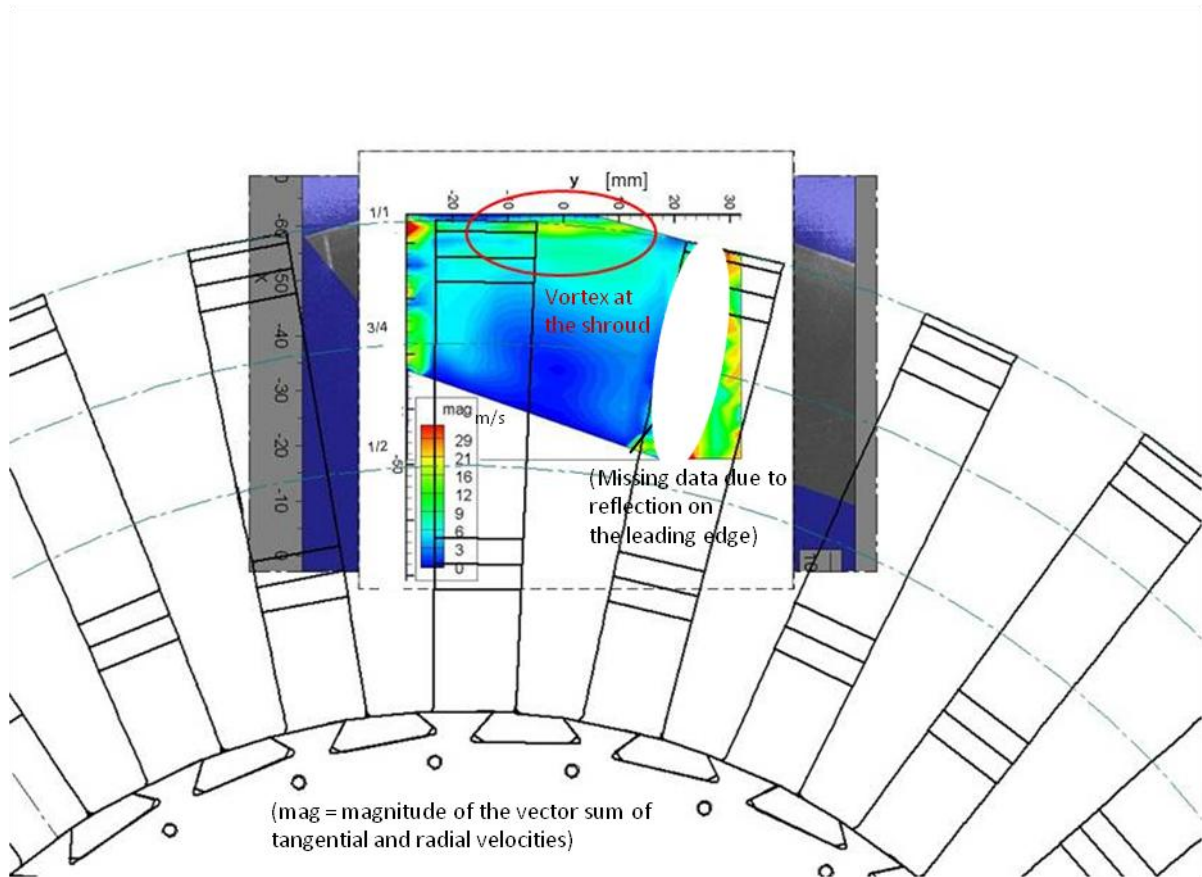


Figure 6.29: Distribution of the combined tangential / radial velocity field behind the wheel, partial load

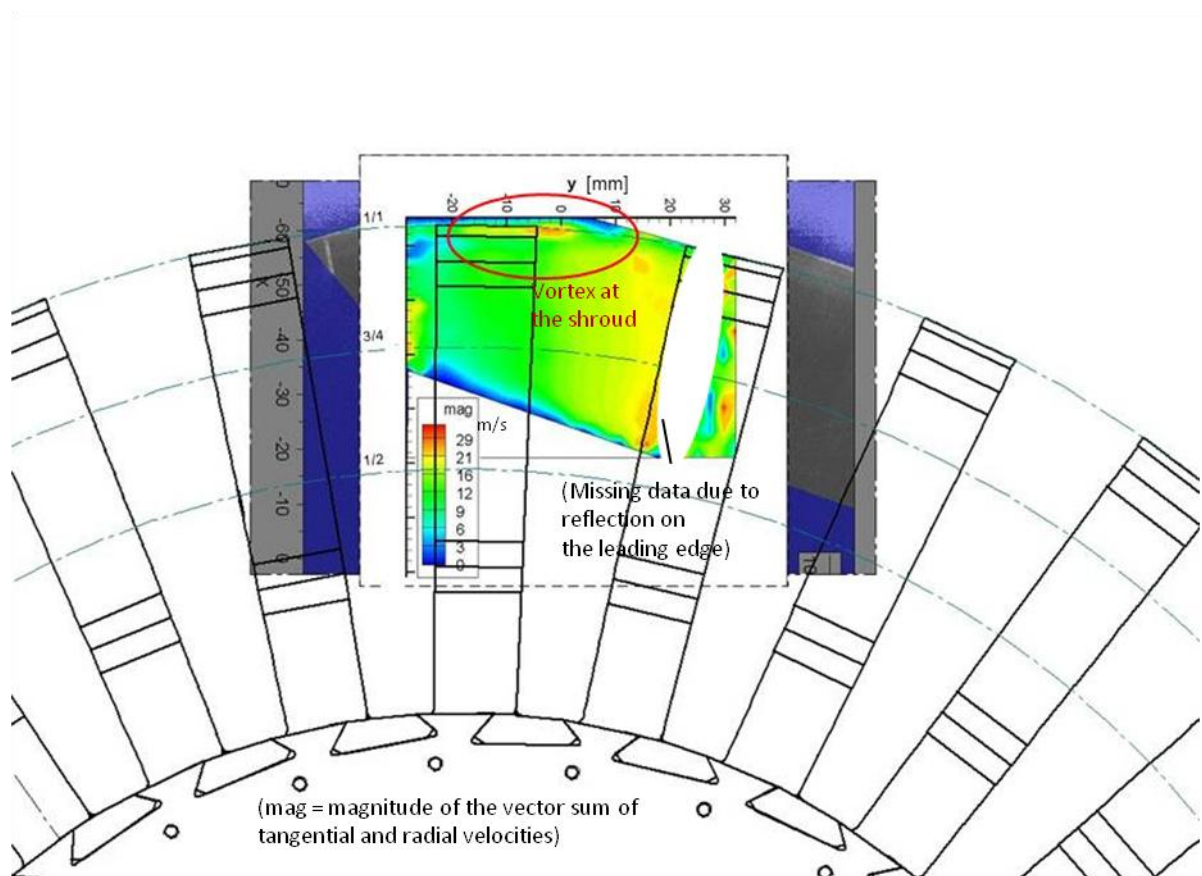


Figure 6.30: Distribution of the combined tangential / radial velocity field behind the wheel, overload

he vortex at the shroud is observed for operating points representing off-design, but it is not observed at the design point. For the partial load operating point, with a low value of the flow coefficient, vortices develop in the direction opposite to the swirl in the main flow and cause flow destabilization. For the overload operating point with a high value of the flow coefficient, these vortices do not counteract the main flow because they develop in the same direction as the swirl in the main flow. The boundary layer is energized but not destabilized by the turbulent structures. This explains the fact that the diffuser performs better for the operating points with high flow coefficients.

### 6.3. Blade wake investigation

In rotating turbomachinery, blade wakes can affect the flow in the downstream components, like turbine stages and diffuser parts. Study of the blade wakes in the core flow is needed to resolve the wake and to understand its influence on the flow structure. In this paragraph, a blade wake of a rotating bladed wheel is studied using PIV, resulting in a 3<sup>rd</sup> configuration, for a range of operating points, representing various turbine load conditions.

In the 3<sup>rd</sup> PIV configuration, the measurements are taken in a plane which intersects the blade at midspan, Fig. 6.31. A fragment of the configuration showing the measurement plane is shown in Fig. 6.32. A 90° endoscope is used to generate the laser section and is placed 150 mm downstream of the blades. A straight 0° camera endoscope is used. The distance between the camera endoscope and the measurement plane is 50 mm, which is 50% of the channel height. For all configurations, the camera was mounted on a remote-controlled traverse. The camera is positioned with an accuracy of 0.5 mm. The stiff mount minimizes errors caused by vibrations.

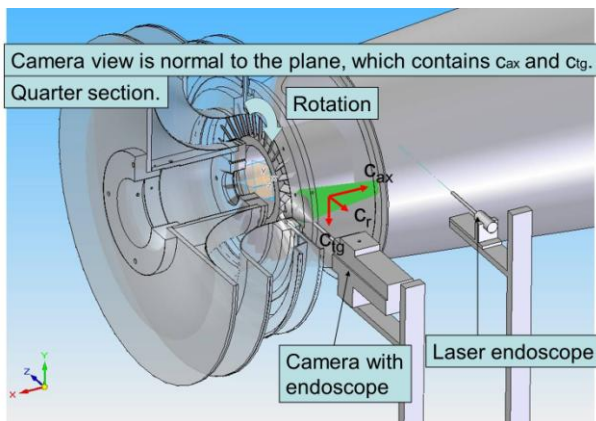


Figure 6.31: PIV configuration 3

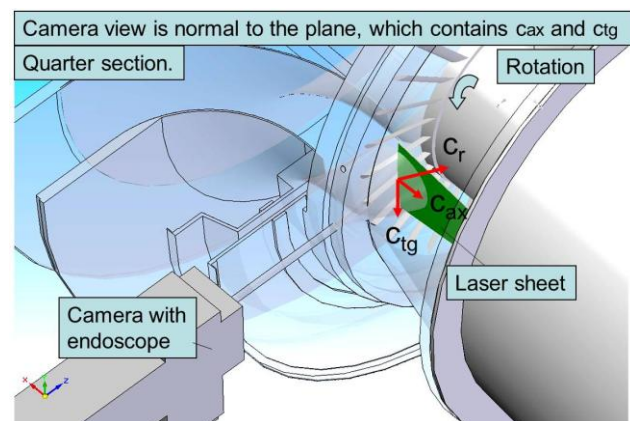


Figure 6.32: PIV configuration 3, fragment

The operating points, representing turbine rotor operating conditions, are given in Table 5. The rotating bladed wheel is driven by an electric motor to model the turbine part load conditions. Design point, partial load, and the overload conditions are set, such that approximately constant mass flow is maintained and adjusting the swirl angle by varying the rotational speed.

**Table 5. Operating points for configuration 3**

Operating point	Mass flow, kg/s	Rotational speed, rpm	Swirl angle, °
Partial load	Appr. 5 kg/s	2,916	-15°
		2,700	-10°
		2,436	-5°
Design point	Appr. 5 kg/s	2,322	0°
Overload	Appr. 5 kg/s	1,998	5°
		1,806	10°
		1,668	15°

The velocity field behind the bladed wheel for a partial load point is shown in Fig. 6.33. On the left side of the Figure, a sketch of the bladed wheel is drawn. In the background, a single PIV image is located. Average and single flow fields in terms of vorticity represent a blade wake of one of the 30 blades. Positive and negative vortices are observed detaching from the trailing edges of the blades and forming wakes.

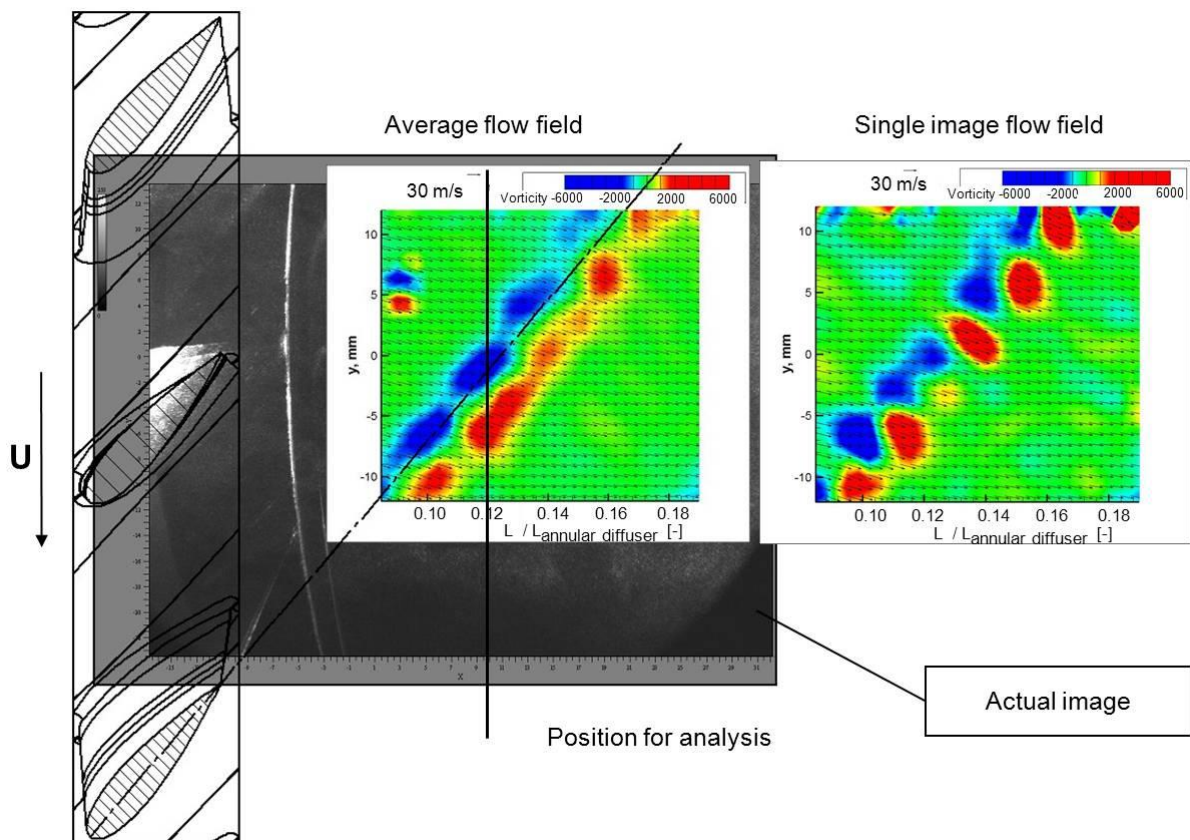


**Figure 6.33: Averaged and single vorticity fields behind the rotating bladed wheel**

Analysis of vortices is provided using parameters extracted from PIV velocity fields at a position at the diffuser length of 0.12, shown in Fig. 6.33. For every operating point, batches of 100 double-images similar to those shown in Fig. 6.33 were sorted out according to the

angular position of the rotor. Those pictures for which a particular chosen blade was in the same position with an error of  $\pm 0.5$  mm were averaged and then evaluated in terms of velocity and vorticity. X and Y coordinates are as shown in Fig. 6.33.

In Fig. 6.34 and 6.35, data extracted from PIV are shown for three typical operating points in terms of velocity and vorticity. In the wake, velocity is found to be lower than the main flow velocity. This reduction rises up to 4 m/s, which is about 10% of the main velocity in the test. For the overload operating point with positive swirl, the velocity drop is shifted in the direction of swirl (in the negative Y direction in Fig. 6.33) and is stronger. This can cause a rise in turbulence intensity resulting in higher pressure recovery. The smallest velocity reduction is found for the partial load point. The vorticity amplitude is found to be the lowest for this operating point, Fig. 6.35.

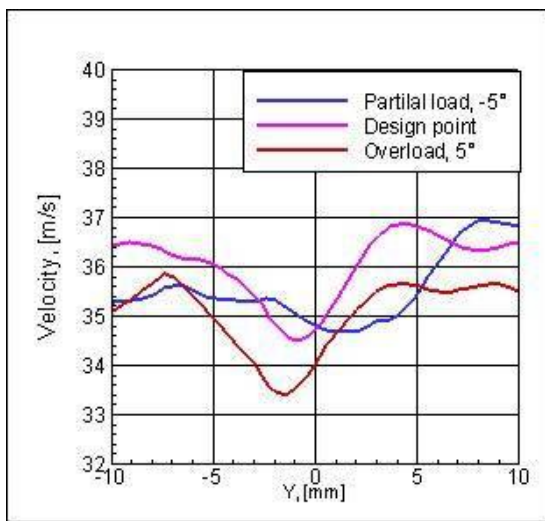


**Figure 6.34: Blade wake in the core flow in terms of velocity magnitude**

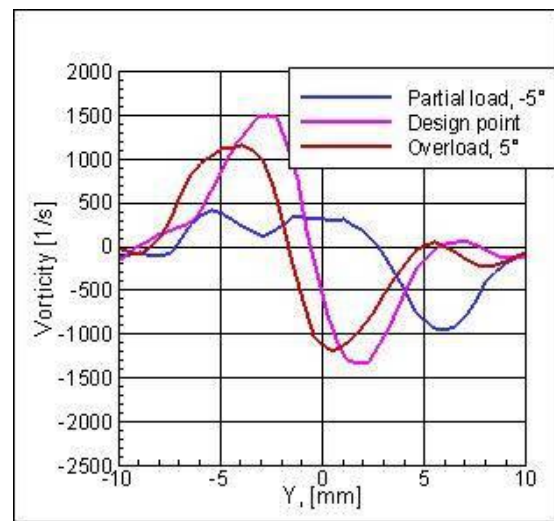


**Figure 6.35: Blade wake in the core flow in terms of vorticity**

Analysis of the vortex street, Fig. 6.37, is performed for a variety of swirl angles in the main flow. It shows smallest vortices for the design point ( $0^\circ$  swirl), which can be explained by favourable flow conditions at the symmetrical blades. The diameter of the vortices is growing for operating points with growing swirl angle. Negative vortices are bigger for all operating points except of the design point. Fig. 6.38 shows that vorticity in the wake does not significantly depend on the swirl angle; slightly higher values are detected for the design point.



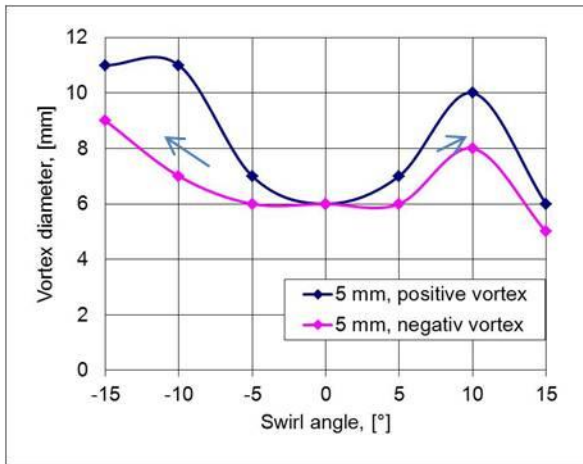


**Figure 6.36: Vortex diameter vs. swirl angle**

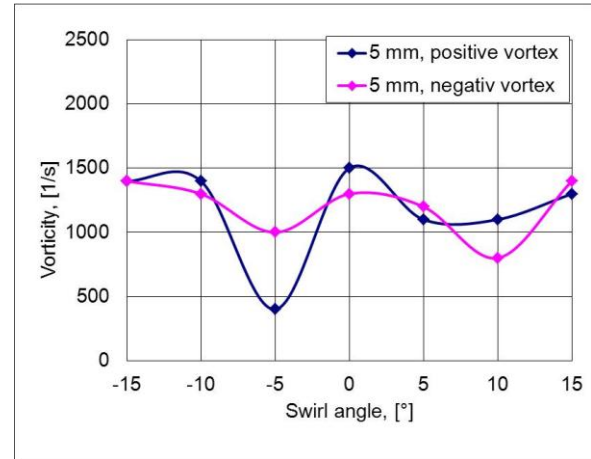


**Figure 6.37: Vorticity in the wake vs. swirl angle**

The present study of the blade wakes in the core flow thus shows that the velocity defect in the wakes, and size and frequency of vortices forming the wake weakly depend on the swirl angle and cannot be sufficient to explain the changes in the diffuser's pressure recovery. It can be concluded, that the influence of the blade wake on the flow structure in the endwall region considered in paragraphs 6.1-6.2 is of greater importance for pressure recovery.

## **7. Parameters dominating the pressure recovery in the diffuser**

Dimensionless parameters are needed to clarify the impact of numerous flow parameters in diffusers and to transfer results from experimental setups to real machines. The flow in a test rig can be said to be similar to the flow in a real diffuser only when geometric, kinematic, and dynamic parameters are the same for both. These parameters are at the same time decisive for diffuser performance.

The geometric parameters of the diffusers studied are listed in the Chapter “Interaction between Gas Turbine and Exhaust Diffuser”. A comparison of the geometric parameters of the test rig used for the present experiments and of the test rig of Chernikov (2008), whose results are used for comparison, is made in the chapter “Experimental facilities”.

Parameters, often referred to as kinematic parameters, describe the flow structure. When the load at the gas turbine is changed, the mass flow changes and the turbine exhaust flow pattern is changed. The flow entering the diffuser is then provided with swirl. The swirl angle, which depends on the turbine load conditions and is widely used in turbine design as a parameter, is applied together with the flow coefficient. These parameters were introduced in the chapter “Measuring programme”.

In addition to the PIV investigation of the flow features, analysis of the diffuser’s performance was done based on experimental investigations using pneumatic measuring techniques. A series of tests has been conducted in order to find the impact of the parameters which are relevant to the interaction between the gas turbine and the exhaust diffuser: swirl angle of the incoming flow, flow coefficient, and tip leakage flow parameters.

A set of operating points was studied which has two advantages. Firstly, the similarity to the real turbine operating conditions is improved compared with the previous research of Sieker and Seume (2008) and Fleige (2002) by using a rotating bladed wheel as a turbine stage simulator together with the tip leakage flow insert. This combined setup allows setting a flow structure closer to the real conditions, because the ratio of the mass flow in the leakage flow produced by the bladed wheel to the mass flow in the main flow was not corresponding to real conditions. Secondly, the similarity of dimensionless parameters to those in the research of Chernikov (2008) allows validation of the results. This is useful because Chernikov used a scaled turbine stage model in his research.

The present set of operating points was studied by means of a pneumatic measuring technique and LDA in order to analyse the dependence of diffuser’s performance on the dimensionless parameters. Evaluation of the diffuser’s performance is based on analysis of velocity distributions in the inlet of the annular diffuser, outlet annular diffuser-inlet conical diffuser, and outlet conical diffuser; pressure recovery, total pressure loss and kinetic energy loss coefficients, calculated using radial distributions of pressure and static pressure along the diffuser.

## 7.1. Results with the bladed wheel and with the tip leakage flow

Experiments were carried out for two Mach numbers of 0.1 and 0.12, keeping the mass flow almost constant, respectively. The range of operating points represents different turbine load conditions. These are the partial load with flow coefficient of 0.66, and swirl angle  $-5^\circ$ , the design mode with flow coefficient 0.74 and straight inflow and the overload, for which flow coefficient is between 0.83 and 1.09 and swirl angles vary up to  $15^\circ$ . The swirl in the leakage flow was kept approximately  $-20^\circ$ . Table 6 shows tested conditions. In real turbines, for unshrouded last blades, the swirl results from the vector sum of the leakage flow across the tip and the circumferential velocity. For shrouded blades, it is the vector sum of the labyrinth leakage and the circumferential velocity.

**Table 6. Operating points NACA rotor + tip leakage flow**

Name	n, rpm	swirl angle main flow, [°]	Flow coefficient $\phi$
15° annular + 5° conical diffuser + NACA-profiled rotor + tip leakage flow			
$\dot{m}=5 \text{ kg/s}$ , $\dot{m}_{\text{leakage}}=0.1 \text{ kg/s}$ ( $\approx 2\%$ of the total), $\text{Ma}=0.1$ , leakage swirl angle $-20^\circ$			
V242	2,496	$-5^\circ$	0.66
V243	2,286	$0^\circ$	0.74
V244	2,052	$5^\circ$	0.83
V245	1,818	$10^\circ$	0.97
V246	1,608	$15^\circ$	1.09
$\dot{m}=6 \text{ kg/s}$ , $\dot{m}_{\text{leakage}}=0.14 \text{ kg/s}$ ( $\approx 2.3\%$ of the total), $\text{Ma}=0.12$ , leakage swirl angle $-20^\circ$			
V262	3,000	$-5^\circ$	0.66
V263	2,736	$0^\circ$	0.74
V264	2,454	$5^\circ$	0.84
V265	2,112	$10^\circ$	0.99

### 7.1.1. Flow parameter distributions

The velocity distributions vs. the channel height are considered as shown in Fig. 7.1 in the inlet and outlet of the annular diffuser and at the outlet of the conical diffuser.

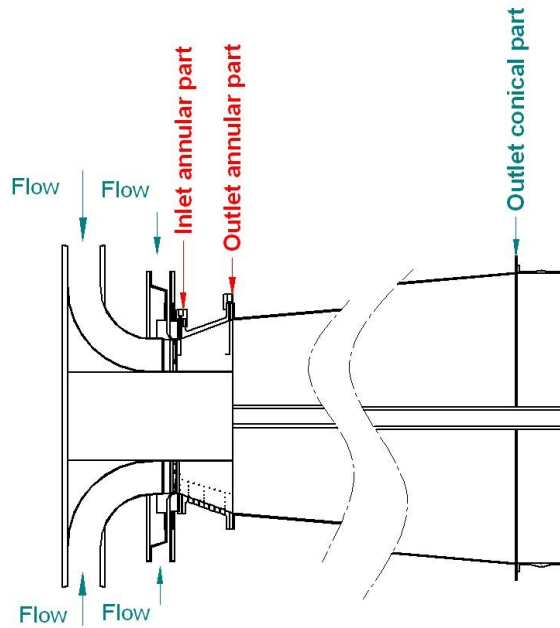


**Figure 7.1: Measurement setup**

The velocity distribution in the inlet of the annular diffuser helps to understand processes in the diffuser and is shown for Mach number 0.1 in Fig. 7.2 for axial and in Fig. 7.3 for tangential velocities respectively. The mass flow in the leakage flow was about 0.1 kg/s or approximately 2% of the total mass flow. The uncertainty of the probe measurements is below 0.5% and thus is too small to be shown in diagrams. The strong influence of tip leakage can be noticed at the shroud in both distributions. Axial velocity profiles are nearly uniform. With increasing swirl in the main flow, velocity reduction at the shroud decreases.

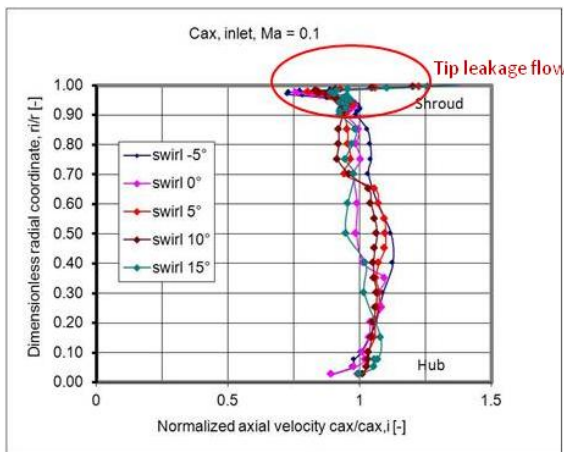


**Figure 7.2: Axial velocity at the inlet of annular diffuser vs. swirl angle, Ma=0.1**

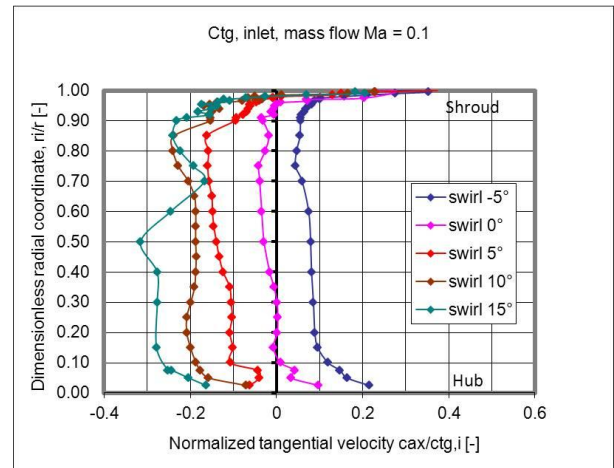


**Figure 7.3: Tangential velocity at the inlet of annular diffuser vs. swirl angle, Ma=0.1**

The velocity distribution in the inlet of the annular diffuser for a slightly higher Mach number of 0.12 is shown in Fig. 7.4 for axial and in Fig. 7.5 for tangential velocities, respectively. The mass flow in the leakage flow was about 0.12 kg/s or approximately 2.3% of the total mass flow. The ratio between velocities in the leakage and the main flow is approximately the same as in tests with Mach number of 0.1.

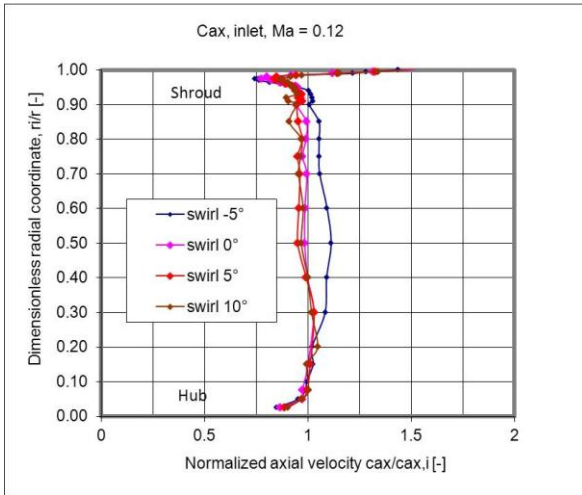


**Figure 7.4: Axial velocity at the inlet of annular diffuser vs. swirl angle, Ma=0.12**

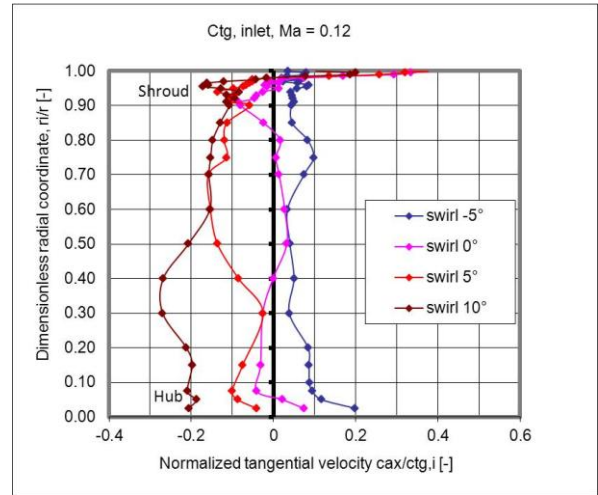


**Figure 7.5: Tangential velocity at the inlet of annular diffuser vs. swirl angle, Ma=0.12**

The axial velocity distribution in the outlet of the annular diffuser (inlet conical diffuser) is shown for Mach number 0.1 in Fig. 7.6. The casing and the hub boundary layer have grown significantly, compared to the inlet of the diffuser.

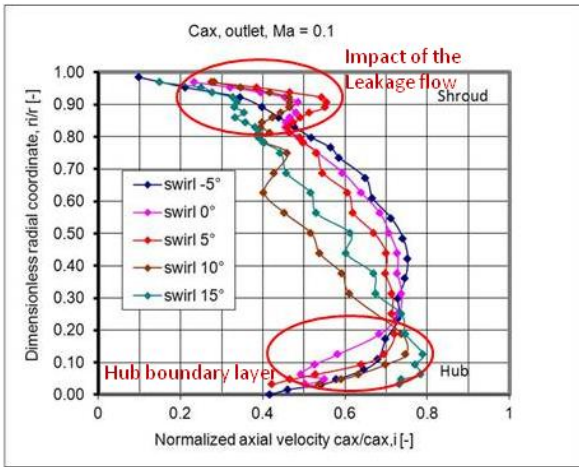


**Figure 7.6: Axial velocity at the outlet of annular diffuser vs. swirl angle, Ma=0.1**

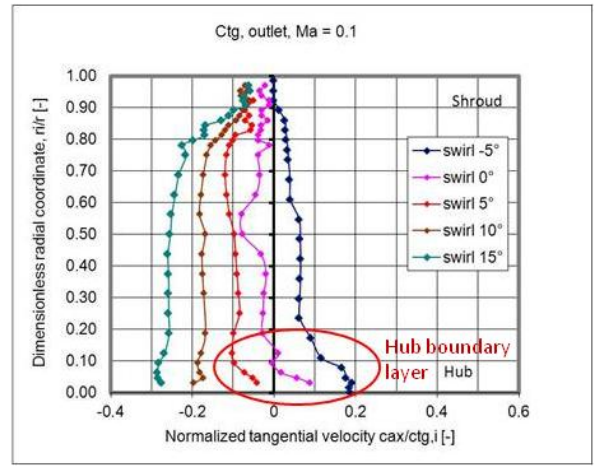


**Figure 7.7: Tangential velocity at the outlet of annular diffuser vs. swirl angle, Ma=0.1**

For all operating points, the flow does not separate. Operating points with a small positive swirl of 5°, 10°, and 15° have shifted flow to the hub velocity profile with a velocity increase near the shroud. In this case, the flow near mid-span is decelerated due to a velocity increase on the hub. For the swirl angle of 5° the impact of the leakage flow is the strongest.

For operating points with straight inflow and with negative swirl of -5°, the velocity profile is very smooth with thick boundary layers at the shroud and the hub. The influence of the leakage flow is not found anymore and separation tendencies decelerate the flow at the walls.

From previous studies made by Fleige (2002), it is known that strong swirl causes separation on the hub, affecting the diffuser function; this tendency is suppressed due to the turbulent effects introduced by the operating bladed wheel and the additional leakage flow.

The distribution of tangential velocities in Fig. 7.7 shows a reduction of velocity in this zone affected by the leakage flow upstream for all operating points. Near the hub, there is a tendency to positive swirl.

The velocity distribution in the outlet of the annular diffuser (inlet conical diffuser) is shown for Mach number 0.12 in Fig. 7.8 for axial and in Fig. 7.9 for tangential velocities, respectively. The impact of the leakage flow is stronger than in tests with a Mach number of 0.1. Operating points with negative swirl or without swirl have the most uniform velocity profile. Swirl of  $10^\circ$  together with the leakage flow result in a flow structure with energized boundary layers. Tangential velocities at the shroud are shifted to the negative side.

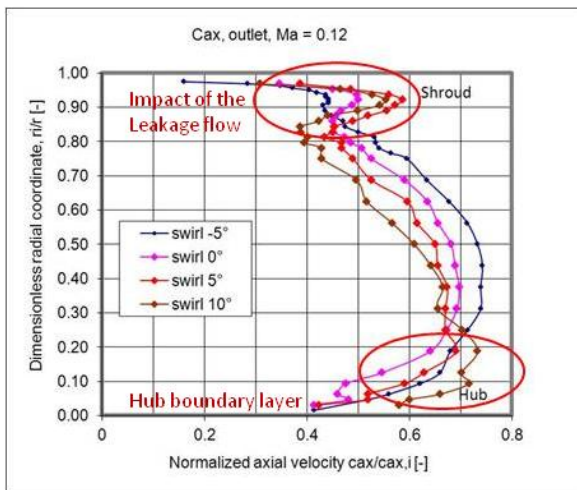


**Figure 7.8: Axial velocity at the outlet of annular diffuser vs. swirl angle, Ma=0.12**

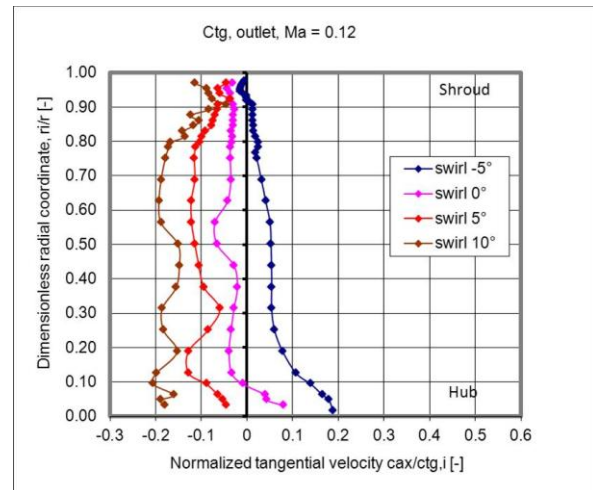


**Figure 7.9: Tangential velocity at the outlet of annular diffuser vs. swirl angle, Ma=0.12**

The axial velocity distribution in the outlet of the conical diffuser is shown for a Mach number of 0.1 in Fig. 7.10. The most favourable uniform distribution is found for  $5^\circ$  positive swirl. Strong core flow is established, however the flow at the shroud is reduced most compared with other operating points. With increasing swirl, the flow is moving to the shroud while decelerating in the middle of the conical diffuser. Fig. 7.11 shows tangential velocities in the outlet of the conical diffuser. In the flow in the middle of the diffuser the swirl disappears for all operating points, i.e. the tangential component is eliminated. At the shroud, the swirl is strong. As the measurements in the outlet of the conical diffuser were done using LDA, RMS-velocity distributions could be acquired simultaneously. Turbulence intensity distributions could be calculated and are shown in Fig. 7.12. For all operating points, the turbulence intensity is approximately the same. The operating point with  $10^\circ$  swirl has less unsteady flow in the diffuser. In Fig. 7.13 the measurement position is highlighted.

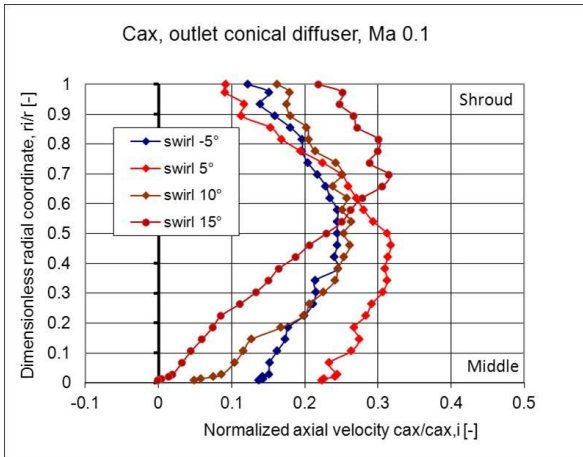


Figure 7.10: Axial velocity, outlet of conical diffuser vs. swirl angle, Ma=0.1

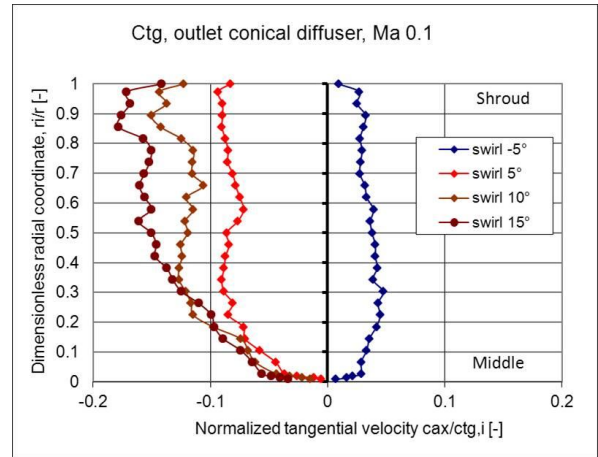


Figure 7.11: Tangential velocity, outlet of conical diffuser vs. swirl angle, Ma=0.1

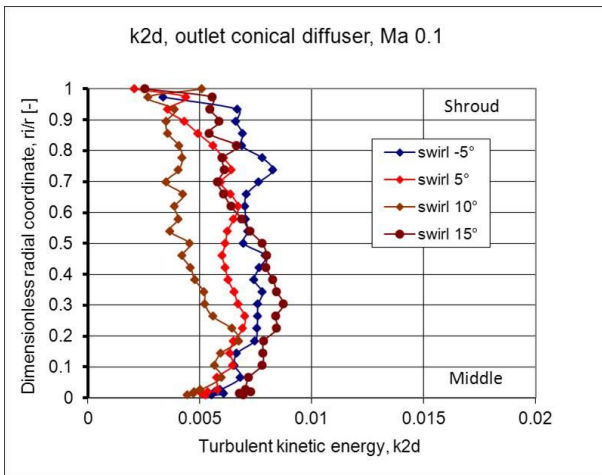


Figure 7.12: Turbulent kinetic energy, outlet of conical diffuser vs. swirl angle, Ma=0.1

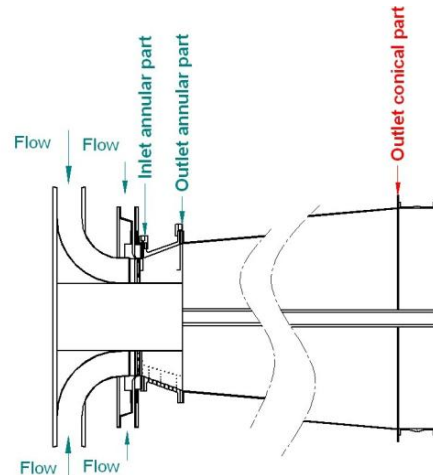
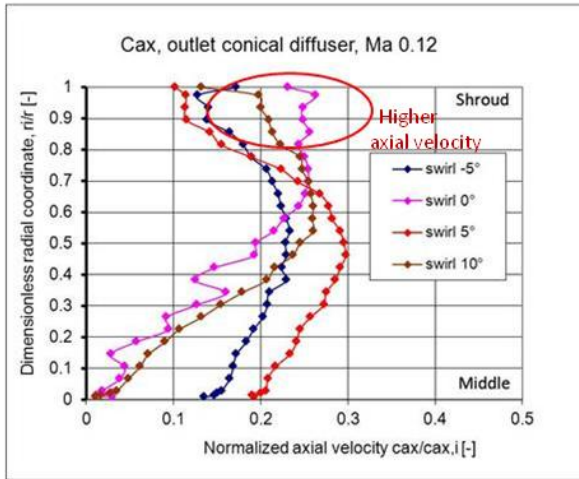


Figure 7.13: Measurement setup



The axial velocity distribution in the outlet of the conical diffuser for a Mach number of 0.12 is shown in Fig. 7.14. Higher axial velocities are found at the shroud for operating points with  $0^\circ$  swirl and  $10^\circ$ . The most uniform profile is measured for  $5^\circ$  positive swirl just as in the test with Mach number 0.1. This uniformity of the flow which can be also noticed in Fig. 7.15 explains the best pressure recovery at this operating point (Fig. 7.18). In Fig. 7.15, an almost constant tangential velocity is provided in the whole channel for this operating point. Turbulence intensity distributions shown in Fig. 7.16 are similar to those in tests with a Mach number of 0.1.



**Figure 7.14: Axial velocity, outlet of conical diffuser vs. swirl angle, Ma=0.12**

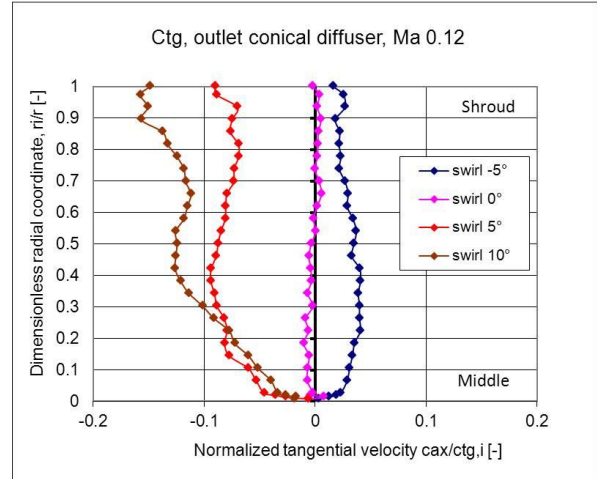


**Figure 7.15: Tangential velocity, outlet of conical diffuser vs. swirl angle, Ma=0.12**

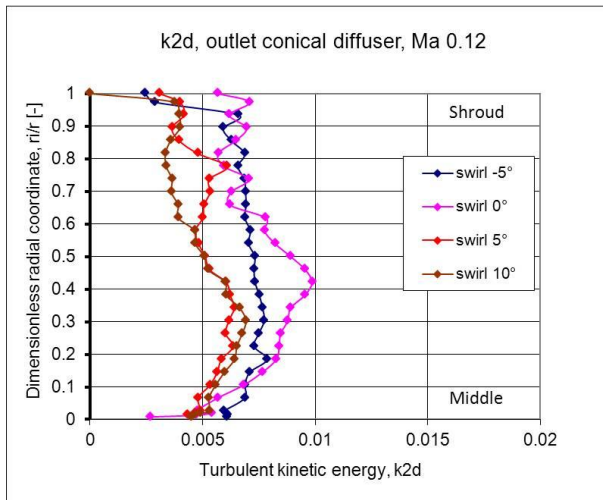


**Figure 7.16: Turbulent kinetic energy, outlet of conical diffuser vs. swirl angle, Ma=0.12**

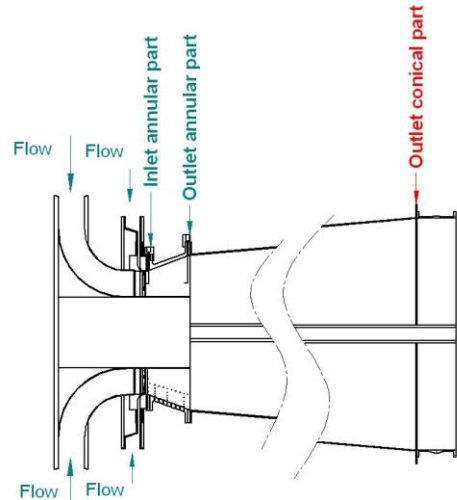


**Figure 7.17: Measurement setup**



### 7.1.2. Coefficients

The pressure recovery trends for operating points with swirled tip leakage flow are given in Fig. 7.18. High pressure recovery can be explained by the influence of leakage flow, which was noticed in velocity distributions for almost all conditions. The combination of swirl in the main and the leakage flow affects the pressure recovery by energizing the shroud boundary layer and the flow does not separate for all operating points. The highest pressure recovery is for operating points with positive swirl, while negative swirl angles result in lower diffuser performance. This tendency is more developed for tests with a Mach number of 0.1. A higher difference between swirl angles in the main and the leakage flow smoothed the velocity profiles and counteracted the separation. Kinetic energy losses are shown in Fig. 7.19. These losses depend on the Mach number. Higher velocity at the outlet results in higher losses because more kinetic energy of the flow is not utilized. These losses increase with growing swirl because the tangential component is not used in the process of pressure recovery. Total pressure losses shown in Fig. 7.20 decrease a little for the operating points with moderate swirl compared to the  $0^\circ$  swirl operating point. Beneficial vortex structures in the diffuser inlet introduced by the bladed wheel stabilized the flow, caused uniform flow distributions downstream in the diffuser, prevented separation, and resulted in lower total pressure losses.

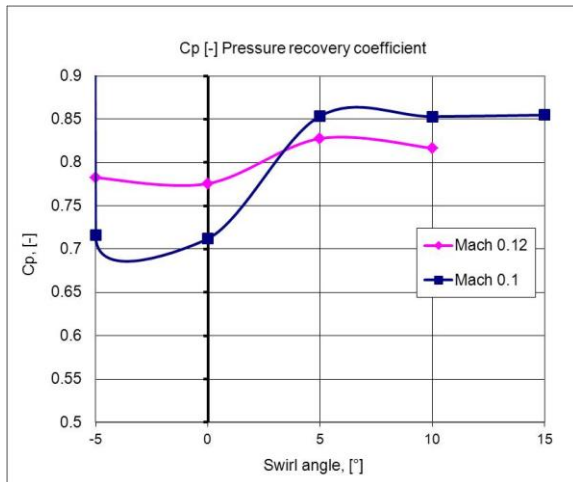


Figure 7.18: Pressure recovery for the whole diffuser vs. swirl angle and mass flow

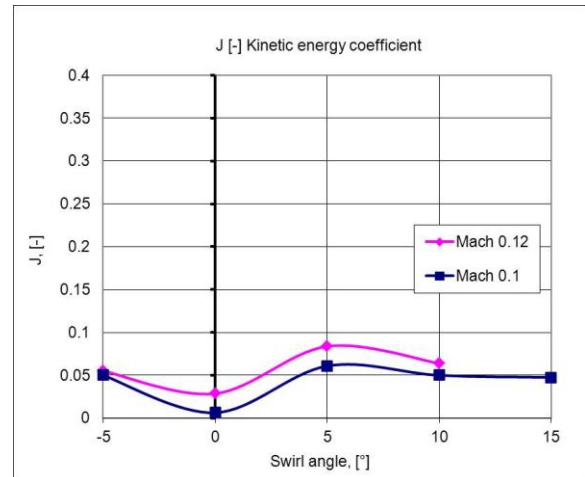


Figure 7.19: Kinetic energy for the whole diffuser vs. swirl angle and mass flow

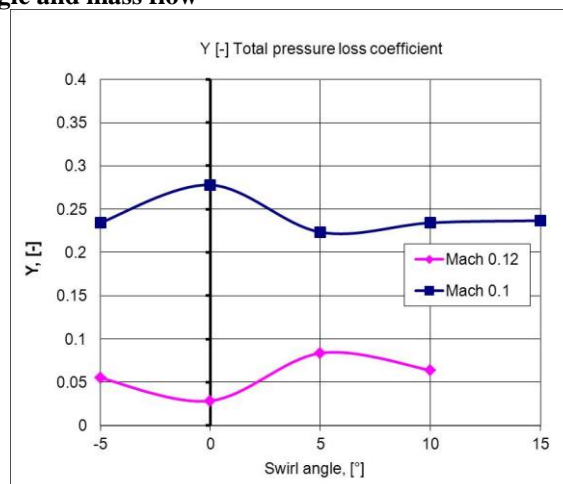


Figure 7.20: Total pressure loss for the whole diffuser vs. swirl angle and mass flow

## 7.2. Results without a bladed wheel and with tip leakage flow

Three operating points were studied for the test rig configuration without a bladed wheel and for an annular diffuser with an opening angle of  $15^\circ$ . To produce swirl in the inlet flow, a mechanical swirl generator was used instead of the bladed wheel. The motivation is to understand the influence of the bladed wheel when the flow is provided with leakage flow, separating the influence of the bladed wheel. Using the methodology of Fleige et al. (2002), swirl angles in the main and leakage flow were adjusted by bending sheet metal vanes in the stationary swirl generators. Table 7 shows the tested conditions.

**Table 7. Operating points tip leakage flow**

Operating point	swirl angle main flow, [°]	Swirl in the leakage flow [°]
15° annular + 5° conical diffuser + Tipp leakage flow		
$\dot{m} = 5 \text{ kg/s}$ , $Ma = 0.1$ , $\dot{m}_{\text{leakage}} \approx 0.1 \text{ kg/s}$ ( $\approx 2\%$ of the total)		
V110 Design point	0 (90)	$\pm 19$
V111 Overload 120%	18 (108)	-14.5
V112 Partial load 80%	$\pm 25$ (65)	$\pm 25.25$

### 7.2.1. Flow parameter distributions

In the axial velocity distributions at the inlet to the annular diffuser for all three operating points shown in Fig. 7.21, higher velocity in the leakage area is measured. Figure 7.22 shows that the flow changes its circumferential direction along the channel.

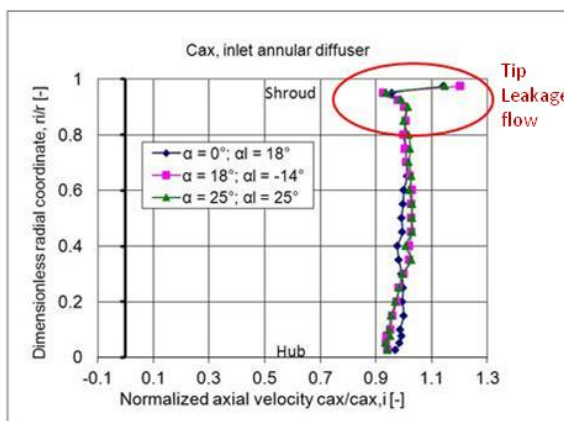


**Figure 7.21: Axial velocity at the annular diffuser inlet vs. swirl angle**

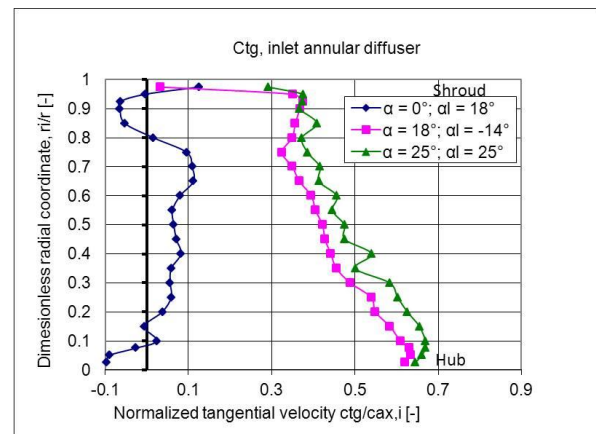


**Figure 7.22: Tangential velocity at the annular diffuser inlet vs. swirl angle**

At the outlet, shown in Fig. 7.23, separation is detected at the hub for both off-design operating points, i.e. partial load and overload. A back flow zone at the hub takes

approximately 17% of the channel height. This is due to high swirl angles of  $18^\circ$  and  $25^\circ$  in the main flow, Fig. 7.24. The flow is rotated in the annular part, and due to the centrifugal forces, axial and tangential velocities are very high at the shroud and decrease towards the hub.

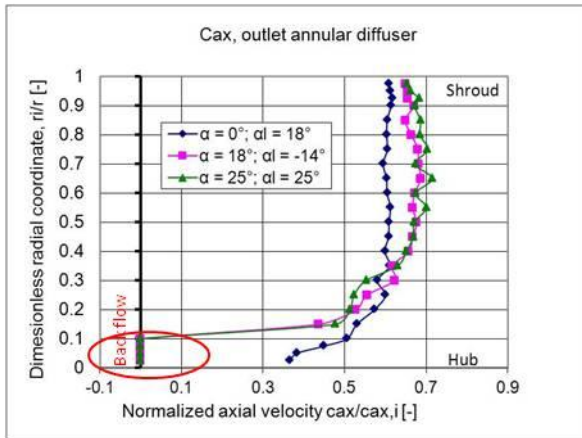


**Figure 7.23: Axial velocity at the ring diffuser outlet vs. swirl angle**

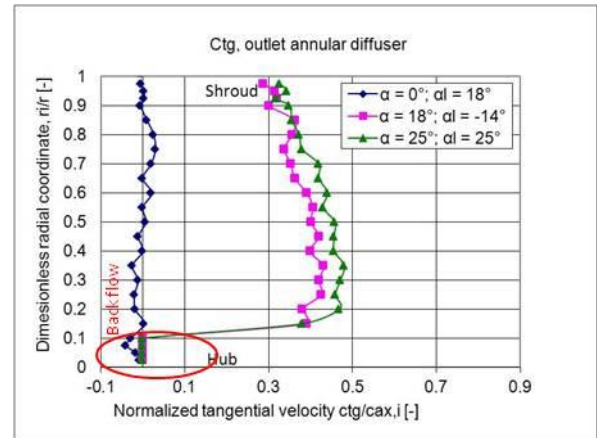


**Figure 7.24: Tangential velocity at the ring diffuser outlet vs. swirl angle**

## 7.2.2. Coefficients

Distribution of the pressure recovery coefficient in Fig. 7.25 shows the best performance for the design point. Separation at the hub, caused by great centrifugal forces at the off-design point, worsened the performance. At overload, pressure recovery is higher than at partial load. This is due to greater difference in the swirl of the main and the leakage flows. The lowest pressure recovery is for the partial load point, where this difference is smaller. For the design point, the leakage flow, injected in the inlet, has energized the boundary layer.

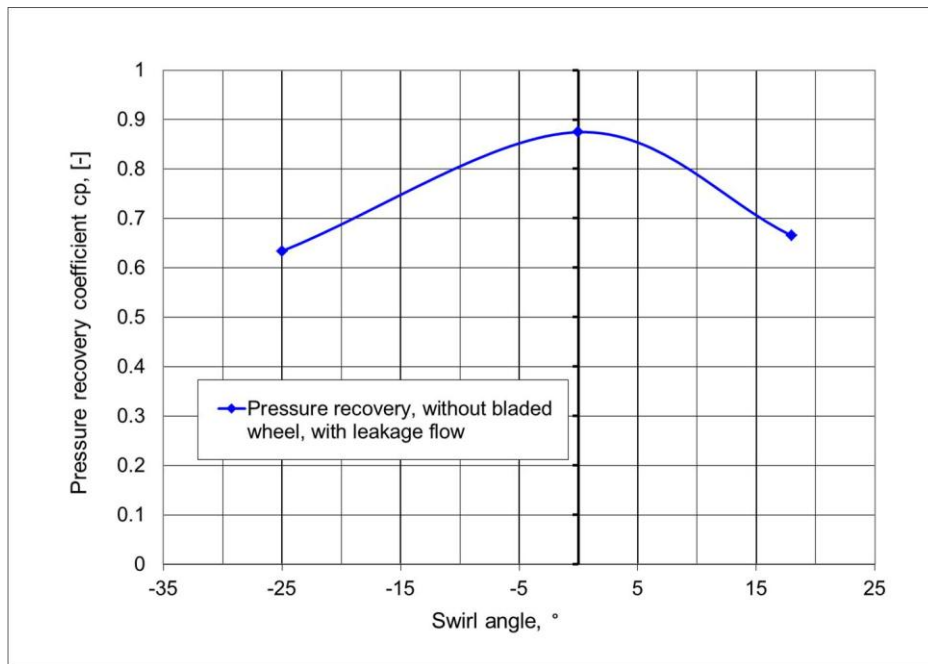


**Figure 7.25: Pressure recovery for the whole diffuser vs. swirl angle**

### 7.3. Results with turbine stage model (Chernikov)

Investigating the dependence of the diffuser's pressure recovery on the turbine operating mode, Chernikov (2008) varied inlet swirl angle of the flow coming into diffuser from the scaled turbine model while keeping Mach number constant at 0.14, 0.21, and 0.25. These measurements are used for validation of the results of the current research.

In Fig. 7.26, distributions of axial velocities are shown for diffuser inlet of Chernikov, in order to highlight similarity to the current research modelling approach and enable a comparison of pressure recovery, which is provided in paragraph 7.4. Strong leakage flow can be observed as well as the influence of secondary flows from the bottom part of the blade's passage. It is stated, that these flows result in chains of vortices encircling the diffuser's hub and interacting with the main flow. This influence is stated by Chernikov to be very important for the diffuser's performance and proposed for further investigation using unsteady measurement techniques. For most of the operating points, flow changes direction of the rotation along the channel height, Fig. 7.27. Pressure recovery for these operating points is considered in the following paragraph.

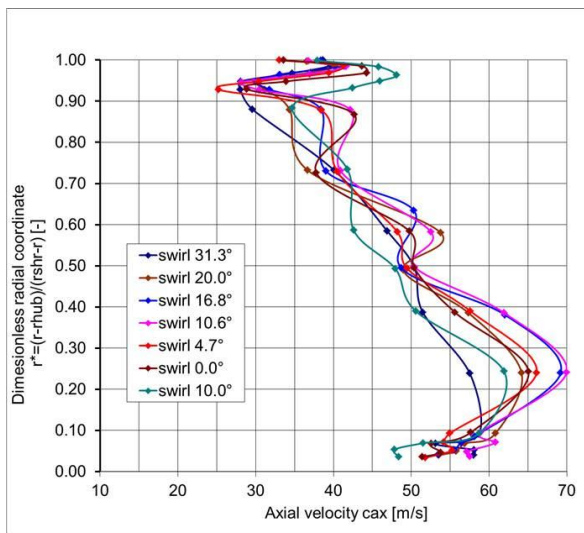


Figure 7.26: Velocity at the ring diffuser inlet vs. swirl angle (Chernikov, 2008)

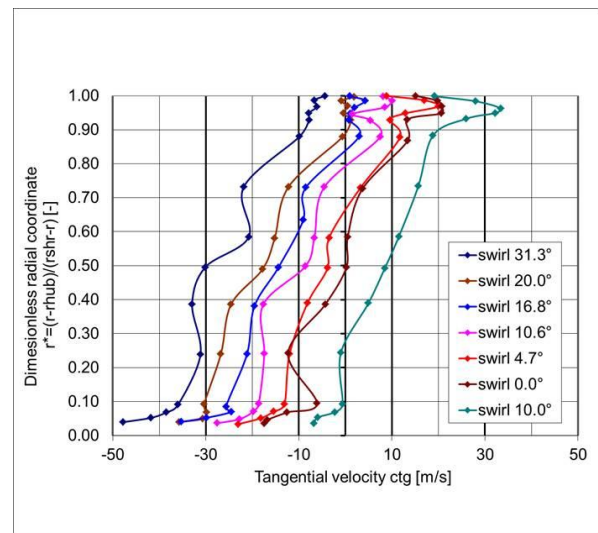
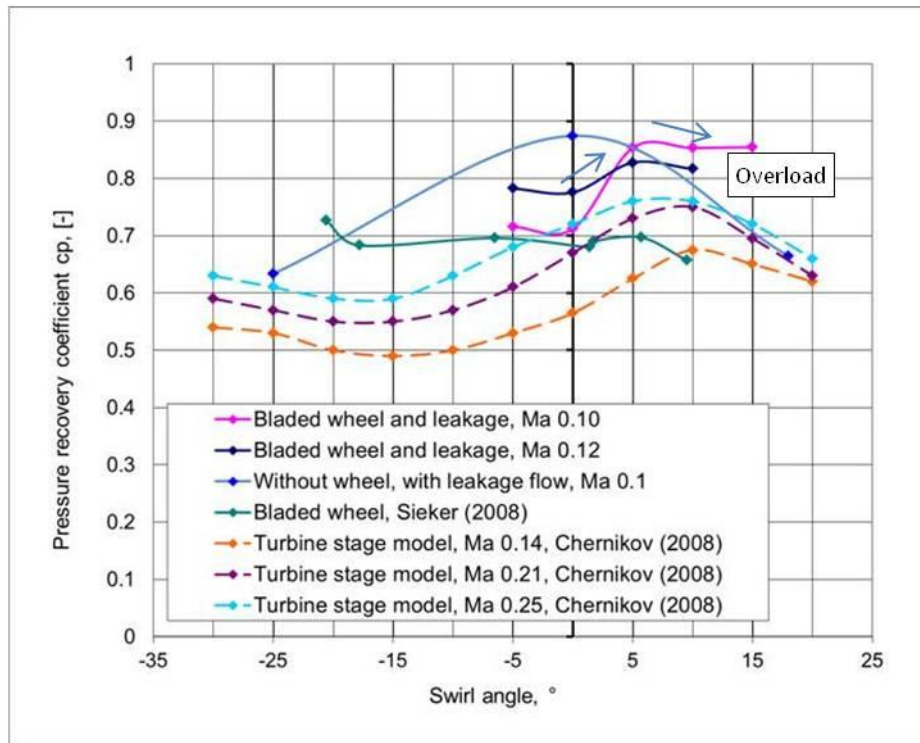


Figure 7.27: Velocity at the ring diffuser inlet vs. swirl angle (Chernikov, 2008)

## 7.4. Comparison of results

In Fig. 7.28 the pressure recovery of the whole diffuser is given as a function of the inlet swirl angle and the Mach number. Pressure recovery for tests with additional leakage flow and with the bladed wheel is the best for the  $5^\circ$  positive swirl. With increasing swirl angle up to  $10^\circ$  and  $15^\circ$ , the pressure recovery coefficient is decreasing slowly. Decreasing the swirl to  $-5^\circ$  reduces  $c_p$ . Variation of mass flow, and therefore, Mach number, shows the dependence on swirl angle is stable.



**Figure 7.28: Pressure recovery, whole diffuser, vs. swirl angle and mass flow, comparison**

The performance of the diffuser is good for almost all of the studied mass flow and swirl values, with the pressure recovery in the whole diffuser not dropping below 0.7 for most operating points. A higher Mach number generally results in a higher pressure recovery, and the trend pressure recovery vs. swirl is constant. With growing Mach number, an increase in pressure recovery is observed. The pressure recovery for the Mach number of 0.1 is a little higher than for 0.12 for the swirl angle of  $-5^\circ$  and  $0^\circ$ . The higher the Mach number, the steeper the swirl-  $c_p$  trend is. The Mach number of 0.12 gives the most favourable distribution in the range  $-5^\circ \dots 10^\circ$ , but for the swirl of  $-10^\circ$  the drop is significant.

As seen when comparing the points with leakage flow with and without the bladed wheel, pressure recovery for the latter is higher in overload operation. This can be explained by the influence of turbulent structures, which suppress boundary layer separation tendencies.

In order to validate results taken on the diffuser test rig at the Leibniz Universität Hannover, the results of Chernikov (2008) are used. Modeling of the unsteady effects using the bladed wheel is compared with methodology which utilized a scaled turbine stage. Swirl was adjusted varying conditions on the scaled turbine stage model. The operating points of Chernikov show pressure recovery to depend on the swirl direction in the main flow and on Mach number, increasing with increased Mach number. The best performance is found for moderate positive swirl angles and is not changing with varied Reynolds number. The trend remains the same for all Mach numbers. The difference in experimental values of pressure recovery for the two test rigs is primarily due to the different geometric parameters (see paragraph 3.3).

The beneficial effect of the leakage flow can be seen when comparing these results to the operating points of Sieker and Seume (2008). Pressure recovery for the points with additional leakage flow and with/without bladed wheel is higher.

## 8. Conclusions

The performance of turbine exhaust diffusers is evaluated using the coefficient of pressure recovery. Pressure recovery in diffusers was studied and explained based upon measurements of the phenomena in the diffuser flow, applying a range of measurement techniques: Endoscopic PIV, pressure probes, and LDA. The influence of several main factors on pressure recovery, e.g. the swirl, the turbulence, the tip leakage flow, and the blade wakes is studied. A sophisticated approach of the endoscopic PIV was realized in measurements on a rotating test rig. The interaction between the diffuser's boundary layer and the effects introduced by the bladed wheel was studied.

As observed by others, the flow structure and unsteady effects are responsible for the dependence of the diffuser's performance on the bladed wheel operating conditions. Turbulence introduced in the flow by the bladed wheel is important. More precisely, unsteady flow structures which are identified in regions with a high turbulence level contribute significantly to the stabilizing/destabilizing effects of the bladed wheel, depending on their direction.

In the present work, blade wakes introduced by the bladed wheel are found to be responsible for diffuser performance. Study of the blade wakes in the core flow showed that the velocity defect in the wakes, the size and the frequency of vortices forming the wake depend on the swirl angle (and the flow coefficient). However, this dependence is insufficient to explain the changes in the diffuser's performance, because for diffuser channels influence of blade wakes is much more significant in the boundary layer, where they interact with the boundary layer. This interaction was visualized and studied, with the following results and conclusions.

Large vortices, originally separated from the blades, are found in the annular diffuser inlet close to the shroud. They come from the upper part of the blade passage and affect the boundary layer on the diffuser's shroud. When the bladed wheel operates at the design point (without swirl in the main flow), these vortices are suppressed very early by the main flow and mixed. Turbulence intensity is decreasing in the downstream direction. The expansion process in the diffuser is stable.

For the operating point with a low value of the flow coefficient (negative swirl), vortices are about two times stronger than for the design point and survive. The mixing process is weak and the boundary layer is destabilized. Separation tendencies are induced which result in coherent back flow zones which are found in the single PIV images and in separation at about 1/3 the diffuser length found in the averaged flow field. The unstable boundary layer leads to a decrease of pressure recovery for the annular diffuser due to the reduction of the effective diffuser cross sectional area.

For the operating point with positive swirl (a high value of the flow coefficient), these vortices are also strong and are found downstream. However, pressure recovery in the annular diffuser is even higher than for the design point. This can be explained by two facts: firstly,

the turbulence level in the core flow is very high. Turbulent energy is better transported to the peripheral zones of the channel by the swirled flow.

Secondly, vortices in the inlet of the diffuser must be considered in the third dimension, in terms of tangential and radial velocity components. For the design point, vortices are so weak that they are not even detected. For the operating points with a low value of the flow coefficient, vortices develop in the direction opposite to the swirl in the main flow and just cause flow destabilization. For the operating point with a high value of the flow coefficient, these vortices do not counteract the main flow because they develop in the same direction as the swirl. The boundary layer at the shroud is thus energized, and separation tendencies are suppressed.

Pressure recovery coefficients, calculated for different diffuser configurations, significantly depend on the flow coefficient and swirl. This occurs due to change in the development of vortical structures downstream of the rotor blade tip area. The diffuser performance diagrams for the different inlet flow conditions introduced by the rotating bladed wheel show that positive swirl of about  $5\text{-}10^\circ$  has a positive effect on the pressure recovery while negative swirl, for the most cases, decreases  $c_p$ . This trend remains for all values of Mach number for the same diffuser geometry.

For the operating points measured with a bladed wheel and additional leakage flow, pressure recovery is found to be very high. The tip leakage flow energizes the inlet casing boundary layers and, if it is introduced along the outer cone, decreases the velocity profile distortions at the diffuser outlet.

The results of previous investigations on the same test rig of Sieker and Seume (2008), as well as results of investigations on another test rig, for which parameters are nearly the same, Chernikov (2008), are taken into consideration in order to prove the dependence of diffuser performance on these parameters. The performance tendencies are found to be similar to those obtained for a more gas turbine-like test rig with a scaled last turbine stage model and a similar geometry.

In future investigations, modern measurement techniques like PIV should be further applied to turbomachinery as they can provide explanations for the complex effects on blades, diffuser struts, and other components in the turbomachine flow path. Unsteady PIV with measuring frequency in kHz range or hot wire anemometry can contribute to an understanding of the dynamics of unsteady flow structures. The results of this thesis can be applied for validation of numeric calculations of diffuser flows with Computational Fluid Dynamics tools.



## 9. Literature

- Alhaj O., Seume J.R., (2010) Optical Investigation of Profile Losses Coefficient in a Linear Turbine Cascade, GT2010-23166, ASME TURBO EXPO, June 14-18, 2010, Glasgow, UK
- Badreddine R., Lawrenz M., (2009): Messung selbsterregter periodischer Strömungen. Symposium 25 Years of PIV in Aerodynamics, Göttingen, September 23-25, 2009
- Balevic D., Hartman S., Youmans R., (2009): Heavy-Duty Gas Turbine operating and Maintenance considerations GER 3620L (11/09) GE Energy Atlanta, GA
- Bryanston-Cross P. et al., (2000): Intelligent diagnostic optics for flow visualization. Optics and Laser Technology 32:641-654
- Chernikov V. A., (2008): Test Bench for Gas-dynamic Investigations of Exhaust Diffusers and Hoods of Turbines, Thermal Engineering, Vol. 55, No. 6, pp. 499–505.
- Chernikov V., Semakina E., (2009): Aerodynamic characteristics of the exhaust axial diffuser of the stationary gas turbine at various regimes of its operation, No. 2 2009 “Energeticheskie mashini i ustanovki”, Russian text
- Denton, J.D., (1993): Loss Mechanisms in Turbomachines, ASME Journal of Turbomachinery, 115, pages 621- 632
- Deytch, M., Zaryankin, A., (1970): Gasdynamik von Austrittsdiffusoren in Turbomaschinen, Moskau, Energiya, Russian
- Estevadeordal J., Gogineni S., Goss L., Copenhaver W., Gorrell S., (2002): Study of Wake-Blade Interactions in a Transonic Compressor Using Flow Visualization and DPIV. Journal of Fluids Engineering, 124:166-175
- Feldcamp, G.K., Birk, A.M. (2006): Strut losses in a diverging annular diffuser with swirling flow, ASME Turbo Expo 2006: Power for Land, Sea and Air May 8-11, 2006, Barcelona, Spain GT2006-90566
- Fischer, W. J., (2010): Siemens H class turbine, the SGT5-8000H ready for the market: a "giant" gas turbine sets new benchmarks, Mechanical Engineering-CIME, [www.allbusiness.com/energy-utilities/utilities-industry-electric-power](http://www.allbusiness.com/energy-utilities/utilities-industry-electric-power).
- Fleige H.-U., Riess W.; Seume J.R., (2002): Swirl and tip leakage flow interaction with struts in axial diffusers, GT-2002-30491, ASME TURBO EXPO 2002, June 3-6, 2002, Amsterdam, The Netherlands
- Fleige H.-U., (2002): Experimentelle und numerische Untersuchungen am Modell eines Turbinenaustrittsdiffusors, Doctoral thesis, Hannover, Germany

Göttlich E. et al., (2006): Investigation of Vortex Shedding and Wake-Wake Interaction in a Transonic Turbine Stage Using Laser-Velocimetry and Particle-Image-Velocimetry. ASME Journal of Turbomachinery, 128:178-187

Hayami H, Hojo M, Hirata N, Aramaki S., (2004): Flow with shock waves in a transonic centrifugal compressor with low-solidity cascade diffuser using PIV. Proceedings ASME Turbo Expo 2004, June 14-17, 2004, Vienna, Austria, GT2004-53268

Ibaraki S., Matsuo T., Yokoyama T., (2007): Investigation of unsteady flow field in a vaned diffuser of a transonic centrifugal compressor. ASME J. Turbomach. 129, 686-693

Kluß, D. Stoff, H. Wiedermann, A., (2009): Effect of Wakes and Secondary Flow on Re-attachment of Turbine Exit Annular Diffuser Flow, Journal of Turbomachinery October 2009, Vol. 131 / 041012-3

Kompenhans J., (2009): 25 years of PIV development for application in aeronautical test facilities. Symposium 25 Years of PIV in Aerodynamics, Göttingen, September 23 - 25, 2009

Kruse, H., Quest, J., (1982): Experimentelle Untersuchungen an Nabendiffusoren hinter Turbinen, MTZ-Motortechnische Zeitschrift, 44, pp 13-17, German

Kuschel, M., Seume, J. R., (2011): Influence of unsteady turbine flow in the performance of an exhaust diffuser. ASME Turbo Expo, June 6-10, 2011, Vancouver, Canada.

Logan, E., Jr., Roy R., Logan, L., (2003): Handbook of Turbomachinery

Mohseni, A.; Goldhahn, E.; Braembussche, Renè A., Van den; Seume, J.R. (2011): Novel IGV Designs for Centrifugal Compressors and Their Interaction With the Impeller, Journal of Turbomachinery, March 2012, Volume 134, Issue 2, 021006 (8 pages) doi:10.1115/1.4003235

Mohseni, A. (2010): Development of Endoscopic Stereoscopic PIV for Investigating the IGV-Impeller Interaction in a Centrifugal Compressor. Dissertation, Leibniz Universität Hannover, pp. 84-85

PIVVIEW2C/3C, (2006), Version 3.0, User Manual, PIVTEC, <http://www.pivtec.com>

Pradeep A. M., Bhaskar R., (2010): Study of gas turbine exhaust diffuser performance and its enhancement by shape modifications. Proceedings of ASME Turbo Expo 2010: Power for Land, Sea and Air GT2010 June 14-18, 2010, Glasgow, UK, GT2010-22088

Raab, D. Lippert, D.K. Hennecke (1996), A new concept for the design of turbine diffusers, ASME GT-450

Reynolds S.B., Gorrell, S.E., Estevadeordal J., (2010): PIV analysis on the effect of stator loading on transonic blade-row interactions. Proceedings of ASME Turbo Expo 2010: Power for Land, Sea and Air GT2010 June 14-18, 2010, Glasgow, UK GT2010-22576

- Ristic, D., Lakshminarayana, B., Chu, S., (1999): Three-Dimensional Flowfield Downstream of an Axial-Flow Turbine Rotor. *Journal of Propulsion and Power*, Vol. 15, No.2, M.-A. 1999
- Roosenboom, E.W.M., (2009): High quality PIV data for numerical validation. Symposium 25 Years of PIV in Aerodynamics, Göttingen, September 23 - 25, 2009
- Schlienger, J., Kalfas, A.,I., Abhari, R. S., (2005): Vortex-Wake-Blade Interaction in a Shrouded Axial Turbine. *ASME Journal of Turbomachinery*, October 2005, Vol. 127 / 699.
- Sieker, O.; Seume, J.R. (2008): Effects of Rotating Blade Wakes on Separation and Pressure Recovery in Turbine Exhaust Diffusers, GT2008-50788, ASME TURBO EXPO 2008, June 9-13, 2008, Berlin, Germany
- Sieker, O. (2010): Einfluss von Drall und Nachlaufdübeln auf das Strömungsverhalten und den Druckrückgewinn in axialen Turbinenaustrittsdiffusoren. Dissertation, Leibniz Universität Hannover, p. 19.
- Selesnev, K., Galerkin, U., Anisimov S., (1986): Theorie und Berechnung der Turboverdichtern, pp. 160-161
- Sovran, G., Klomp, E. D., (1967): Experimentally Determined Optimum Geometries for Rectilinear Diffusers with Rectangular, Conical or Annular Cross-Section, *Fluid Mech. Of Int. Flow*, Symp. pp. 270-319
- Stieger RD, Hollis D, Hodson HP, (2004): Unsteady Surface Pressures Due to Wake-Induced Transition in a Laminar Separation Bubble on a Low-Pressure Cascade. *ASME Journal of Turbomachinery* 126:544-550
- Tropea, C., Yarin, A., Foss, J., (editors), (2003): *Springer Handbook of Experimental Fluid Dynamics*, pp. 382-383
- Vassiliev V., Rothbrust, M., Irmisch, S., (2008): Refitting of exhaust diffuser of industrial gas turbine. *Proceedings of ASME Turbo Expo 2008: Power for Land, Sea and Air*, GT2008-50165 June 9-13, 2008, Berlin, Germany
- Vassiliev V., Irmisch, S., Abdel-Wahab, S., (2010): Impact of the inflow conditions on the heavy-duty gas turbine exhaust diffusers performance. *Proceedings of ASME Turbo Expo 2010: Power for Land, Sea and Air* GT2010 June 14-18, 2010, Glasgow, UK GT2010-22840
- Voges, R., Schnell, C. Willert, R. Mönig, (2007), Investigation of blade tip interaction with casing treatment in a transonic compressor – part 1: particle image velocimetry *Proceedings of ASME Turbo Expo 2008: Power for Land, Sea and Air*, June 9-13, 2008, Berlin, Germany GT2008-50210
- Walsh, P. P., Fletcher, P. (2004): *Gas turbine performance*. Blackwell Publishing

Wernet, M. P., Zante, D., V., Strazisar, T., J, John, W. T, Prahst, P.S., (2005): Characterization of the tip clearance flow in an axial compressor using 3-D digital PIV. *Experiments in Fluids* 39:743-753

Woisetschläger J., Göttlich E. (2008): Recent Applications of Particle Image Velocimetry to Flow Research in Thermal Turbomachinery, in: A. Schröder, C.M. Willert (Eds.): *Particle Image Velocimetry New Developments and Recent Applications*, Topics of Applied Physics, Springer

## Appendix

### External triggering

External triggering was employed in order to track the blades and to study the wake generation associated with a particular blade. The phase resolution was set up as follows: after the first exposure, the bladed wheel is in an angular position turned by  $2.8^\circ$ . The second exposure occurs with the bladed wheel in the position  $5.6^\circ$ . After the 5<sup>th</sup> and last exposure, the bladed wheel is in the position  $11.2^\circ$  from the origin. This procedure allows estimating the local evolution of the blade wake. For this procedure, the delay time between output sequences of the laser needs to be fit into the rotational speed of the bladed wheel and the origin must be chosen. Figure 20 shows evaluated pictures containing delayed blade wakes. The measurement region is as in Fig. 9.1. The five images characterize successive double-images for non-swirled flow in the diffuser entrance and velocity magnitude as a contour plot.

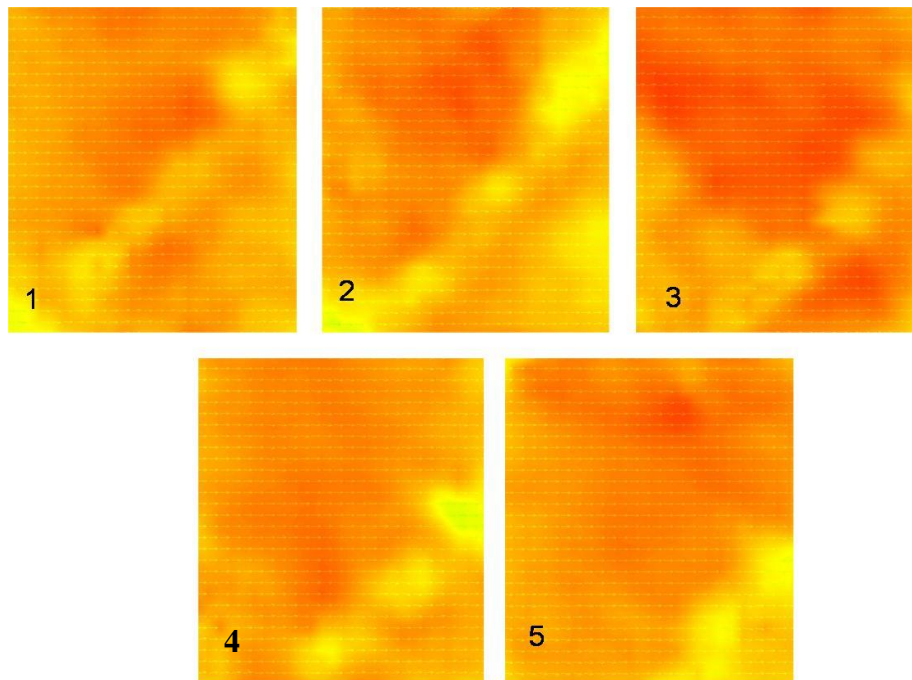


Figure 9.1: Time-resolved blade wake

## **CURRICULUM VITAE**

### **Personal information**

---

Name: Victor Opilat  
Date of birth: 07.08.1985  
Place of birth: St. Petersburg, Russia

### **Educational background**

---

02/2008 - 09/2008  
(6 months) Institute of TFD, Leibniz Universität Hannover  
student assistant

09/2007 - 02/2008  
(6 months) Institute of TFD, Leibniz Universität Hannover, Student exchange  
program

2002 - 2008  
(5 ½ years) The St. Petersburg State Technical University, Russia  
Diploma studies at the faculty of Mechanical engineering  
Major: Aircraft engines and power plants

2000 School exchange program with the Johannes Kepler Gymnasium in  
Leonberg, Germany

1992 – 2002  
(10 years) Gymnasium 74, St. Petersburg, Russia  
University-entrance diploma

### **Professional experience**

---

09/2008 – 08/2011  
(3 years) Research assistant, Turbine group, Institute of Turbomachinery and  
Fluid Dynamics (TFD), Leibniz Universität Hannover, Germany

09/2005 – 08/2007  
(2 years) Assistant at the Aviation Gear Box Department  
Klimov Company (MiG), St. Petersburg, Russia  
Industry Aerospace (Turbine engines plant)

07/2006 – 08/2006  
(2 months) Internship at the Engineering Department of Philip Morris Russia,  
St. Petersburg, Russia. Industry: Cigarette production.

07/2005 – 08/2005  
(2 months) Internship at the Aviation Engineering Department.  
Krasnyi Oktjabr St. Petersburg, Russia. Industry: Aerospace